Charge order in the cuprates

Pelc, Damjan

Sveučilište u Zagrebu

Prirodoslovno-matematički fakultet, Fizički odsjek

Damjan Pelc

NABOJNI RED U KUPRATIMA: NASTANAK, DINAMIKA I INTERAKCIJA SA SUPRAVODLJIVOŠĆU

DOKTORSKI RAD

Mentor: prof. dr. sc. Miroslav Požek

Zagreb, 2017

University of Zagreb

Faculty of Science, Department of Physics

Damjan Pelc

CHARGE ORDER IN THE CUPRATES: FORMATION, DYNAMICS AND INTERACTION WITH SUPERCONDUCTIVITY

DOCTORAL THESIS

Supervisor: prof. dr. sc. Miroslav Požek

Zagreb, 2017

The research leading to this thesis was performed in its entirety at the Department of Physics, Faculty of Science, University of Zagreb, under the supervision of prof. dr. sc. Miroslav Požek.

Istraživanje koje je dovelo do ove disertacije je u cijelosti izvršeno na Fizičkom odsjeku Prirodoslovno-matematičkog fakulteta Sveučilišta u Zagrebu pod mentorstvom prof. dr. sc. Miroslava Požeka.

ACKNOWLEDGEMENTS

During my years of postgraduate studies and research, I have had the opportunity to collaborate, discuss with and learn from a number of people, greatly improving my work and understanding of solid state physics. Most importantly, I am grateful to my mentor prof. Miroslav Požek, for always providing help, guidance and encouragement, and to Marija Vučković, who has significantly contributed to several experiments presented here. I also thank my colleagues and professors at the University of Zagreb: Tonči Cvitanić, Mihael Grbić, Antonije Dulčić, Ivan Kupčić, Neven Barišić, Denis Sunko and Aleksa Bjeliš; as well as collaborators from other institutions: Hans-Joachim Grafe, Seung-Ho Baek, Markus Hücker, John Tranquada, Genda Gu, and Martin Greven, for many fruitful discussions, comments, and samples. I am indebted to my family for years of backing and reassurance. Finally, my gratitude goes to Kristina, for inspiration, unwavering support and love throughout this work.

ABSTRACT

In this thesis, an experimental investigation of charge stripe order in cuprate superconductors is presented. Several lanthanum-based cuprate compounds are taken as model systems for studying charge order physics. Multiple experimental techniques are employed: nuclear magnetic resonance as a local probe, linear and nonlinear conductivity for investigating transport properties and broken symmetries, and specific heat as a thermodynamic probe. The use of complementary experiments provides an overarching picture of the influence of disorder on charge stripe formation, their dynamical properties, and relation with superconductivity. It is found that the charge stripes form through an unconventional precursor charge nematic phase, which only breaks orientational symmetry and is insensitive to disorder, in agreement with previous theoretical work by other groups. We find that the stripes themselves do not appear as a well-defined phase, but always remain short-range ordered. Furthermore, the charge stripes are strongly pinned to lattice defects and are virtually static, but induce strong spin fluctuations which are dynamically decoupled from the charge stripes and display glassy freezing. The stripes strongly influence superconductivity, inducing a decoupling of copper-oxygen planes in cuprates and ushering in a quasi-two-dimensional superconducting state with ultraslow characteristic dynamics. Yet this state is unique to the charge-ordered compounds, showing that cuprate superconductivity in general is not essentially two-dimensional.

Keywords: cuprates, high-temperature superconductivity, charge order, electronic liquid crystal, nuclear magnetic resonance, nonlinear conductivity

Contents

List of Figures

"There are some enterprises in which a careful disorderliness is the true method."

– H. Melville

Chapter 1

Introduction

Understanding high-temperature superconductors is one of the most important endeavours in solid state physics. Yet in the three decades since the discovery of the first cuprate superconductor [1], it has become clear that these materials are extremely complex [2]. To understand their main features, it may be necessary to broaden or abandon many concepts evolved for describing materials during the last century. There are several reasons for this complexity, but arguably the three most important are reduced dimensionality, strong electronic correlations, and disorder. All known high-temperature superconductors are lamellar materials, consisting of electrically conducting atomic planes separated by ionic layers; this leads to a strong anisotropy of all material properties, and in some aspects it is possible to treat these compounds as quasi-two-dimensional. An essential ingredient of high-temperature superconductors are transition metals (such as copper or iron); their atomic orbitals cause strong on-site Coulomb interactions, leading to short-range electronic correlations superimposed on the usual long-range correlations characterizing a Fermi liquid. Finally, to obtain superconductivity, the materials must be doped: additional electrons or holes must be introduced into the respective parent compounds, usually by modifying their stoichiometry. This inevitably makes the materials disordered; yet even without the doping, the structures of major high-T_c compounds are intrinsically prone to local deformation and structural disorder [3]. The interplay between effective two-dimensionality, strong correlations, and disorder gives rise to interesting new physics and very rich phase diagrams. It also makes formulating an all-encompassing theory of high-temperature superconductors extremely challenging. But most importantly, it demands the use of many complementary experimental techniques to gain a complete picture. It is fair to say that the complexity of high-T_c materials has been a major driver of

both experimental and theoretical methods in solid state physics, and significant progress in understanding the materials has been made. Yet several crucial issues remain controversial. It is the intent of this thesis to investigate the interplay between disorder, dimensionality and electronic ordering tendencies using several innovative experimental approaches, in order to provide answers to some of the most debated questions and further our understanding of these fascinating compounds.

1.1 Cuprates as complex materials.

Several families of high-temperature superconductors have been discovered to date, but cuprates remain the most prominent, and will be the subject of our investigations. They are compounds based on copper and oxygen, and have a common structural element: the CuO_2 plane, a rectangular array of Cu and O atoms with the oxygens serving as bridges between the coppers (Fig. 1.1). To obtain a cuprate crystal, ionic layers are inserted between stacked CuO_2 planes. Different cuprate families have different ionic layers, and are doped in different ways. Crystallographically, cuprates belong to the large perovskite family, and their structures are close to tetragonal symmetry. However, as in other prominent perovskites such as the ferroelectric $BaTiO_3$, the tetragonal symmetry is readily broken (locally or globally) due to the intrinsic symmetry of transition metal atomic d-orbitals and bond mismatch between the CuO_2 and ionic layers. The instability of the tetragonal structure leads to a series of structural transitions in some cuprate families, and to local symmetry breaking in others. In all cuprates, the Cu-O bonds in the planes are buckled for the same reason. To obtain superconductivity (and other electronically ordered phases) one must introduce charge carriers into the insulating parent compounds. This is usually done by modifying the ionic layers between the CuO_2 planes, either by substitutional or by interstitial stoichiometry changes. The first cuprate family to be discovered, lanthanum cuprates, has the parent compound La_2CuO_4 (also referred to as La-214), and can be doped by substituting some of the trivalent lanthanum by divalent ions such as strontium or barium. Thus is formed one of the most extensively investigated cuprate systems, $La_{2-x}Sr_xCuO_4$ (LSCO), where x denotes the fraction of substituted lanthanum, and the closely related $La_{2-x}Ba_xCuO_4$ (LBCO). Other well-known cuprates include $YBa_2Cu_3O_{6+y}$ (YBCO or Y-123), $HgBa_2CuO_{4+y}$ (Hg-1201), $Tl_2Ba_2CuO_{6+y}$ (Tl2201) and $Bi_2Sr_2CaCu_2O_{8+y}$ (BSCCO), which are all doped by adding

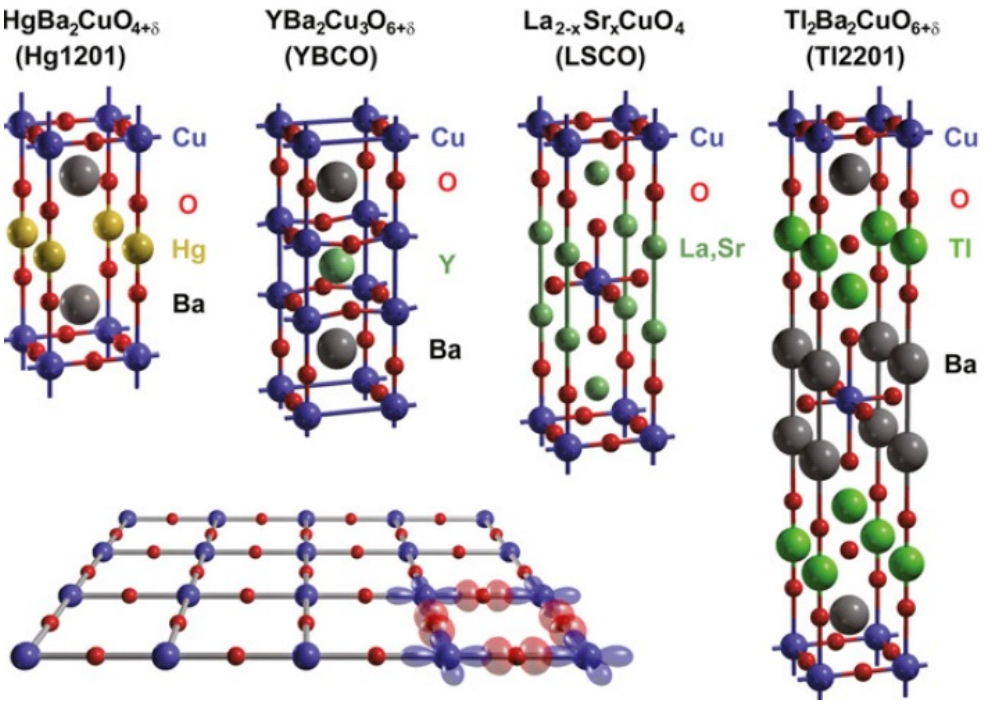

Figure 1.1: The crystal structure of cuprates.
Extended unit cells of four representative cuprate families are shown: mercury-based (Hg1201), lanthanum-based (LSCO), yttrium-based (YBCO) and thallium-based (Tl2201). All families contain the common CuO_2 plane structure, shown schematically with oxygen p and copper d orbitals, and differ in the ionic layers separating the CuO_2 planes. Adapted from [4].

interstitial oxygen atoms. Importantly, the cuprates appear not to be doped like semiconductors – where the dopands form an alloy with the parent compound, and the local states delocalize into impurity bands – but through an electrostatic influence of the dopands on the CuO_2 planes [5, 6]. Determination of the effective number of carriers in the planes is thus often difficult, especially in the oxygen-doped compounds [7].

It is not always possible to synthesize undoped parent compounds, but the known ones – including La_2CuO_4 and $YBa_2Cu_3O_6$ – are antiferromagnetic insulators [8]. This relatively well understood electronic ordering is the basis for all further discussions below. While there are significant differences between the cuprate families, some features of their phase diagrams appear to be universal. A recent schematic phase diagram of hole-doped cuprates is shown in Fig. 1.2, but it must be noted that several elements of the diagram are still disputed. Yet a rough picture can be formed, as follows.

The undoped compounds have one hole per unit cell, and would then have half-filled

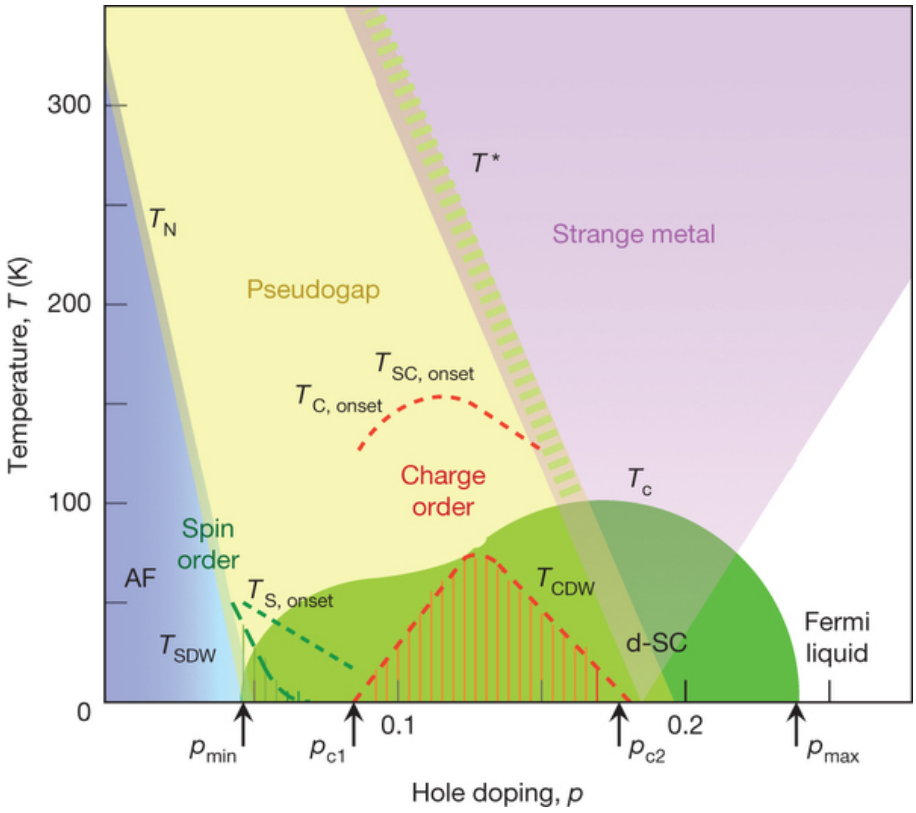

Figure 1.2: Schematic phase diagram of hole-doped cuprates. Upon doping the antiferromagnetic (AF) parent compounds, a spin glass/spin stripe phase (SDW) emerges at low temperatures, and the pseudogap appears below a temperature T^*. Superconductivity (d-SC) and charge order (C and CDW) arise within the pseudogap. The 'strange metal' region can be explained with a temperature-dependent carrier concentration [9, 10]. Tentative critical doping concentrations are marked. Adapted from [2].

bands in a simple band theory. Yet they become antiferromagnetic insulators due to electronic correlations. Such behaviour is well understood within the simplest model which includes a large charge transfer energy barrier between copper and oxygen orbitals, the effective one-band Hubbard model (leading to the Heisenberg spin Hamiltonian) [8, 11–14]. The electrostatic repulsion causes localization of the one hole per unit cell, and antiferromagnetic (AFM) order at lower temperatures. The AFM phase itself is rather conventional, with the ordered spins residing on copper sites and with a single well-defined effective coupling between them [8] up to small corrections [14, 15]. Doping the parent compounds quickly destroys long-range AFM order, replacing it with a spin-glass-like state [8, 16–18]. Superconductivity emerges from that state at around 0.06 additional holes per unit cell [2,19] (or 6% doping). As the compounds are doped further, the superconducting

critical temperature T_c increases, reaches a maximum (at an 'optimal doping' of ~ 0.16) and decreases towards zero on the overdoped side, at doping ~ 0.26. Concomitantly, the normal state of the mobile holes becomes a conventional umklapp Fermi liquid [4], with a large Fermi surface on the highly overdoped side [21, 22]. Although the maximum T_c varies heavily between cuprate families, the characteristic doping concentrations for superconductivity are nearly universal. Another universal and very controversial feature is the pseugogap state in the underdoped region of the phase diagram. Its true nature and origin are still unclear, as well as its role in the formation of superconductivity [20]. Yet it seems likely that it is a remnant of the strongly correlated antiferromagnetic phase of the parent compounds, involving the one localized hole per unit cell [9, 23–25]. Within the pseudogap state, different electronically ordered phases appear, including charge and spin density modulations [2]. Cuprates are thus truly complex materials, with several intertwined electronic ordering tendencies. Charge order is of special importance, since it has recently been shown to be universal in the cuprates as well [26–33, 37]; several theoretical proposals relate it to the pseudogap [38–40], and even to the superconductivity itself [38, 39, 41, 42]. Resolving the role of charge order in the cuprate phenomenology is the primary goal of this thesis, so we must first discuss what is known (and predicted) about it from previous work.

1.2 Charge and spin order in cuprates.

Spontaneous charge modulations appear in a wide range of compounds, being first predicted in quasi-one-dimensional systems [43, 44]. This classic Peierls instability occurs as a way to minimize the net energy of the system by trading elastic for electronic energy. In quasi-two-dimensional materials such as the cuprates, the charge modulations take the form of density waves in the CuO_2 planes, but their origin is extensively debated and apparently more complex than the basic Peierls picture. Relatively soon after the discovery of cuprate superconductors, it was hypothesized that charge (and spin) modulations should exist in these materials [45], as a way to minimize the energy associated with strong antiferromagnetic correlations away from zero doping. In this simple picture, the stripes were imagined as 'rivers' of charge, separated by insulating AFM strips. The first experimental detection of charge stripes in a cuprate, the neodymium co-doped $La_{2-x-y}Nd_ySr_xCuO_4$, was taken as a confirmation of this phase-

separation idea [46]. Yet subsequent work, and the refinement of experimental techniques such as resonant X-ray scattering, showed that the charge modulations are relatively weak in cuprates [29, 33, 37, 47, 48]. Thus the phase-separation scenario had to be modified significantly, and it is now understood that charge (and spin) order is nowhere near as drastic as envisaged in the early work. Yet it remains true that charge stripes induce strong spin fluctuations and glassy spin stripe ordering [49–51], an important aspect of cuprate electronic physics.

Since the basic phase separation scenario is not appropriate, the microscopic mechanism responsible for charge stripes in cuprates is still under scrutiny. Theoretical proposals range from a Fermi surface nesting scenario [52, 53] and Fermi surface instabilities [54] to various local ionic mechanisms [90, 91] and metallic stripes as instabilities of the doped Hubbard model [2, 55, 56]. The situation is further complicated in much-studied compounds such as YBCO, where two distinct types of charge density waves appear: zero-field [30,31,57] and magnetic field-induced [26] density waves. The Fermi surface reconstruction seen universally in quantum oscillation experiments at high magnetic fields [52, 58] indicates that nesting may indeed play a role, but other scenarios for field-induced charge order such as magnetic breakdown have been proposed [59]. It remains unclear if and how the field-induced and zero-field charge stripes are related [57], and what the formation mechanisms are. Furthermore, biaxial charge modulations, known as chequerboard order, have been found in nominally tetragonal materials such as BSCCO [35]. Their relationship to uniaxial stripes in other materials remains unclear, although it seems plausible that the physical origin is similar. Notably, the wave-vectors of charge order in lanthanum-based cuprates [28, 29] have a different doping trend than those in oxygen-doped systems such as Hg1201 [34] and YBCO [32], which might indicate a different physical origin [29]. Yet transport properties such as Nernst effect [36] are remarkably similar; we will show that local amplitudes of the charge modulations are broadly similar as well, and the associated spin dynamics is qualitatively the same. It is therefore plausible that charge modulations in cuprates have a common origin, but different properties due to different levels of point (dopand) disorder and proximity to antiferromagnetism.

Due to relatively small amplitudes and short correlation lengths, charge order in cuprates is difficult to detect. Its presence has only recently been established in the most prominent families, primarily by X-ray diffraction: LBCO [37, 60] and LSCO [61, 62], YBCO [26, 27, 30, 31, 57], Hg1201 [33, 34]. Although charge stripes were first found by

neutron scattering in neodymium co-doped LSCO, there were early indications for their presence in other materials from local probes such as nuclear magnetic resonance (NMR), chiefly in lanthanum cuprates [63–65]. More specifically, a decrease of the copper magnetic resonance signal intensity – called the wipeout effect – occurs when charge stripes appear in the material [47, 63–66]. Yet since the discovery of wipeout, its nature and relation to charge stripes has been controversial [65, 67]. One of our objectives in this thesis is to clarify the origin of the wipeout effect, enabling insights into the microscopic behaviour of charge stripes in representative cuprates.

Perhaps the most important question in relation to charge order is its relationship with other electronic phenomena in cuprates – pseudogap and superconductivity. Surface sensitive experiments such as scanning tunnelling microscopy (STM) and spectroscopy show evidence of local spatial symmetry breaking in the temperature range of pseudogap appearance, which may be interpreted as a nascent charge stripe state [69]. Furthermore, some neutron scattering [70] and resistivity [71] studies have obtained evidence of increased anisotropy within the CuO_2 planes of cuprates such as YBCO, a sign of possible tetragonal symmetry breaking as a precursor to charge stripes. Yet other experiments, such as magnetometry [72–74], polar Kerr effect [75, 76] and polarized neutron scattering [77–79], detect an unconventional magnetism in a similar temperature range, which is more difficult to reconcile with a stripe scenario. The ubiquitous presence of disorder complicates the physics of stripes (and pseudogap) considerably [70, 98–100, 105], and it is thus crucial to resolve the effects of disorder to understand the relation between stripes and pseudogap. We will discuss this point in more detail below.

Notably, the signature of charge stripe correlations and superconducting fluctuations are similar in probes such as Nernst effect and c-axis optical conductivity [80]; the apparent finding of a wide superconducting fluctuation temperature range through Nernst effect measurements [81, 82] was subsequently shown to be caused by a stripe-related signal [36, 83]. However, on the underdoped side of the cuprate phase diagram, charge stripes and superconductivity do coexist in a significant doping range. Since the finding of charge stripes in lanthanum-based cuprates, it was clear that there is a strong interaction between the charge order and superconductivity [18, 84–86]. All cuprates display the so-called '1/8-anomaly', a decrease of the bulk superconducting T_c close to doping 1/8; this is the doping concentration where charge stripes are most stable (Fig. 1.2). X-ray scattering experiments show that the stripe order parameter decreases below T_c

in YBCO [31], also indicating competition between the two ordering tendencies. On the other hand, a state with cooperating stripes and superconductivity (leading to a spatially modulated superconducting phase, or phase density wave) has been suggested [39,87–89], motivated by the dramatic behaviour of LBCO-1/8 [85, 86]. This compound contains an enviable collection of cascading ordered phases, including structural, charge and spin stripe, and superconducting transitions [86]. Most importantly, it appears that the superconductivity of LBCO-1/8 is truly two-dimensional in a wide temperature range from ~ 35 K down to the bulk $T_c \sim 4$ K [85, 86]. This is unique among cuprates, and to explain the almost complete CuO_2 plane decoupling, superconducting phase density waves (PDW) were proposed [89]. If the PDWs are stacked in a particular way, the effective Josephson coupling between CuO_2 planes can be almost eliminated, leading to a stripe-induced two-dimensionality and Kosterlitz-Thouless physics [85,88]. Some aspects of this scenario have been observed in LBCO-1/8 through transport and scattering experiments, but it remains questionable if the model is relevant for the material. Furthermore, other cuprates with prominent charge stripes could display similar effects; a promising example is the co-doped compound $La_{2-x-y}Eu_ySr_xCuO_4$ (LESCO). In this work, LBCO and LESCO will be taken as model cuprates for the investigation of charge stripe physics and striped superconductivity. Contrasting them with other compounds will provide insight into the properties of cuprate superconductivity in general.

1.3 The influence of disorder, electronic liquid crystals.

We have seen that the multiple electronic ordering tendencies in the cuprates provide a rich phase diagram and unconventional physics. The presence of disorder further complicates the understanding of these materials, and will be shown to be important for many of their properties. As noted above, to introduce charge carriers into the insulating CuO_2 planes, chemical doping must be used, introducing a large concentration of point defects into the crystal. Depending on the dopands, the disorder may be quenched – as in the case of Sr substitutional doping – or partially or fully annealed – as for oxygen interstitial doping. Sr dopands are immobile, resulting in a highly homogeneous spatial distribution of point defects, while oxygen mobility in cuprates is quite high and causes specific ionic ordering, further complicating the material properties. Furthermore, the tetragonal perovskite structure of cuprates is intrinsically unstable towards different symmetry-breaking

deformations due to the orbital makeup of Cu atoms [3,6,90,91]. Structural disorder is thus to some degree inevitable in cuprates, regardless of the refinement of synthesis procedures. A crucial unresolved question is, however, whether disorder is relevant for the various electronic phenomena, or can be disregarded or treated in some effective manner.

Models of cuprate band structure neglect disorder completely, making the conventional assumption of translational invariance and enabling a transition to reciprocal k-space in describing electronic properties. This assumption is rarely questioned, and used to interpret a large body of experimental results – from angle-resolved photoelectron spectroscopy to nuclear magnetic resonance and optical properties [91,92]. However, experiments such as hydrostatic and conductivity relaxation [93,94], nuclear quadrupole resonance [95,96], and (most notably) STM [68,97–100] have consistently shown that disorder exists in the cuprates on the nanoscale. Recently it has become clear that underlying disorder also has a profound influence on normal-state conductivity and superconducting fluctuations [101], and some theories argue that heterogeneity is essential for both pseudogap and superconducting pairing [90, 102–104]. Yet the most drastic effects of disorder are on charge and spin stripes. In clean systems the charge stripes are a thermodynamically well-defined ordered phase, appearing through a true phase transition. However, it has been long known theoretically that even low levels of point defects destroy long-range charge stripe order and make it glassy [40, 105–108]. In other words, disorder is a relevant perturbation for charge stripes in the renormalization group sense [109]. Interestingly, vestiges of charge stripe order survive even in moderately disordered systems, but these phases do not break translational symmetry [40, 105, 106]. They have therefore been called 'electronic liquid crystals' [105], since they are different from an ordinary electronic Fermi liquid. Some of them break only rotational symmetry and are referred to as charge nematics, due to the analogy with nematic liquid crystals formed by rod-like molecules. The molecular liquid – electron analogy can be extended further (Fig. 1.3): a liquid phase with broken translational and rotational symmetry is called a smectic, and corresponds to the charge stripes.

Physically, the sensitivity of two-dimensional charge stripes to disorder originates from the almost vanishing energy costs of defects in the stripe structure [107, 159]. The stripes can curl around point defects with virtually no energy penalties, destroying long-range order [40, 105]. Thus the transition into the stripe-ordered state is not a true phase transition, but should be regarded as a crossover. Signatures of such glassy stripes are

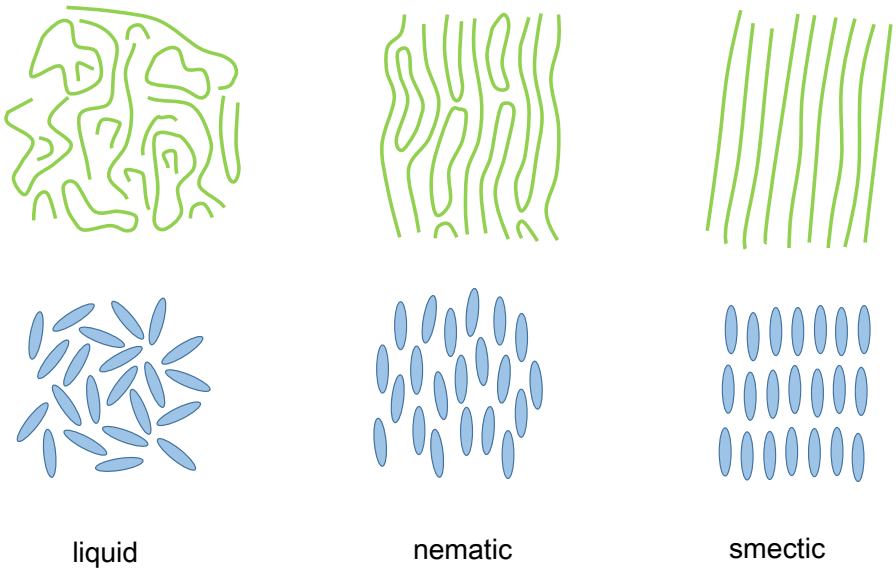

Figure 1.3: Electronic liquid crystals.
Charge ordered phases (above) have their analogies in classical liquids with rod-like molecules (below): a featureless Fermi liquid is analogous to a simple molecular liquid, charge and molecular nematics break orientational symmetry, while smectics break both orientational and translational symmetry in one direction.

consistently observed in local experiments such as nuclear magnetic resonance [50, 65, 66, 110, 111]. Yet recent calculations show that the charge nematic phase is robust with respect to disorder (due to its lower symmetry), and should survive as a well-defined phase [40, 108]. Some experiments, such as neutron scattering [70], STM [69], and YBCO resistivity anisotropy [71], indicate that orientational symmetry is broken in the pseudogap region, leading to the idea that the charge nematic is the hidden order responsible for the pseudogap [40]. Testing this claim will be one of our objectives in this thesis.

Experimentally it is very difficult to study electronic liquid crystals in the cuprates, mainly due to the fact that they do not break translational symmetry. Most scattering methods are then useless, and one must resort to local probes and techniques sensitive to higher-order charge correlations. Precedents for such investigations exist in other strongly correlated materials: in pnictide superconductors, Raman scattering [112,113] and nuclear magnetic/quadrupole resonance [114] was used to detect nematic fluctuations, and in the hidden order system URu_2Si_2 nonlinear magnetic susceptibility provided insight into unconventional spin ordering [115]. Yet in cuprates the appearance and dynamics of

different kinds of charge order remains mostly unexplored experimentally.

We will show here that a well-chosen combination of experimental methods can provide a complete picture of the formation and dynamics of charge stripes in the cuprates, and give novel insight into the interaction between stripes and superconductivity. This will add important pieces to the cuprate phenomenology, enable a comparison to other materials and contemporary theoretical ideas outlined above, and provide answers to some long-standing questions.

The thesis is organized as follows: in Chapter 2, we discuss the experimental techniques used to study charge order in cuprates, their theoretical foundations and what information can be gained; Chapter 3 presents the results of the studies and discussion of their physical implications, while Chapter 4 is a summary.

Chapter 2

Experimental Methods and their Interpretation

The most important aspect of the work presented here is the use of multiple experimental techniques, including several innovations, to obtain in-depth information about the intertwining electronic orders in representative cuprates. In the Introduction, we have discussed in broad strokes the experimental difficulties for studying unconventional charge order; here we will describe in some detail the experimental methods used to surmount these difficulties. Four distinct techniques have been chosen to give an all-encompassing physical picture: a local probe – nuclear magnetic (and quadrupolar) resonance; a bulk thermodynamic probe – differential microcalorimetry; and two transport probes – linear and nonlinear conductivity. To make some of these measurements possible, custom-made experimental probes were constructed; the nonlinear conductivity method was newly developed [116], and innovations were introduced to the other, more conventional experimental techniques in order to make measurements which were previously unavailable. High-quality single crystals, characterized in detail in previous work, were used for all investigations. This is of particular importance since it is known that NMR signal wipeout is different in powder and single crystal samples [65,66]. Unconventional superconductivity and symmetry breaking related to charge order can only be studied in single crystals as well, because of the well-defined crystallographic directions and absence of grain boundaries in crystals. The use of state-of-the-art high-quality samples ensures that our results and conclusions pertain to intrinsic effects, and not irregularities introduced by imperfect sample preparation.

2.1 Nuclear magnetic resonance.

2.1.1 Theoretical background.

Nuclear magnetic resonance (NMR), and the closely related nuclear quadrupole resonance (NQR), are spectroscopic techniques which use the transitions between quantum levels of nuclear spins to investigate the local magnetic and electric fields seen by the nuclei [117]. This makes NMR and NQR powerful local probes, providing microscopic information about static and dynamic fields in the material. The energy differences between nuclear spin levels are typically of the order of 10^7 Hz, which places NMR and NQR in the MHz frequency range and enables highly sensitive coherent detection. Before describing the NMR experiment in more detail, we will first discuss the scope and possibilities of the technique in a somewhat formal manner.

The basic Hamiltonian of a nuclear spin in an external magnetic field $\mathbf{H}_0$ is [117]

$$\mathcal{H}_{n0} = -\gamma\hbar \sum_{\alpha} H_{0\alpha} I_{\alpha} \tag{2.1}$$

where γ is the nuclear gyromagnetic ratio, and I_α the components of the nuclear spin. However, in a material the local magnetic field is modified by coupling to electrons. Also, a quadrupolar term appears in the Hamiltonian due to the interaction between the local electric field and nuclear quadrupole moment. The full Hamiltonian is then

$$\mathcal{H}_n = \mathcal{H}_{n0} + \mathcal{H}_{n-el} + \mathcal{H}_Q, \tag{2.2}$$

where $\mathcal{H}_{n-el}$ is the nuclear-electron interaction contribution and $\mathcal{H}_Q$ the quadrupolar contribution. We first consider the nuclear-electron term, which has important static and dynamic aspects in the experiment. $\mathcal{H}_{n-el}$ can be derived [118] by considering the coupling between electrons and an average nuclear magnetization $\mathbf{M}_n = \gamma\hbar \langle \mathbf{I} \rangle$. In reciprocal space, the coupling then becomes

$$\mathcal{H}_{n-el} = \sum_{\mathbf{q}} \sum_{\alpha,\beta} A_{\alpha,\beta}(\mathbf{q}) I_{\alpha} \langle \hat{m}_{\beta}(\mathbf{q}) \rangle \tag{2.3}$$

where $A_{\alpha,\beta}$ is a q-dependent form-factor and $\hat{m}$ the electron magnetization operator. The induced electronic magnetization is simply $\langle \hat{m}_{\beta}(\mathbf{q}) \rangle = \sum_{\kappa} \chi_{\kappa,\beta} H_{0\kappa}(\mathbf{q})$, with $\chi_{\kappa,\beta}$ the magnetic susceptibility tensor. Of course, this simple form is only valid in the linear response approximation, but it is universally used in NMR and we are not aware of any significant exceptions. Clearly the nuclear-electron coupling term effectively modifies the

field $\mathbf{H}_0$ at the nuclear site; if we assume for simplicity that the form factor $A_{\alpha,\beta}$ is diagonal, the effective field can be written as

$$H_{\alpha,eff} = \left(1 + \frac{A_{\alpha\alpha}}{\gamma\hbar}\chi_{\alpha\alpha}\right) H_{0\alpha} = (1 + K_{\alpha\alpha})\, H_{0\alpha} \tag{2.4}$$

where we have denoted the dimensionless field change $K_{\alpha\alpha}$, conventionally called the Knight shift [92, 117]. It is straightforward to generalize the expression for nondiagonal K. Clearly the Knight term shifts the NMR resonance frequencies in proportion to the electronic susceptibility. Notably, if the electronic system displays static magnetic ordering, the Knight shift description becomes invalid due to the presence of strong intrinsic magnetic fields, making possible a detection of 'zero-field' NMR signals. Measuring the NMR line shift gives a microscopic measure of the static susceptibility and complements macroscopic susceptibility measurements (especially in that it is insensitive to magnetic impurities, being a true bulk probe). Yet in the lanthanum-based cuprates we investigate here, the Knight shift is of limited experimental merit due to the large widths of the NMR lines, which make the determination of the shift difficult – this is not generally the case in cuprates, especially oxygen-doped systems where point electrostatic disorder is relatively small. The dynamic aspects of the nuclear-electron coupling are much more important for us, as follows.

Along with shifting the resonance lines, the nuclear-electron interaction can induce transitions between nuclear levels. The energy is then transferred from the nuclear spin system, which relaxes into lower states, to the lattice (or in this case, the electron system, which is then thermalized with phonons). The corresponding relaxation time – termed spin-lattice relaxation – can be obtained from the coupling Hamiltonian using Fermi's golden rule and employing equilibrium Fermi-Dirac statistics for the electrons. The result is

$$\frac{1}{T_1} = \frac{2\pi}{\hbar^2} \sum_{\mathbf{q}} |A(\mathbf{q})|^2\, S_{+-}(\mathbf{q}, \omega) \tag{2.5}$$

expressed through the dynamic structure factor S_{+-}, with ω being the NMR resonance frequency. The structure factor is defined as the Fourier transform of the electronic two-point magnetization correlation function, $2\pi S_{\alpha\beta}(\mathbf{q}, \omega) = \int_{-\infty}^{\infty} dt e^{i\omega t} \langle \hat{m}_\alpha(\mathbf{q}, t) \hat{m}_\beta(-\mathbf{q}, 0) \rangle$. The fluctuation-dissipation theorem connects this correlation function to the imaginary part of the magnetic susceptibility, giving a relation between spin-lattice relaxation and susceptibility of the form

$$\frac{1}{T_1} = \frac{2k_B T}{\omega} \sum_{\mathbf{q}} |A(\mathbf{q})|^2\, \Im\left(\chi_{+-}(\mathbf{q}, \omega)\right) \tag{2.6}$$

where k_B is Boltzmann's constant and T the temperature. Thus measuring T_1 provides a way of determining the imaginary part of the susceptibility at the NMR frequency, giving important information about low-frequency spin dynamics in the material. The susceptibility can be independently measured e.g. by inelastic neutron scattering, and in many cases agrees with the NMR results [92]. However, we shall see that there are important differences when slow spin fluctuations appear in relation to charge stripes.

The spin-lattice relaxation time T_1 measures the rate of energy exchange between the spin system and other components – in the above-discussed case, conduction electrons. Yet if the spin system is excited in a coherent manner, an additional relaxation time appears: the spin-spin relaxation time T_2, which measures the rate of spin decoherence (without energy transfer). Physically, decoherence of the spin ensemble occurs because each nuclear spin experiences a slightly different local field, either due to slow fluctuations or static effects. The theory of T_2 is in principle much more complex than that of T_1, but two limiting cases deserve attention for their usefulness. In the static limit, mutual nuclear spin-flip processes are neglected, and the nuclear spin interaction that causes decoherence is only transferred through the electronic spins [119, 120]. It can be shown that in that case the spin-spin decay curve has a Gaussian shape, $\langle I_{+,-} \rangle (t) \sim \exp(-t^2/2T_{2G}^2)$, with T_{2G} the corresponding relaxation time. $1/T_{2G}$ is proportional the real part of the electronic susceptibility [92, 119], providing another way of determining this important quantity microscopically. In the opposite, dynamic limit, mutual spin flips dominate and the relaxation is purely exponential, $\langle I_{+,-} \rangle (t) \sim \exp(-t/T_{2E})$; this case can be realized for certain configurations of the external (or internal) magnetic fields in anisotropic systems [119]. Both regimes are relevant for copper magnetic resonance in cuprates, and the transition from static to dynamic spin decoherence will be a sign of the appearance of strong spin fluctuations on the NMR timescale.

The intensity of the nuclear resonance signal is proportional to the number of investigated nuclei in the sample, and the equilibrium population differences between nuclear levels. In a vast majority of cases, the spin system is well described by classical Maxwell-Boltzmann thermodynamics, implying that the population differences depend on temperature as $1/k_BT$. Thus the signal decreases at higher temperatures, and if one is interested in the number of nuclei contributing to it, the thermal Boltzmann factor must be compensated for. Importantly, spin-spin and spin-lattice relaxation times can also influence the apparent signal intensity: as we will discuss in more detail below, the NMR excitation

and detection takes some time; if relaxation occurs on a similar timescale, the signal will decrease. This is the cause of the well-known wipeout effect – a Cu NMR/NQR signal decrease related to charge and spin stripe order in cuprates [63–67, 110]. By performing measurements faster than was possible in previous work, we will be able to avoid wipeout to a large extent in some compounds, resolving its spin-fluctuation origin.

The last contribution to the nuclear Hamiltonian, the quadrupolar term, is of special interest in cuprates with charge order [26, 27, 47, 57, 117]. Its origin is the interaction of local electric field gradients with the nuclear electric quadrupole moment, thus giving the possibility of measuring local electric fields. Generally, the quadrupolar term can only appear if the nucleus under investigation has spin higher than 1/2, since spin-1/2 nuclei are spherically symmetric and have zero quadrupole moment [117]. We will only consider the case of spin-3/2 nuclei (relevant for Cu NMR and NQR), and assume that the local electric field gradients have approximate cylindrical symmetry (corresponding to a tetragonal crystal structure, with two equivalent directions in the CuO_2 planes). The Hamiltonian then reads [117]

$$\mathcal{H}_Q = \sum_\alpha \frac{1}{9} \frac{eQV_{\alpha\alpha}}{2} \left(3I_\alpha^2 - \frac{15}{4} \right) \tag{2.7}$$

where e is the elementary charge, Q the nuclear quadrupole moment, and $V_{\alpha\alpha}$ the second derivatives of the electric potential at the nuclear site. Depending on the size of Q and applied external magnetic field H_0, the quadrupolar term can be a small perturbation within the NMR Hamiltonian, become comparable to the magnetic term, or dominate all other terms. If the external magnetic field is strictly zero (and there are no permanent internal magnetic fields), $\mathcal{H}_Q$ remains as the only contribution to the nuclear spin Hamiltonian: this case is referred to as pure nuclear quadrupole resonance (NQR). Since Q for different nuclei is known with precision, a measurement of the pure NQR spectrum gives direct information on the size of local static electric field gradients, in analogy with the Knight shift for the magnetic case. This is very valuable if charge modulations are present. To investigate spin fluctuations, it will prove advantageous to apply external magnetic fields in cuprates with stripe order – in the full Hamiltonian (A.1), the quadrupolar term cannot be treated as a perturbation in that case, since it is comparable to the magnetic contribution. A numerical diagonalization of the full Hamiltonian [121] is then necessary to determine the resonant frequencies (Fig. 2.1).

To summarize, nuclear magnetic resonance is a versatile and powerful method for obtaining information about local fields in materials: we will use it mainly to determine

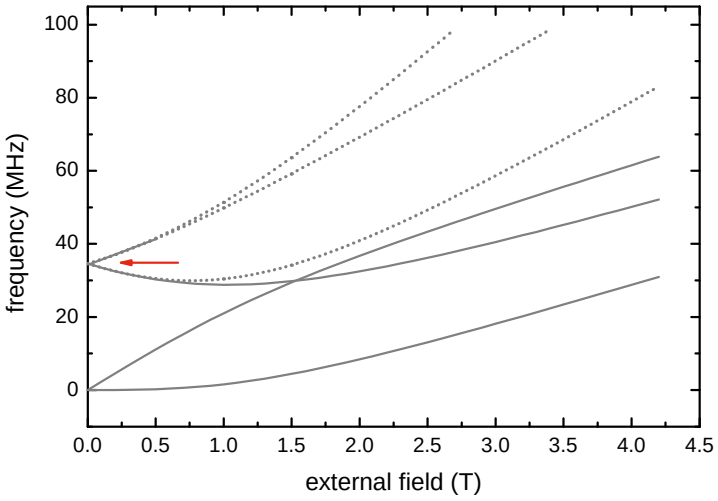

Figure 2.1: Nuclear spin levels of ^{63}Cu.

Nuclear transition frequencies for a ^{63}Cu nucleus with comparable magnetic and quadrupolar contributions to the Hamiltonian are shown in dependence on the applied magnetic field (which is perpendicular to the symmetry axis of the electric field gradient tensor). The transitions are obtained by numerical diagonalization of the nuclear Hamiltonian, eq. (A.1) – see Appendix A for details. The arrow marks the pure NQR frequency. Dotted lines have small intensity (i.e. they are nominally 'forbidden' transitions).

the spin dynamics (through relaxation time measurements) and investigate charge order (through NQR spectroscopy and signal wipeout).

2.1.2 Fast relaxation measurements.

Having shown what physical information can be gained from NMR/NQR, we proceed to describe the experiment itself, with focus on innovations that have made fast relaxation rate measurements possible. As mentioned above, NMR is a radio-frequency (RF) spectroscopic technique, enabling coherent excitation and detection of the nuclear spin transitions. In practice, this means that the sample is put in a coil which is part of an LC resonant circuit. The circuit serves as an antenna for both excitation and detection. Pulsed NMR spectroscopy is used exclusively, due to its many advantages in measurement possibilities and signal processing [122]. Within that method, microsecond RF pulses are used to excite the nuclear spin system out of equilibrium. The nuclear magnetization is then refocused and detected using spin echoes, as discussed below. A coherent NMR spectrometer generates the excitation pulses, which pass through a high-power pulse am-

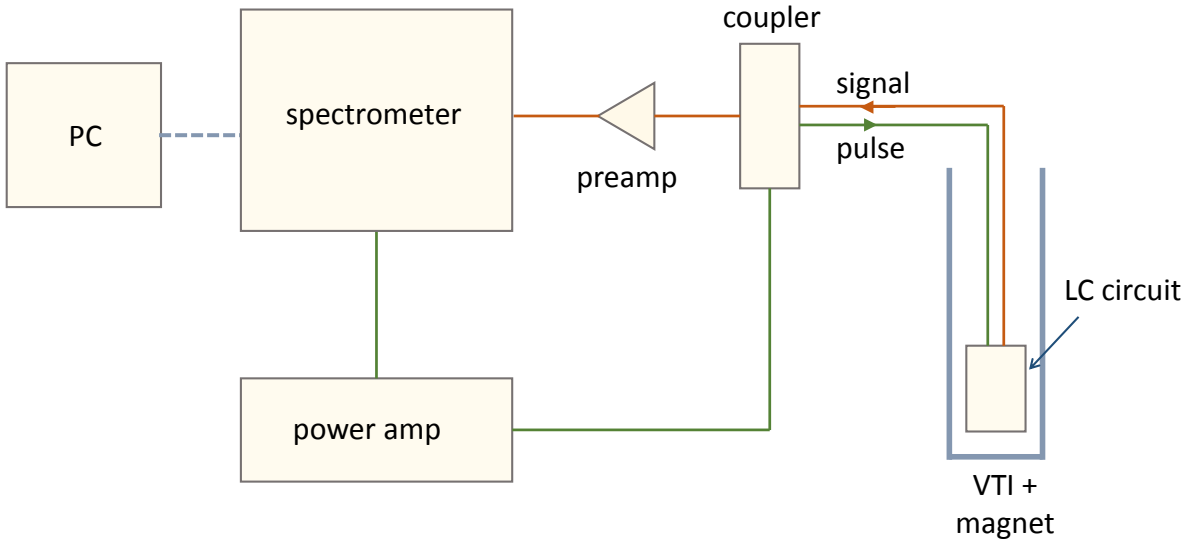

Figure 2.2: Shematic representation of the NMR experimental setup.

A simplified block diagram of the NMR/NQR experiment, with a coherent spectrometer serving as both a pulse generator and signal detector, a power amplifier increasing the excitation pulse amplitude, a passive transcoupler serving as a switch to isolate the sensitive signal preamplifier from the strong RF pulses, and a NMR probe inside a variable temperature inset (VTI) for sample temperature regulation. Signal and excitation pulses are denoted by different lines, but in reality the same coaxial transmission line is used.

plifier and passive coupler before reaching the LC circuit and sample. The NMR signal is detected by the same spectrometer, with a low-noise preamplifier used for first stage signal conditioning. A schematic of the entire experiment is shown in Fig. 2.2. For measurements in magnetic fields, we use a high-homogeneity Oxford Instruments superconducting magnet with a variable-temperature insert. Thus the sample and LC circuit are in a stream of helium at atmospheric pressure, minimizing self-heating from the intense RF pulses. To further decrease the heating effects, a sapphire holder is used for the sample.

The NMR and NQR spectral lines in cuprates are typically rather broad, due to the electrostatic disorder [65,95,123]. This means that the only reasonable way to detect the signals in a pulsed experiment is to use the spin echo technique [124]. To understand the spin echo (and how to measure it with short waiting times), we will use the standard classical picture of nuclear spin dynamics, noting that the same results are obtained within a more complete density matrix formalism [117]. In equilibrium, the spin system

is polarized either by an external magnetic field or by internal electric field gradients, as written in the static nuclear Hamiltonian (A.1). Thus the nuclear spin levels are unequally populated and the spin ensemble has an average magnetization $\langle \mathbf{M}_n \rangle$, whose direction defines the z-axis of an internal spin coordinate system. The definition can be written simply as $\langle \mathbf{M}_n \rangle = \langle M_{nz} \rangle \hat{\mathbf{z}}$. An RF magnetic field pulse causes transitions between the nuclear spin levels and places the system out of equilibrium: effectively, the average magnetization is rotated from its equilibrium direction. If the pulse has the correct duration, the populations of the spin levels are precisely equalized after the pulse, and the entire nuclear magnetization lies in the xy-plane of the internal coordinate system. Such a pulse is referred to as a $\pi/2$ pulse, since it rotates the effective magnetization by $\pi/2$. After the pulse, the level populations change spontaneously and the magnetization returns to equilibrium with characteristic relaxation time T_1. The most straightforward way of measuring NMR would be to detect the nuclear magnetization itself; yet this is extremely difficult in most situations, due to the very small magnetic moments involved (although SQUID-based experiments have been devised to make such measurements [125]). Instead, the time-dependent part of the magnetization is detected using simple magnetic induction in the LC circuit containing the sample. In the effective magnetization picture, the only time-dependent components are $\langle M_{nx} \rangle$ and $\langle M_{ny} \rangle$, which oscillate at the resonant frequency corresponding to the nuclear spin level energy difference. However, if different nuclei have slightly different resonant frequencies – or, equivalently, if the spectrum is broadened – the in-plane components of the effective magnetization will quickly decay to zero. To counteract this, a second pulse can be applied after the $\pi/2$ pulse, which refocuses the in-plane magnetizations causing a signal peak known as a spin echo (Fig. 2.3). The refocusing pulse should be twice as long as the $\pi/2$ pulse for optimal spin echo creation to fully rotate the spins, and hence is called a π pulse. If the time interval between the $\pi/2$ and π pulses is τ, the peak of the spin echo will occur at a time 2τ after the $\pi/2$ pulse. The time τ is referred to as the echo time. Importantly, the spin-echo pulse sequence cannot refocus the in-plane magnetizations if intrinsic decoherence has occurred – thus the spin echo amplitude decays with increasing τ, with a characteristic time equal to the spin decoherence time T_2. Clearly, if T_2 is short, detecting the signal becomes problematic.

In previous NMR and NQR work the typical echo times are above 10 μs [92]. We have managed to shorten this time by an order of magnitude, enabling measurements

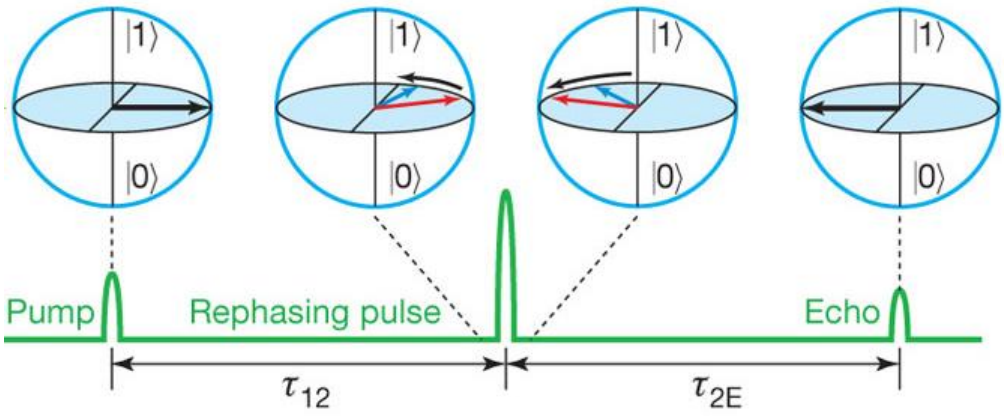

Figure 2.3: The nuclear spin echo.
A schematic representation of the spin echo experiment: the pump or $\pi/2$ pulse rotates the nuclear magnetization into the xy-plane, where different spins precess with slightly different angular rates due to local field inhomogeneity. A rephasing or π pulse rotates the spins by π, enabling their refocussing after an echo time τ_{2E}. Adapted from [126].

with T_2 shorter than 3 μs. Two factors bear a decisive influence on the shortest possible echo time in an NMR experiment: preamplifier recovery times and LC circuit ringing. During the RF pulses, the preamplifier is overloaded, and detection of the echo signal cannot commence until the amplifier recovers. Modern fast recovery amplifiers, such as the Miteq AU1114 used in our experiments, have recovery times of about 1 μs, mostly eliminating this problem. LC ringing is much more serious: an RF pulse excites resonant current/voltage oscillations in the LC circuit, which persist some time after the pulse and can completely obscure the small NMR signal. The ringing decay time is proportional to the Q-factor of the circuit, but so is the circuit's passive amplification factor, which determines sensitivity. Thus a decrease of the Q-factor suppresses ringing, but a price must be paid in NMR sensitivity. Various active electronic schemes have thus been devised to damp the ringing [127, 128], but none of them operate fast enough for our purposes. The only remaining option is to use passive damping, i.e. intentionally spoiling the Q-factor by adding resistors to the LC circuit. By a systematic optimization of the Q-factor, we have found that connecting a resistor of 20 Ω in series with the sample coil enables fast measurements of Cu NMR and NQR in the frequency interval 30-50 MHz with a

reasonable loss of signal sensitivity. In addition to spoiling the Q-factor of the LC circuit, a technique known as phase cycling can be used to further decrease the effects of ringing (but only as long as the preamplifier is in the linear regime). Since the NMR spectrometer contains a heterodyne phase-sensitive detector, the relative phases of detection and all excitation pulses are well defined. By cycling the phases from acquisition to acquisition and averaging the detected signals, the nuclear echo signal can be enhanced and the ringing suppressed, since they have different physical origins and hence different relative phases. We use a double-antiringing phase cycle, which cancels the ringing induced by both $\pi/2$ and π pulses in a spin echo sequence (Table 2.1).

$\pi/2$ pulse	0	2	0	2	0	2	0	2
π pulse	1	1	3	3	0	0	2	2
detector	0	2	0	2	2	0	2	0

Table 2.1: Spin echo antiringing phase cycle. The numbers are the phase divided by $\pi/2$.

We have seen that to measure the spin-spin relaxation time T_2 one simply needs to perform a spin-echo experiment with different echo times. Determining the spin-lattice relaxation time is slightly more complicated, since a measurement of the z-component of the nuclear magnetization is needed. It is accomplished by using a three-pulse sequence, wherein the first pulse (or preparation pulse) rotates the instantaneous nuclear magnetization into the xy-plane, which is then detected with a standard spin echo sequence. By changing the time between the preparation pulse and echo pulses, the return of $\langle M_{nz} \rangle$ to equilibrium can be traced. A more involved phase cycle has to be used to ensure ringing cancellation (Table 2.2).

preparation	1	1	1	1	3	3	3	3
$\pi/2$ pulse	0	2	0	2	0	2	0	2
π pulse	1	1	0	0	1	1	0	0
detector	0	2	2	0	0	2	2	0

Table 2.2: Spin lattice relaxation measurement antiringing phase cycle. The numbers are the phase divided by $\pi/2$.

Employing our short echo time methodology described above, measurements of short T_1 also becomes possible. This will be of great importance in studying spin fluctuations induced by charge order, and in clarifying the nature of signal wipeout.

2.2 Linear and nonlinear conductivity.

2.2.1 Contact-free conductivity measurement.

Electrical conductivity is one of the basic properties of any material, but measuring it in cuprates poses some specific challenges. Firstly, cuprates are ceramic materials, making it difficult to make reliable electrical contacts on them. Usually the procedure involves baking in an oxygen atmosphere and repeated annealing of the contacts. Even if the contact resistance is reasonably low, the procedure can significantly affect the local doping of the crystal, sometimes even creating a percolating superconducting path above the nominal T_c. This is especially troublesome if one wants to investigate superconducting effects such as quasi-two-dimensional fluctuations, where the intrinsic bulk conductivity is very high (but not yet infinite). As discussed in the Introduction, one of our objectives is to investigate the interplay between charge and spin stripes, disorder and superconductivity, making the contact-related problems significant. Therefore a contact-free method was established to reliably measure linear (and nonlinear) conductivity of cuprate single crystals.

The contact-free experiment is similar to the previously developed microwave conductivity measurement [129], used extensively in cuprate and other systems [101, 130–133]. Related radio-fequency measurement methods utilizing tunnel diode resonators [134, 135], marginal oscillators [136, 137] and mutual inductance [138, 139] have also been used for complex conductivity and NMR measurements in the past. The central idea is to use the sample as a perturbation of a resonant cavity (for microwaves) or circuit (for lower frequencies). Measuring the resonant frequency and Q-factor of the cavity or circuit, the complex conductivity of the sample can be deduced. To measure the resonant parameters, a frequency-modulated alternating voltage is applied to the resonator, and a directional coupler is used to detect the reflected component. Due to the frequency modulation, the rectified reflected voltage traces out the resonant curve, enabling a precise determination of its parameters. A slightly different method is used in the MHz and microwave frequency range, where the frequency and Q-factor are obtained by measuring the harmonic components of the rectified reflected signal. Yet when extending the experiments down to frequencies of ~ 10 kHz the sensitivity of the resonant curve analysis method becomes superior. The overall sensitivity depends on the Q-factor of the resonator, and thus deteriorates at low frequencies – this sets the practical lower limit of ~ 10 kHz for this kind

of experiment.

Three different experimental probes were used for contact-free conductivity measurements. A previously constructed microwave cavity probe [129] was employed for frequencies of $\sim$ 10 GHz; this probe enables measurements in a wide temperature range, since the cavity is always at liquid helium temperatures and does not introduce a temperature-dependent background. The sample is kept on a sapphire holder in vacuum, its temperature controlled with a resistive heater and measured with a cernox resistive sensor. A similar probe for frequencies between 10 kHz and 100 MHz was constructed, having a coil and capacitor resonant circuit in place of the cavity. The LC circuit was immersed in liquid helium as well, with the coil wound on a glass tube to avoid Q-factor deterioration. Due to the relatively weak thermal coupling between the sample and helium bath, the base temperature in this probe was around 15 K. To make measurements at lower temperatures (down to 1.5 K in a pumped variable temperature insert), a third option was used: we simply worked with an NMR probe, which already contains an LC circuit. However, in this configuration the resonator and sample have the same temperature, and the temperature dependence of the empty coil Q-factor introduces a background which is hard to remove. Thus the NMR probe was only used at temperatures below $\sim$ 20 K, where the resistivity of the coil material saturates and the Q-factor of the empty circuit does not significantly depend on temperature.

An established procedure was used to obtain the complex conductivity of the single crystal samples from the resonant circuit parameters. The relationship between the components of the conductivity tensor and the power absorbed in the sample was derived in [140], and independently in [141]; we follow the approach of [141]. For a rectangular sample with side dimensions $2a$ and $2b$ and length c, the power absorbed from an oscillating magnetic field (parallel with c) with amplitude H_0 and frequency ω is equal to

$$P(\omega) = \frac{1}{2} i\omega\mu_0 H_0 \frac{\mu(\omega)}{1 + (\mu(\omega) - 1)N_m} \tag{2.8}$$

where N_m is the demagnetizing factor for a rectangular sample geometry [142], and $\mu(\omega)$ the effective complex permeability of the sample given by

$$\mu(\omega) = \frac{4}{\pi} \sum_{m\ odd} \frac{1}{m} \left(\frac{\tanh \beta_m b}{\alpha_m \beta_m} + \frac{\tanh \delta_m a}{\gamma_m \delta_m} \right) \tag{2.9}$$

with $\alpha_m = \pi m/2a$, $\gamma_m = \pi m/2b$, $\beta_m^2 = i\omega\mu_0\sigma_x + \alpha_m^2\sigma_x/\sigma_y$ and $\delta_m^2 = i\omega\mu_0\sigma_y + \gamma_m^2\sigma_y/\sigma_x$. The conductivities along a and b are σ_x and σ_y, respectively. The real and imaginary components of the absorbed power are related to the parameters of the resonator through

$\Re P(\omega) \sim 1/Q_0 - 1/Q$ and $\Im P(\omega) = (\nu - \nu_0)/\nu_0$, where Q_0 and ν_0 are the Q-factor and resonant frequency of the empty resonator. The components of the conductivity tensor are obtained numerically from measurements of Q and ν in dependence on temperature, for different orientations of the sample. The parameters Q_0 and ν_0 are determined by the shape and material of the resonant cavity in the microwave experiment, while at lower frequencies they can be changed in a wide range by modifying the inductance and capacitance of the resonant circuit components.

2.2.2 Conductivity and Kosterlitz-Thouless physics.

The contact-free conductivity measurement technique is especially well suited to investigate exotic superconducting phases, where the conductivity is very high but not necessarily infinite. Cuprate superconductors are layered materials, and hence their superconductivity is always strongly anisotropic [144, 145]. Yet it is debated if the superconductivity is essentially three-dimensional, or can be regarded as two-dimensional [143, 146] (with interlayer coupling corrections for bulk samples). In several of the most prominent cuprate families, microwave conductivity measurements [131, 133, 147] have shown that superconductivity in the CuO_2 planes appears in the same way as perpendicular to the planes, indicating a three-dimensional nature. Some specific materials, however, seem to be exceptions. The clearest evidence for true two-dimensional superconductivity to date is obtained in underdoped LBCO (hole doping $\approx 1/8$, where contact conductivity measurements have detected several hallmark features of two-dimensionality [85, 86].

It has been known for a long time that long-range superconducting order is impossible in two-dimensional systems due to strong phase fluctuations [148, 151, 152]. Instead, they are described by Berezinski-Kosterliz-Thouless (BKT) theory, where the superconducting correlation function changes from an exponential to a power-law behaviour at a characteristic temperature T_{BKT}, but long-range phase coherence never develops [148, 149, 153]. The strong fluctuations thus completely change the nature of the superconducting order and renormalize the bare mean-field transition temperature T_{c0}. The Berezinski-Kosterliz-Thouless transition at $T_{BKT} < T_{c0}$ can thermodynamically be regarded as an infinite-order phase transition, with several specific material properties appearing in its vicinity: a fast exponential divergence of the correlation length [109], strongly nonlinear current-voltage characteristics [154, 155], and sensitivity to external pair-breaking fields (and thus very weak diamagnetic shielding). Current-voltage nonlinearity, an essentially

infinite ratio between in-plane and c-axis conductivity, and sensitivity to external magnetic fields have been detected in LBCO-1/8 [85], making it the best known candidate for Kosterliz-Thouless behaviour in a bulk material. Yet a much more stringent test would be an investigation of the dynamic properties of LBCO-1/8 superconductivity, for which we use contact-free conductivity measurements in a wide frequency range.

Berezinski-Kosterliz-Thouless theory can be formulated in terms of superconducting vortex-antivortex pairs – the temperature T_{BKT} is then the vortex unbinding temperature, above which free vortices and antivortices exist in the material. In clean materials, the dynamics of the free vortices can be described by conventional Debye-Drude exponential relaxation at temperatures high above T_{BKT}, leading to a frequency-dependent conductivity of the form

$$\Re\sigma(\omega) = \rho_0\tau\frac{1}{1+\omega^2\tau^2},\ \Im\sigma(\omega) = \rho_0\tau\frac{\omega\tau}{1+\omega^2\tau^2} \tag{2.10}$$

where ρ_0 is the bare superconducting density and τ the vortex relaxation time [154–156], which is proportional to the free vortex density. Close to T_{BKT} the vortices bind into vortex-antivortex pairs, the number of free vortices diminishes and the response is dominated by the bound pairs; this leads to a model referred to as Minnhagen phenomenology [154], with conductivity

$$\Re\sigma(\omega) = \frac{\rho_0}{\epsilon}\frac{2}{\pi}\frac{\tau_M\ln\omega\tau_M}{\omega^2\tau_M^2-1},\ \Im\sigma(\omega) = \frac{\rho_0}{\epsilon}\frac{\tau_M}{1+\omega\tau_M} \tag{2.11}$$

where ϵ is an effective vortex dielectric constant and τ_M the corresponding relaxation time. Importantly, the characteristic relaxation times of the vortices are extremely slow compared to other relevant electronic scales, as seen in investigations of superconducting and superfluid films [156–158]. Measurements of the frequency-dependent conductivity in materials which are candidates for BKT physics will give us the possibility to compare with relations (2.10) and (2.11), providing insight into vortex dynamics and giving evidence of the existence of true 2D superconductivity.

2.2.3 Nonlinear response.

As discussed in the previous section, one of the distinctive properties of two-dimensional superconductors is the strong nonlinearity of their current-voltage characteristic both above and below the BKT transition temperature [85, 154, 155]. However, nonlinear conductivity is also appreciable in any superconductor, especially in the temperature range

above T_c where traces of superconductivity still exist [101]. Furthermore, it is known that one-dimensional charge density waves respond to external electric fields in a nonlinear way due to pinning effects [159], so similar effects are expected for charge stripes. All this implies that studying the nonlinear response of cuprates is a worthwhile endeavour, capable of providing information on many aspects of electron correlation physics.

Nonlinear conductivity is conventionally defined as the field-dependent corrections to Ohm's law:

$$j_k = \sum_l \sigma_{kl} E_l + \sum_{l,m,n} \sigma_{3,klmn} E_l E_m E_n + ... \tag{2.12}$$

where σ_{kl} is the linear conductivity tensor, E the external electric field, and $\sigma_{3,klmn}$ the third order nonlinear conductivity tensor. The third order term is the first nonlinear contribution in most cases, since the second order response is symmetry-constrained [160] – we will not discuss it further here. Clearly if the electric field is oscillating at a frequency ω, the third order response will appear as a signal at 3ω, i.e. at the third harmonic frequency (as well as a small correction to the signal at ω, which is however hard to detect and not discussed further). This provides a possibility for sensitive measurement of the nonlinear response.

Except contact problems, a major difficulty in measuring nonlinear conductivity is sample heating. If the frequency of the applied electric field is small enough, Joule heating in a conductive sample will cause temperature oscillations and lead to a spurious third harmonic signal proportional to the temperature derivative of the linear conductivity [161, 162]. Conventionally the heating effects are decreased by using pulsed electric fields (with pulse duration ~ 1 ms), but it has been shown that this method does not completely eliminate the unwanted nonlinear signal [161, 162]. Hence we use a different approach: measurements at high frequencies, where the temperature of the sample cannot follow the field. The frequency must be greater than a characteristic thermal frequency of the sample, which can be estimated from the heat diffusion equation:

$$\nu_T \sim \frac{\kappa}{\rho c_p L^2} \tag{2.13}$$

where κ is the thermal diffusivity, ρ the density, c_p the specific heat, and L the linear dimension of the sample. For typical cuprates at 100 K the thermal frequency is of the order of 1 kHz, while our experimental setup operates in the MHz frequency range – clearly the sample temperature cannot follow the electric field in this case, thus eliminating spurious third harmonic signals.

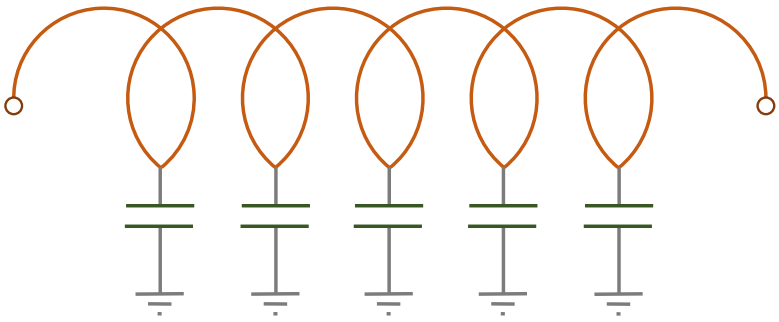

Figure 2.4: Lump element transmission line.

A tune-free excitation circuit can be made by connecting capacitors to the windings of a coil, creating a lump element transmission line whose impedance is matched to 50 Ω in a wide frequency range.

A special probe was designed for measuring nonlinear response, with two distinct detection methods. The measurement principle is always the same: one system of coils and capacitors provides the excitation field E, while a second system detects the third harmonic response in a selective manner. Of course, any other multiple of the excitation frequency can be used, in order to measure other nonlinear conductivity contributions. For the measurements we employ the same probe as for linear conductivity, but with a more complicated circuitry, as follows. Since the experiment operates in the RF range, we use a resonant LC circuit for detection, similar to linear conductivity and NMR described above. The excitation field is provided by a special non-resonant matched circuit, consisting of a distributed capacitance and inductance and effectively behaving as a transmission line (Fig. 2.4). In practice, this circuit is fabricated by winding a tight coil from varnish-insulated copper wire and painting it with conductive silver paint. The paint is then grounded, providing the needed distributed capacitance. The impedance of such a circuit can be finely tuned to the standard transmission line impedance of 50 Ω by varying the fraction of the coil surface covered by the silver paint. This results in a very low coefficient of reflection in a wide frequency range. We have managed to obtain a 50 Ω impedance from $\sim$ 1 to $\sim$ 100 MHz with the best circuits. Using a non-resonant excitation circuit instead of a resonant one eliminates cumbersome double tuning, but we note that it would be possible to perform the experiment with a double tuned resonant circuit, similar to two-channel NMR.

Two different detection/demodulation methods were used in nonlinear conductivity

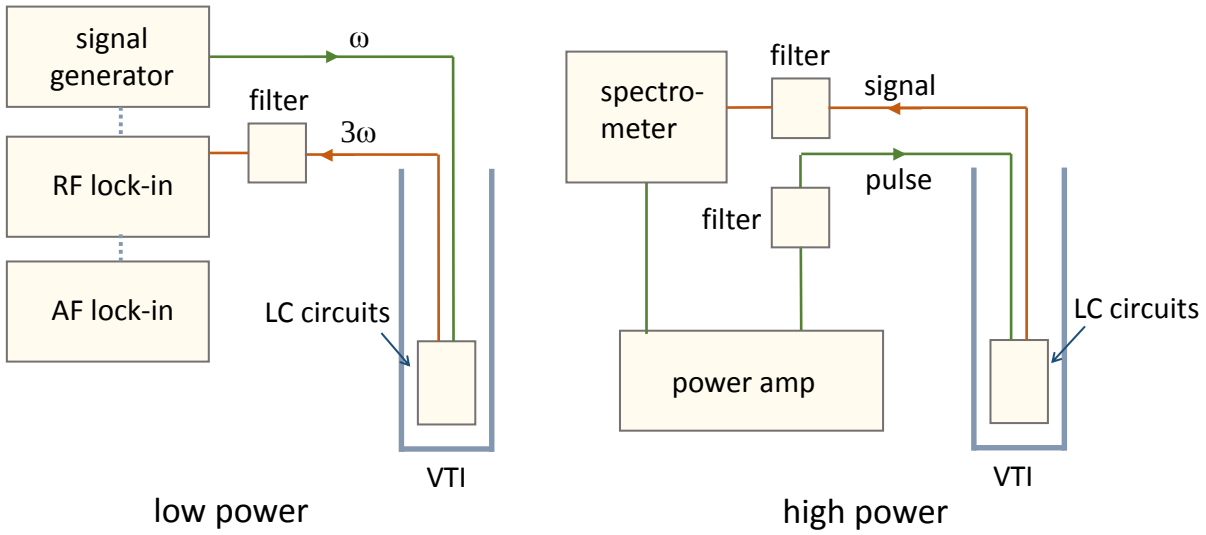

Figure 2.5: Schematic representation of the nonlinear conductivity measurement setup. Nonlinear conductivity is measured with two distinct methods: low power (left) and high power (right). The low-power setup uses a radio-frequency (RF) lock-in amplifier to detect the third harmonic response, and an audio-frequency (AF) modulation scheme for higher sensitivity. The high-power setup is essentially the same as an NMR experiment, with additional filtering for the first and third harmonic signals.

experiments, depending on the magnitude of the applied electric field. In both setups, it is important to filter out nonlinearities from the excitation signal (which can be large for high-power amplifiers) and to minimize the amount of excitation signal reaching the detector. Several commercial and custom-made low-pass and high-pass filters were used for this. A 7-pole Chebyshev filter was constructed to reject the first harmonic voltage at the detector, enabling a suppression ratio of ~ 80 dB. Single- and double-pole low-pass filters were used to clean the excitation signal. The applied filters minimize crosstalk between the excitation and detection circuits and avoid nonlinear amplification effects in the detection preamplifier.

The low-field experiment uses a continuous alternating voltage generator for the excitation field, and the third harmonic signal is detected with an RF lock-in amplifier (Fig. 2.5 left). The locking voltage is created from the excitation signal by a custom-made Schottky diode frequency tripler. For improved sensitivity, the RF signal can be amplitude-modulated at a frequency in the 100 Hz range, and the RF lock-in is then used as a demodulator whose output is fed to a second, low-frequency lock-in amplifier. This

configuration was used to investigate nonlinear response related to superconductivity, which is sizeable even for relatively low excitation fields.

The high-field experiment employs a conventional NMR spectrometer and power amplifier to generate strong excitation fields and detect the nonlinear response (Fig. 2.5 right). To avoid overheating of the coils and sample, the measurements are performed with pulsed excitations, similar to NMR (but with somewhat longer pulses of ~ 20 μs). Despite the extensive filtering, a nonlinear contribution is always present in the excitation signal due to the strong distortion in the power amplifier. To subtract these electronic nonlinearities and increase the sensitivity, the third harmonic is measured for different amplitudes of the excitation, and signal averaging is used (again in analogy to NMR). The high-field method was used for the investigation of charge order and stripe pinning nonlinearities, which require very high applied fields to be measurable with confidence.

2.2.4 Detecting nematic fluctuations.

We will apply nonlinear response to investigate two distinct phenomena in lanthanum-based cuprates: the formation and dynamics of charge order, and unconventional quasi-2D superconductivity, i.e. Berezinski-Kosterliz-Thouless physics. While nonlinear conductivity in BKT theory is relatively well studied (and was already investigated in LBCO-1/8), the response of different charge-ordered phases is less thoroughly understood. In known systems with charge-density waves, defects can pin the stripes, and a strong electric field causes stripe unpinning and hence nonlinear response [159, 163, 164]. The pinning in one-dimensional models is most simply described by the washboard model [159], where it is taken that the stripes move in a periodic pinning potential. If the external electric field is small, the stripes only oscillate around equilibrium positions of the potential; if the field is high enough, it is possible for the stripes to move from one potential well to the other, enhancing the conductivity of the system. Thus the response becomes strongly nonlinear in the vicinity of this threshold electric field. Of course, in an effectively two-dimensional system such as the cuprates, the potential landscape for stripe motion is much more complicated, and deformations of the stripes play an important role [40]. Nevertheless, qualitatively one would expect a similar threshold field to exist, which causes stripe depinning and leads to nonlinear response. This is one aspect of charge stripe nonlinearity that we will investigate with our experimental setup.

Furthermore, third order nonlinear conductivity is intimately related to higher-order

charge correlation functions, making it an interesting probe of hidden charge ordering. The relation between nonlinear response and four-point correlation functions was investigated extensively within the physics of glassy liquids [166–169] and spin glasses [165], with the establishment of an extended fluctuation-dissipation theorem (FDT) connecting third-order response to four-point correlation functions [166, 169]. A related framework was also used for the analysis of nonlinear magnetic susceptibility [170] in materials with possible spin nematic order, such as URu_2Si_2 [115]. Here we apply a similar formalism to establish a relation between third order nonlinear conductivity and charge nematic fluctuations.

As discussed in the Introduction, a charge nematic is an electronic ordered phase which breaks orientation symmetry, but keeps translational symmetry intact [40,105,106]. In the cuprates, the underlying lattice symmetry is ideally tetragonal (disregarding structural changes), and nematic order will lower it to orthorhombic – the x and y directions in the CuO_2 planes will not be equivalent. In contrast to charge stripes, a charge nematic is relatively insensitive to disorder [40], and was predicted to exist as a well-defined phase in underdoped cuprates. If this is true, a feature in the specific heat should be present, as well as a diverging susceptibility related to fluctuations of the nematic order parameter. We show that a direct correspondence exists between nematic fluctuations and third order nonlinear conductivity, as follows. Recent transport and optical studies show that the mobile holes in underdoped cuprates behave like a Fermi liquid [9, 171], so we base the discussion on Fermi liquid theory [172, 173]. The starting point is then the Landau-Silin transport equation for a charged Fermi liquid [173],

$$\frac{\partial \delta n_{\mathbf{k}}}{\partial t} + \mathbf{v}_{\mathbf{k}} \cdot \nabla_{\mathbf{r}} \delta \bar{n}_{\mathbf{k}} + e\mathbf{E} \cdot \nabla_{\mathbf{k}} n_{\mathbf{k}} = I\left(\delta \bar{n}_{\mathbf{k}}\right) \tag{2.14}$$

where $n_{\mathbf{k}}$ is the quasiparticle distribution (in dependence on the wave-vector $\mathbf{k}$), $n_{0,\mathbf{k}}$ the equilibrium distribution, $\delta n_{\mathbf{k}}$ and $\delta \bar{n}_{\mathbf{k}}$ the global and local deviations of the quasiparticle distribution from the equilibrium distribution respectively, $\mathbf{v}_{\mathbf{k}}$ the group velocity, $\mathbf{E}$ the screened electric field, and $I\left(\delta \bar{n}_{\mathbf{k}}\right)$ the collision integral. The local and global deviations are related via

$$\delta \bar{n}_{\mathbf{k}} = \delta n_{\mathbf{k}} - \frac{\partial n_0}{\partial \mathcal{E}_{\mathbf{k}}} \sum_{\mathbf{k}'} f_{\mathbf{k}\mathbf{k}'} \delta n_{\mathbf{k}'} \tag{2.15}$$

where $\mathcal{E}_{\mathbf{k}}$ is the dispersion and $f_{\mathbf{k}\mathbf{k}'}$ the quasiparticle interaction. Thus the full transport equation (2.14) is an integrodifferential equation and unsolvable in the general case, so we focus our attention on the simple limiting cases still relevant for experiment. Most

importantly, the electric fields we apply are almost constant in space (compared to microscopic length scales such as the inverse of the Fermi wavevector), and we thus drop the term containing spatial derivatives of the distribution function. This corresponds to writing the electric field in Fourier components with wavevector $\mathbf{q}$, and taking the limit $q \to 0$. Furthermore, we take the quasiparticle Fermi surface to be isotropic – this is certainly not quantitatively true in cuprates, but makes the calculations tractable; but we will argue below that the qualitative conclusions do not depend on the precise form of the dispersion relation. Finally, we employ the relaxation time approximation, wherein the collision integral is modelled as a simple linear relaxation process.

Before calculating the nonlinear response, we first discuss the textbook case of linear conductivity [173]. For an isotropic Fermi surface, the external field $\mathbf{E}$ gives a convenient axis of symmetry, so that $\delta n_{\mathbf{k}}$ and $\delta \bar{n}_{\mathbf{k}}$ can be expanded in spherical harmonics with the polar angle θ being between $\mathbf{E}$ and $\mathbf{k}$. Since we are interested in planar response, we can use a Legendre polynomial expansion in place of the full spherical harmonics, yielding

$$\delta n_{\mathbf{k}} = \sum_l \delta n_l P_l(\cos\theta),\ \delta n_{\mathbf{k}} = \sum_l \delta \bar{n}_l P_(\cos\theta) \tag{2.16}$$

where $P_l(\cos\theta)$ are Legendre polynomials of order l. In a degenerate Fermi liquid, all relevant quantities are restricted to the vicinity of the Fermi surface, and thus the quasiparticle interaction $f_{\mathbf{k}\mathbf{k}'}$ only depends on the angle between $\mathbf{k}$ and $\mathbf{k}'$ in the isotropic case. After expanding the interaction into Legendre polynomials as well, we find that the relation (2.15) between $\delta n_{\mathbf{k}}$ and $\delta \bar{n}_{\mathbf{k}}$ takes the simple form

$$\delta \bar{n}_l = \left(1 + \frac{F_l}{2l+1}\right) \delta n_l = \eta_l \delta n_l \tag{2.17}$$

where F_l is the l-th dimensionless Legendre component of $f_{\mathbf{k}\mathbf{k}'}$ and η a shorthand. The collision integral in the relaxation time approximation may also be expanded in a similar way [173],

$$I\left(\delta \bar{n}_{\mathbf{k}}\right) = -\sum_l \Gamma_l \delta \bar{n}_l \tag{2.18}$$

where Γ_l are the relaxation rates for the l-th component of the nonequilibrium distribution. In the simplest case, they are all equal and $\Gamma_l = \Gamma$. We will use the constant Γ approximation for simplicity, keeping in mind that it is easy to reintroduce different Γ_l if necessary. The linear response to an oscillating applied field $\mathbf{E}(\omega) = \mathbf{E}e^{i\omega t}$ can now be simply calculated by assuming that $\nabla_{\mathbf{k}} n_{\mathbf{k}} \approx \nabla_{\mathbf{k}} n_0 = \mathbf{v}_{\mathbf{k}} \partial n_0 / \partial \mathcal{E}_{\mathbf{k}}$ in the Landau-Silin equation. Since in an isotropic Fermi liquid the group velocity is along $\mathbf{k}$, $\mathbf{E}\cdot\mathbf{v}_{\mathbf{k}} = E v_{\mathbf{k}} \cos\theta = E v_{\mathbf{k}} P_1(\cos\theta)$

and the transport equation becomes

$$\sum_l \left(\frac{\omega}{\eta_l} + i\Gamma \right) \delta\bar{n}_l P_l(\cos\theta) = ieEv_{\mathbf{k}} \frac{\partial n_0}{\partial \mathcal{E}_{\mathbf{k}}} P_1(\cos\theta) \tag{2.19}$$

where we have incorporated the relation between $\delta\bar{n}_l$ and δn_l and used the fact that $\delta\bar{n}$ oscillates at the same frequency as the external field. Clearly the only finite component of $\delta\bar{n}_l$ is $l = 1$, as it should be – the external field induces a vector-like deviation from equilibrium, creating a current flow (Fig. 2.6). It is trivial to solve equation (2.19) to obtain

$$\delta\bar{n}_1^{(1)} = \frac{ieEv_{\mathbf{k}}}{\omega/\eta_1 + i\Gamma} \frac{\partial n_0}{\partial \mathcal{E}_{\mathbf{k}}} \tag{2.20}$$

where we have highlighted the fact that $\delta\bar{n}_1^{(1)}$ is the linear response component. The linear conductivity may now be found from the standard relation for the charge current,

$$\mathbf{j} = \sum_{\mathbf{k}} \mathbf{v}_{\mathbf{k}} \delta\bar{n}_{\mathbf{k}} \tag{2.21}$$

giving the well-known Drude form of frequency-dependent conductivity [173].

To go beyond linear response, one step in the above discussion must be modified: if the nonequilibrium distribution is a nonlinear function of the external field, we must not approximate $\nabla n_{\mathbf{k}}$ in the Landau-Silin equation. To solve this general, nonlinear case in a systematic way, we investigate the effect of slowly turning on the electric field by multiplying it with a small parameter [174]: $\mathbf{E} \to \lambda\mathbf{E}$. When $\lambda = 1$, the full transport equation is recovered. The parameter λ now enables a systematic expansion of $n_{\mathbf{k}}$,

$$\delta\bar{n}_{\mathbf{k}} = \delta\bar{n}_{\mathbf{k}}^{(0)} + \lambda\delta\bar{n}_{\mathbf{k}}^{(1)} + \lambda^2\delta\bar{n}_{\mathbf{k}}^{(2)} + \lambda^3\delta\bar{n}_{\mathbf{k}}^{(3)} + ... \tag{2.22}$$

and similar for $\delta n_{\mathbf{k}}$. The zeroth-order term may be incorporated into $n_{\mathbf{0},\mathbf{k}}$ without loss of generality, and thus will not be considered in the calculation. Inserting the expansion (2.22) into the transport equation with included $\lambda\mathbf{E}$, we may derive a system of equations for the different expansion terms by noting that the original equation must be valid for any value of the parameter λ. Collecting terms with the same power of λ, we obtain

$$\frac{\partial \delta n_{\mathbf{k}}^{(1)}}{\partial t} + \Gamma\delta\bar{n}_{\mathbf{k}}^{(1)} = e\mathbf{E} \cdot \nabla_{\mathbf{k}} n_0 \tag{2.23a}$$

$$\frac{\partial \delta n_{\mathbf{k}}^{(2)}}{\partial t} + \Gamma\delta\bar{n}_{\mathbf{k}}^{(2)} = e\mathbf{E} \cdot \nabla_{\mathbf{k}} \delta n_{\mathbf{k}}^{(1)} \tag{2.23b}$$

$$\frac{\partial \delta n_{\mathbf{k}}^{(3)}}{\partial t} + \Gamma\delta\bar{n}_{\mathbf{k}}^{(3)} = e\mathbf{E} \cdot \nabla_{\mathbf{k}} \delta n_{\mathbf{k}}^{(2)} \tag{2.23c}$$

and continuing for higher-order contributions; to evaluate third order response, the above system is sufficient. If we take the electric field to be oscillating as $e^{i\omega t}$, clearly the $\delta n_k^{(p)}$ terms will oscillate at $p\omega$, as seen from the recursive nature of the system (2.23). The first equation corresponds to linear response and has been solved above. To obtain the second-order contribution, we may again employ the Legendre polynomial expansion, noting that the right-hand side of eq. (2.23b) contains $\mathbf{E}\cdot\nabla_{\mathbf{k}}Ev_{\mathbf{k}}P_1(\cos\theta)$. After evaluating the gradient in terms of Legendre polynomials, the second-order equation becomes

$$\sum_l\left(\frac{2\omega}{\eta_l}+i\Gamma\right)\delta\bar{n}_l^{(2)}P_l(\cos\theta)= \frac{1}{3\eta_1}\frac{(ie)^2E^2}{\omega/\eta_1+i\Gamma}\frac{\partial n_0}{\partial\mathcal{E}_{\mathbf{k}}}\left[2\left(\frac{\partial v_k}{\partial k}-\frac{v_k}{k}\right)P_2(\cos\theta)+\left(\frac{\partial v_k}{\partial k}+2\frac{v_k}{k}\right)P_0(\cos\theta)\right] \quad (2.24)$$

This expression is important for us because the second-order correction is bilinear in the external field, meaning that it represents the induced quadrupolar charge density, which is closely related to the nematic order parameter. There are two contributions to $\delta\bar{n}^{(2)}$, $l=0$ and $l=2$, corresponding to the two irreducible deformations of a circular Fermi surface induced by a uniaxial bilinear electric field. Such contributions are well known in the analysis of electronic Raman scattering, where the response is bilinear in the applied vector potential [91]. The $l=0$ term is referred to as $\mathrm{A_{1g}}$ and represents an isotropic expansion or contraction, while the $l=2$ or $\mathrm{B_{1g}}$ term is a d-wave quadrupolar deformation (Fig. 2.6). The third irreducible representation, $\mathrm{B_{2g}}$, is obtained as a rotation of $\mathrm{B_{1g}}$ by $\pi/4$, and in our geometry does not explicitly enter the transport equation (2.24). A nematic order parameter has $\mathrm{B_{1g}}$ symmetry, and thus the $l=2$ contribution directly represents the field-induced nematic density. The induced density is

$$\langle\rho_Q\rangle=\sum_{\mathbf{k}}\delta n_2^{(2)}=\frac{2}{3\eta_1\eta_2}\frac{1}{\omega/\eta_1+i\Gamma}\left|k\frac{\partial}{\partial k}\frac{v_k}{k}\right|_{k_F}E^2=\chi_N E^2 \quad (2.25)$$

where k_F is the Fermi wave-vector, and we have defined a nematic susceptibility χ_N as a measure of the softness of the system with respect to nematic fluctuations. In Fermi liquid theory, a spontaneous nematic deformation of the Fermi surface occurs when the $l=2$ channel of the quasiparticle interaction satisfies the Pomeranchuk instability condition $\eta_2=0$ [175]. Clearly $\chi_N\sim 1/\eta_2$, implying that the nematic susceptibility diverges at the Pomeranchuk nematic transition, as should be expected.

When calculating the second-order conductivity using expression (2.21), the angular factors make the Fermi surface integral disappear, implying that $\mathbf{j}^{(2)}=0$. This is in line with general symmetry constraints, since no second order response can be present if the

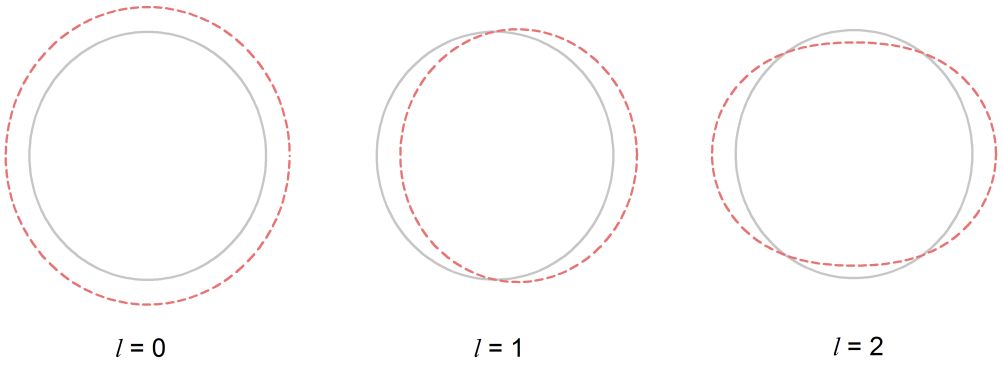

Figure 2.6: Fermi surface deformations.
Deformations of a circular Fermi surface induced by an applied field. The $l = 0$ deformation amounts to a homogeneous expansion or contraction, $l = 1$ is a vector deformation (leading to a charge current), and $l = 2$ is a quadrupolar deformation, which can be viewed as electric field-induced nematic order.

system is time reversal symmetric. The quadrupular density thus cannot be measured in a conductivity experiment (but is detectable with other probes, such as Raman scattering [112] and NQR [114]). However, it is possible to measure the nematic susceptibility χ_N. We have seen above that when the system approaches a nematic instability at $\eta_2 = 0$, it will become soft with respect to the field-induced nematic perturbations, and the corresponding susceptibility will diverge. We now show that the third-order conductivity is proportional to the nematic susceptibility, by employing the recursion (2.23) one more time. After inserting $\delta\bar{n}^{(2)}$, the equation of motion becomes

$$\sum_l \left(\frac{3\omega}{\eta_l} + i\Gamma\right) \delta\bar{n}_l^{(3)} P_l(\cos\theta) = \frac{1}{3\eta_1} \frac{(ie)^3 E^3}{\omega/\eta_1 + i\Gamma} \frac{\partial n_0}{\partial \mathcal{E}_{\mathbf{k}}} \left[\frac{6}{5}\frac{1}{\eta_2}\frac{1}{\omega/\eta_2 + i\Gamma}\frac{1}{k^2}\frac{\partial}{\partial k}k^3\frac{\partial}{\partial k}\frac{v_k}{k} P_3(\cos\theta) + \left(\frac{4}{5}\frac{1}{\eta_2}\frac{1}{\omega/\eta_2 + i\Gamma}k^3\frac{\partial}{\partial k}\frac{1}{k^2}\frac{\partial}{\partial k}\frac{v_k}{k} + \frac{1}{\eta_0}\frac{1}{\omega/\eta_0 + i\Gamma}\frac{\partial}{\partial k}\frac{1}{k^2}\frac{\partial}{\partial k}v_k k^2\right) P_1(\cos\theta)\right] \quad (2.26)$$

The only terms in $\delta\bar{n}^{(3)}$ are then those with $l = 1$ and $l = 3$. In calculating the corresponding conductivity through relation (2.21), only the $l = 1$ term remains after Fermi surface integration; taking the limit $\omega \to 0$ appropriate for our experiment, we obtain

$$\sigma_3 = \frac{e^4}{3\eta_1\Gamma}\left(\frac{8}{15}\frac{1}{\eta_2}\left|v_k k^3 \frac{\partial}{\partial k}\frac{1}{k^2}\frac{\partial}{\partial k}\frac{v_k}{k}\right|_{k_F} + \frac{2}{3}\frac{1}{\eta_0}\left|\frac{v_k}{k^2}\frac{\partial}{\partial k}v_k k^2\right|_{k_F}\right) \quad (2.27)$$

The third order conductivity contains two contributions: one proportional to $1/\eta_0$, which is always finite since $\eta_0 > 0$ is the condition for a finite Fermi liquid compressibility, and

the other proportional to $1/\eta_2$, which becomes singular at the nematic transition. Thus in the vicinity of a nematic transition, $\sigma_3 \sim \chi_N \sim 1/\eta_2$ (with a complicated prefactor depending on the form of the quasiparticle dispersion), and the third order conductivity can be used for detecting the nematic Fermi surface instability. We note that instabilities in higher l channels can also be investigated with the corresponding nonlinear conductivity contributions.

In deriving the relation between σ_3 and the nematic susceptibility, we have used several simplifying assumptions: a spherical Fermi surface, negligible spatial variation of the quasiparticle response, and of course the basic assumption that Fermi liquid theory is applicable. Recent transport and optical experiments show that the latter is indeed the case in cuprates [4, 9]. However, the Fermi surface certainly is not spherical; yet the main conclusion that σ_3 is sensitive to nematic fluctuations should remain true. A Fermi surface shape which depends on θ precludes the spherical harmonic expansion of $\delta n_{\mathbf{k}}$, $\delta \bar{n}_{\mathbf{k}}$ and $f_{\mathbf{k}\mathbf{k}'}$, implying that in the general case one must solve an integral equation of motion for $\delta \bar{n}_{\mathbf{k}}$ [173]. But even then the basic idea of a recursive calculation of higher-order response remains valid: indeed, the system (2.23) does not explicitly include the l-expansion. Any Fermi surface shape with a four-fold symmetry can undergo a spontaneous nematic deformation for some value of the quasiparticle interaction components – a generalized Pomeranchuk criterion can be obtained in two spatial dimensions [176]. For symmetry reasons, it is always possible to decompose the second-order response $\delta n_{\mathbf{k}}^{(2)}$ into irreducible contributions and make an identification with the quadrupolar density similar to eq. (2.25). The nematic susceptibility will then again diverge at the Fermi surface instability, but with a more complex dispersion-dependent prefactor. In turn, the third order response will always have a component proportional to the induced nematic density, simply because of the nature of the recursive calculation. Thus σ_3 remains a probe of divergent nematic fluctuations in the general case as well. We remark that the same relation between third order response and fluctuations of the nematic order parameter was derived on completely different grounds for molecular liquids, within nonlinear optics [177].

2.3 Specific heat.

We have seen in the preceding sections that nuclear magnetic (and quadrupole) resonance can be used to gain microscopic insight into the electronic physics of cuprates, and that contact-free linear and nonlinear conductivity measurements give information on superconducting and charge fluctuations. To complete our experimental insight into charge order formation, we use the simplest bulk thermodynamic probe: specific heat. As discussed in the Introduction, on theoretical grounds we expect the charge stripes to become glassy because of disorder, but a precursor charge nematic phase should remain well-defined. Detecting the associated phase transition will be the main goal of the specific heat investigation.

Due to the small size of the single crystal samples we are working with, a special method had to be employed for the measurement of their specific heat. Standard methods such as pulse calorimetry are not sensitive enough to detect the small features related to nematic order, mainly because the transitions appear at rather high temperatures of ~ 100 K (or higher). The lattice specific heat of the samples is large at these temperatures, making the electronic contributions appear as small peaks on a large background. To alleviate this problem, we use a variant of the well-known differential scanning calorimetry (DSC) widely used in chemistry and material science [178], but modified for small samples and with increased sensitivity. A similar experimental setup was developed for studying vortex transitions in cuprate superconductors [179].

The measurement principle is very simple: the investigated sample and a reference sample are mounted on two small temperature sensors – we use standard platinum resistors. The resistors are weakly thermally coupled to a platform, whose temperature is sweeped in time. The temperatures of the resistors lag behind the platform temperature in proportionality with the specific heat of the samples. By connecting the resistors in a bridge configuration, a precise determination of the specific heat becomes possible. If the mass of the platform is much larger than the sample and resistor mass (which is easily achieved in practice) and if the entire system is in high vacuum, it is straightforward to show that the temperature difference between the two resistors is

$$\Delta T = \frac{\dot{T}}{\Lambda} (C_0 - C_p) \tag{2.28}$$

where $\dot{T}$ is the time derivative of the platform temperature, Λ the heat conductivity of the link between platform and resistors (assumed to be equal for both resistors), C_0

the specific heat of the reference, and C_p the sample specific heat. In the experiment, the two platinum resistors are connected as one half of a Wheatstone bridge, with the other half consisting of two high-precision low temperature coefficient chip resistors. The bridge voltage is directly proportional to ΔT in a wide temperature range where the temperature coefficient of platinum is nearly constant. If the bridge is excited by an alternating voltage source, a phase sensitive measurement of the bridge voltage is possible with a lock-in amplifier, enabling high sensitivity. Typically a temperature difference ΔT less than 10 μK can be detected in this way.

While the specific heat measurement method described above is simple in essence, several experimental difficulties make it more challenging than it might appear. The most important is the fact that the temperature difference ΔT is very sensitive to the instantaneous value of the platform temperature time derivative. This means that even small oscillations of the platform temperature will be visible in the signal and obscure real features in the sample specific heat. A conventional temperature regulation of the platform includes a closed-loop PID temperature controller, with a finite density of thermometer calibration points and linear interpolation between them; thus a programmed linear temperature sweep will introduce small platform temperature oscillations due to the discontinuous interpolation. Other effects such as helium bubbling and thermal contact imperfections can cause temperature oscillations as well, but the controller-induced effect is repeatable and especially difficult to remove. To eliminate it, we used open-loop control, i.e. simply sweeping the heater power and measuring the resistivity of the platform temperature sensor. The temperature was calculated from the resistivity using a continuous calibration curve, thus removing the need for interpolation. This procedure makes the platform temperature time dependence almost completely smooth in the range between $\sim$ 10 K and $\sim$ 200 K. At lower temperatures, the resistivity of the platinum sensors saturates and sensitivity is lost, while at higher temperatures many common materials used in probe construction (such as greases, epoxy, teflon and GE varnish) have phase or glass transitions, introducing further artefacts. Fortunately, the most interesting phenomena in our investigations turned out to occur within the smooth range.

A dedicated experimental probe was constructed for the specific heat measurements (but also used in other investigations). To be useful in a wide range of experiments, it was designed to be able to reach temperatures below 1.5 K in a liquid helium bath. To reach temperatures below the normal helium boiling point of 4.2 K, the helium is

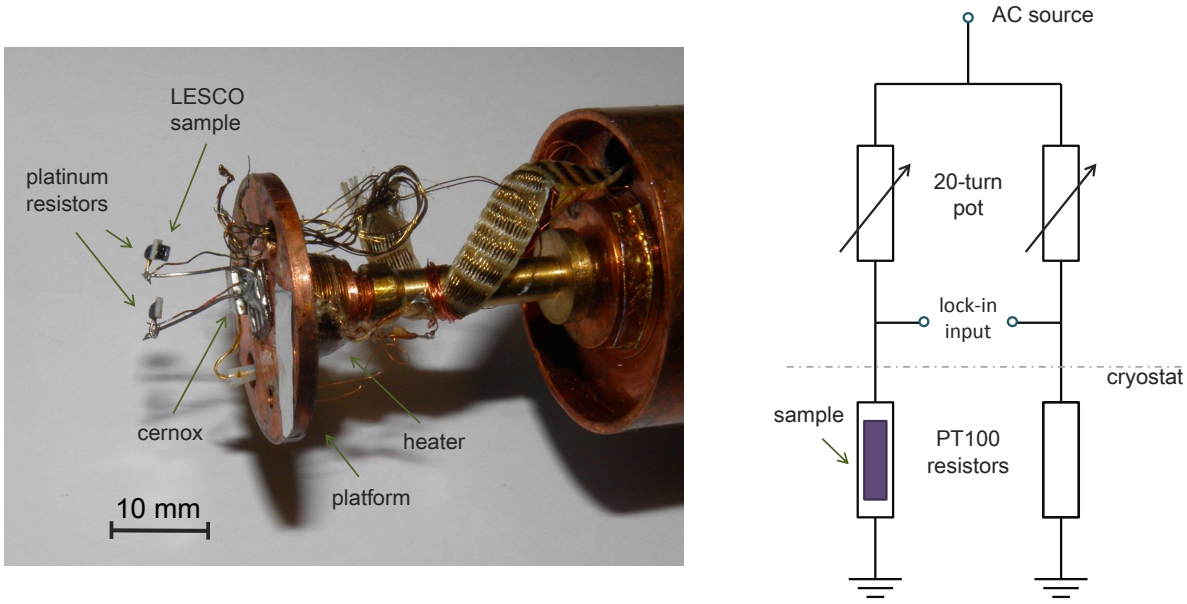

Figure 2.7: Setup for specific heat measurements.
The specific heat probe head is shown (left) with two equal platinum resistance thermometers and a LESCO single crystal sample [181]. The resistors are connected in a simple bridge circuit (right), enabling sensitive bridge voltage measurements with a lock-in amplifier.

sucked through a long capillary tube into a pot with a volume of several cm^3, where it is cooled by lowering the vapour pressure [180]. The probe design thus requires two separate tubing systems: one for helium pumping, and one for the vacuum containing the pot and sample platform. A photograph of the sample platform and 1K pot is shown in Fig. 2.7; see Appendix C for design schematics. Some specific design points include the conical grease seal between the brass cap and the probe body, the helium capillary made of a stainless steel tube with 1 mm outer diameter and a constantan wire fitted inside the tube to decrease its cross-section, and the use of multiple thermal anchoring points throughout. The thermal contact between the pot and the sample platform is a thin brass neck with counter-threads on both sides, enabling simple replacement if a neck with different thermal conductivity is needed. The platform temperature is measured with a calibrated low-magnetoresistance cernox sensor. A foil heat shield is wrapped around the sample space, minimizing the effects of thermal radiation.

The simple measuring principle and carefully considered methodology enable highly sensitive specific heat measurements. A fortunate circumstance provides an internal cali-

bration and sensitivity standard in experiments on co-doped lanthanum cuprates. As we shall see in the next chapter, they contain a structural phase transition relatively close to the interesting charge stripe and nematic order. Detecting this transition gives an independent measure of the sensitivity of the setup, which is shown to be adequate for studying small features in the specific heat and usable for many other materials.

2.4 Samples.

Before discussing the results of our measurements, a short overview of the sample preparation methods and samples employed in the investigations is in order. We use materials from two closely related cuprate families: LBCO and LESCO. Their structure is similar, and both are derived from the 214 lanthanum cuprate La_2CuO_4, but the doping ions are slightly different. LBCO is doped simply by substituting lanthanum for barium, while in LESCO a fraction of the lanthanum is substituted by isovalent europium, and the hole doping is provided by strontium. The europium ion is smaller than lanthanum and stabilizes the low-temperature tetragonal (LTT) phase, which has a profound influence on electronic properties (as we shall see in the next chapter).

LBCO and LESCO samples were high-quality single crystals with masses of the order of 10 mg. All samples were grown with the traveling floating zone method, wherein a system of high-power lamps and mirrors focuses light on a small portion of a powdered sample rod [182]. The powder then melts locally, and if the rod is slowly translated, recrystallization of the powder at the edges of the floating zone creates a single crystal. The technique is suitable for growing 214 cuprates because of the non-volatility of the starting oxides and their substitutional doping. Typical growing speeds are below 1 mm/h, and large homogeneous crystals can be obtained. Both the LBCO and LESCO samples used here were employed in numerous previous investigations and characterized in detail. LESCO was grown by Udo Ammerahl in the group of A. Revcolevschi at Universite Paris-Sud, and the europium and strontium concentrations were determined independently by energy-dispersive X-ray analysis. The same crystals were used in previous NMR, X-ray scattering [28, 29] and transport [183] studies. The LBCO crystal was grown at Brookhaven National Laboratory, and samples from the same rod were characterized in previous magnetization [86], transport [85,86] and scattering [37] experiments.

Chapter 3

Results and discussion

Our combination of experimental techniques provides unique insights into the formation and dynamics of charge order in the cuprates, and its interaction with superconductivity. Before analysing the results of measurements and comparing them to recent theoretical concepts, we introduce the particular compounds used as model systems for the investigation of cuprates in general. The first superconducting cuprates to be discovered were lanthanum-based systems. Charge stripe order was first found in lanthanum cuprates as well. Yet due to strong spin fluctuations [60, 65, 66] and relatively small charge stripe amplitudes, insight into the local properties as well as into the evolution of the stripes is incomplete in these compounds. Importantly, it has been shown recently that other prominent cuprate families display charge stripe features [26–28, 30–33, 57, 61, 62], meaning that an understanding of charge order and its interaction with superconductivity is relevant to cuprate physics in general. Lanthanum cuprates are single-layer compounds, i.e. their structure has only one CuO_2 motif per unit cell, making them simpler than other prominent families such as YBCO. Furthermore, they are doped by ionic substitution (and not by oxygen interstitials), which makes the doping easier to control and determine, but introduces relatively strong point charge disorder. Last but not least, in lanthanum cuprates such as LBCO the interaction between charge stripes and superconductivity seems to be especially pronounced, inducing an unconventional two-dimensional superconducting state and suppressing bulk superconductivity [85, 86]. It is still unclear whether these effects are properly understood and whether they are important for other cuprates [39, 185]. Thus lanthanum-based compounds are good model systems for investigating the formation of charge stripes and their interplay with other electronic ordering tendencies.

This chapter is divided into three parts, answering three important questions:

- how are charge stripes formed in disordered cuprate systems?
- what are their local and dynamic properties?
- how do they interact with superconductivity?

Answering these questions will shed light on other fundamental issues of cuprate physics, such as the universality of charge order, the nature of the pseudogap state, and properties of the superconducting pairing mechanism.

3.1 The emergence of charge order.

Theoretical analysis [40, 105] suggests that charge stripe order is very sensitive to electrostatic disorder, due to the small energy cost of defects in the ordered stripe structure. Vanishingly small levels of disorder should thus destroy true long-range stripes, and make the transition into the stripe state similar to a glass transition or crossover. Neutron and X-ray scattering experiments in cuprates consistently show that the charge stripe order has small coherence lengths [28, 31, 37], indicating that long-range order is never established; also, local probes such as lanthanum NMR detect a glassy slowing down of the spin dynamics [50, 66, 111, 184], which is related to the disordered stripe structure. Thus the influence of disorder on the charge stripes is experimentally rather well documented. Intriguingly, it is predicted that a precursor ordered phase – the charge nematic – is mostly unaffected by disorder, appearing through a well-defined phase transition [40]. The charge nematic, however, does not break translational symmetry and is rather difficult to detect experimentally. Even more exotic ordered phases are predicted to exist between an ordinary Fermi liquid and the charge nematic, such as the loop metal state which does not break any spatial symmetry [186, 187]. Which experimental probes can then be used to investigate these precursors to charge stripe order? Firstly, if the charge nematic is a thermodynamically well-defined phase, the corresponding phase transition must be visible in the specific heat. Of course, a specific heat anomaly in itself cannot give insight into the microscopic nature of the transition, so other probes are needed to provide complementary information. In chapter 2 we have shown that third order nonlinear conductivity is sensitive to nematic fluctuations, which should diverge at the transition from Fermi liquid – or some other, more exotic phase – to the charge nematic phase. Finally,

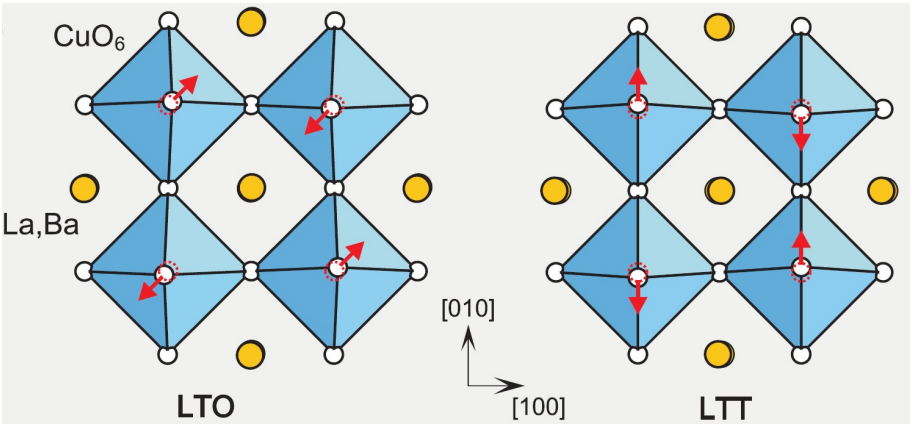

Figure 3.1: The LTT structural transition.
The CuO_2 planes and adjacent La,Ba layers in LBCO are shown from above, indicating the shifts of the CuO_6 octahedra in the low-temperature orthorhombic (LTO, left) and low-temperature tetragonal (LTT, right) phases. The LTT transition then involves a rotation of the octahedra by $\pi/4$. Adapted from [111].

charge nematic order has been shown to induce spin fluctuations in systems close to an antiferromagnetic ground state (such as that observed in the cuprates) [188], implying that a signature in nuclear magnetic resonance should be present. Thus a combination of specific heat, nonlinear conductivity, and NMR/NQR should enable a detection of charge stripe precursor phases, and make their identification possible.

For the investigation of charge stripe formation we use the europium co-doped lanthanum cuprate $La_{1.8-x}Eu_{0.2}Sr_xCuO_4$ (LESCO) as a model system. The most important reason for using LESCO is structure-related. All lanthanum-based cuprates possess a structural transition [91, 190] which involves a tilt of octahedra with copper atoms in their center (Fig. 3.1). The structure above this transition is referred to as low temperature orthorhombic (LTO), while below the transition a low temperature tetragonal (LTT) structure appears. The LTO-LTT transition temperature T_{LTT} depends on doping and co-doping of the compound, and in several materials such as LBCO interferes with the charge stripe order [37, 86]. LESCO is unique in that T_{LTT} is strongly increased by Eu co-doping, which stabilises the LTT structure [18, 191]. Recent resonant x-ray and neutron scattering studies show that the temperatures where charge and spin stripes appear in LESCO are well-separated from the structural transition across the phase diagram [28, 29, 192]. It thus provides the opportunity to investigate charge stripe formation in the tetragonal setting, without interference from structural effects. Another reason for

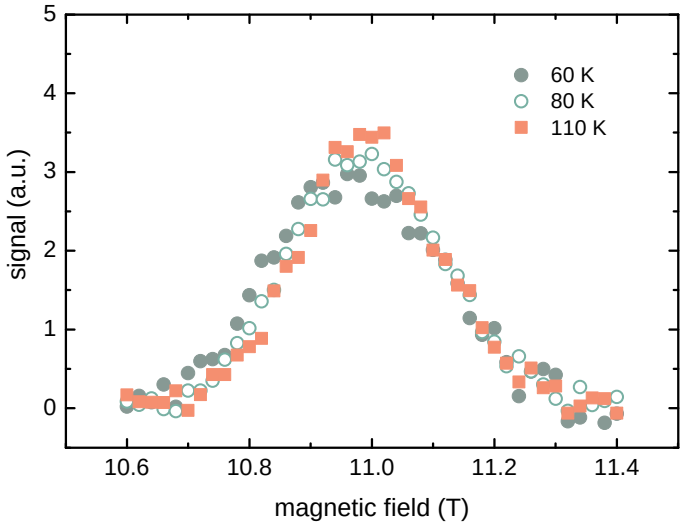

Figure 3.2: The NMR spectrum of LESCO.
Field-sweep spectrum [181] of the quadrupolar satellite of ^{63}Cu at 140 MHz in dependence on temperature, showing that the linewidth does not change appreciably in the temperature range where charge nematic order appears. The spectra are normalized to the same surface area.

using LESCO as a model system is that the superconductivity in this system is rather strongly suppressed (which will also be interesting for us further along), resulting in a wide temperature range where the charge and related spin stripes can be studied without having to consider the interplay with superconductivity.

To follow the evolution of charge stripes and precursor order in both doping and temperature, we use three different LESCO samples in the underdoped region where charge stripes appear. The first indication that a precursor phase exists in this system comes from measurements of copper NQR signal intensity in dependence on temperature. It has been known that in powder samples the NQR and NMR signal intensity drops when charge stripe order appears – an effect known as wipeout, as discussed in the Introduction. In previous work, measurements of the net intensity were performed by integrating the entire NMR or NQR lineshape [47, 63–65], and extrapolating the spin-spin decay to zero echo time to compensate for T_2. Yet such measurements are relatively insensitive because of the large linewidths, while the linewidths themselves do not significantly depend on temperature. The ^{63}Cu quadrupolar satellite in LESCO with $x = 0.125$ is shown in Fig. 3.2 at three different temperatures, demonstrating that the lineshape is approximately temperature-independent. It is therefore acceptable to determine the net signal intensity

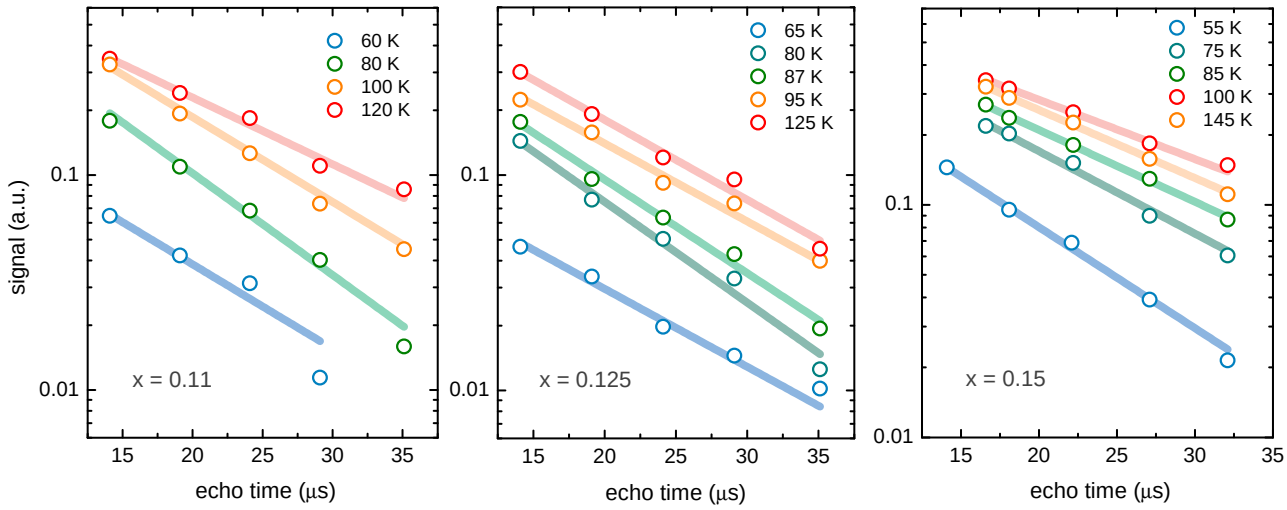

Figure 3.3: Spin-spin relaxation of LESCO.
Raw spin-spin relaxation data [181] are shown for samples with three hole doping concentrations: $x = 0.11$ (left), $x = 0.125$ (middle) and $x = 0.15$ (right). The relaxation is exponential at all temperatures shown here, and a gradual signal wipeout is observed with decreasing temperature, as an overall reduction of the signal intensities.

by measuring the spin-spin decay at the peak of the NMR or NQR line, without integrating the entire lineshape. As we shall show, the signal wipeout is significantly larger than the small changes induced by lineshape changes.

Spin-spin relaxation was measured in dependence on temperature for the pure NQR copper lines in the three compounds with different doping. In addition, measurements in the sample with $x = 0.125$, where the stripe order is most pronounced, were performed in NMR at external fields of 6 T and 12 T. Representative spin-spin decay curves are shown in Fig. 3.3, where it is clear that the decay is exponential in the entire investigated temperature range. The NMR measurements have a much better signal-to-noise ratio because the measurement frequency ω_0 is ~ 4 times larger than in NQR, and the sensitivity of the experiment is roughly proportional to ω_0^2. In all measurements it is clear that a partial signal wipeout appears at temperatures close to 100 K, while a strong signal decrease occurs $\sim$ 20 K below that. When the signal intensity is compensated for the Boltzmann factor and plotted in dependence on temperature, the two wipeout features are nicely visible in all samples (Fig. 3.4). The lower temperatures where a signal decrease is observed closely correspond to the temperatures T_{CO} where resonant X-ray scattering experiments first detect charge stripe order [29] (marked in Fig. 3.4). Yet the wipeout

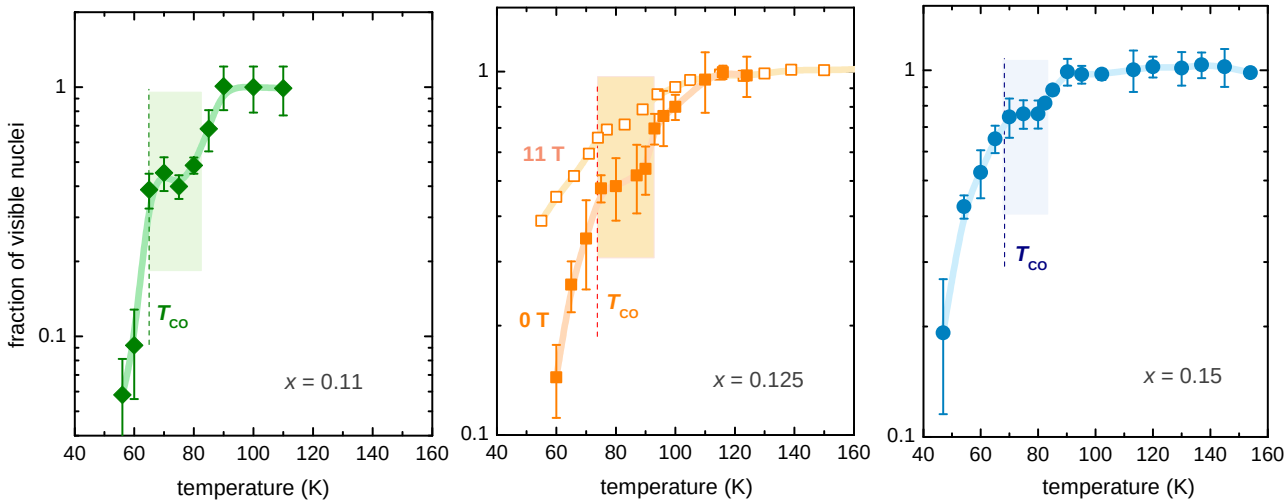

Figure 3.4: Copper NQR and NMR signal wipeout in LESCO.
Temperature dependence of the ^{63}Cu NQR signal intensity for LESCO with three doping concentrations [181]. The intensities are obtained by extrapolating spin-spin decay curves to zero echo delay times, and by compensating for the usual Boltzmann temperature factor. A wipeout plateau is seen in all three samples above the temperatures T_{CO} where charge stripes are first seen in scattering experiments [29].

plateau extends at least 20 K above T_{CO}, indicating that a precursor phase appears between the Fermi liquid at high temperatures and charge order below T_{CO}. Note that the wipeout fractions in the plateau are already rather high, ranging from 0.5 in the sample with $x = 0.11$ to 0.8 in the sample with $x = 0.15$. Interestingly, the wipeout is stronger in pure NQR than in NMR, indicating that the relatively large external magnetic field influences the fluctuations responsible for the signal decrease. We will further explore this effect in measurements on the closely related LBCO.

The observation of the wipeout plateau is encouraging, and enables us to extract a new characteristic temperature T_{CN} corresponding to the high-temperature step in the signal intensity. If this temperature signifies a true phase transition, a feature must be present in the specific heat close to T_{CN}. Using the sensitive specific heat measurement method described in Chapter 2, we have indeed observed a peak at T_{CN} in samples with doping $x = 0.125$ and $x = 0.15$ (Fig. 3.5). In contrast, no recognizable peaks are present near T_{CO}, in agreement with the notion that the transition to the stripe phase is smeared out. A glass-like broad feature could be expected instead, but the resolution of our method is not large enough to observe it. The height of the peak at T_{CN} can be compared to a similar feature observed at the structural transition temperature

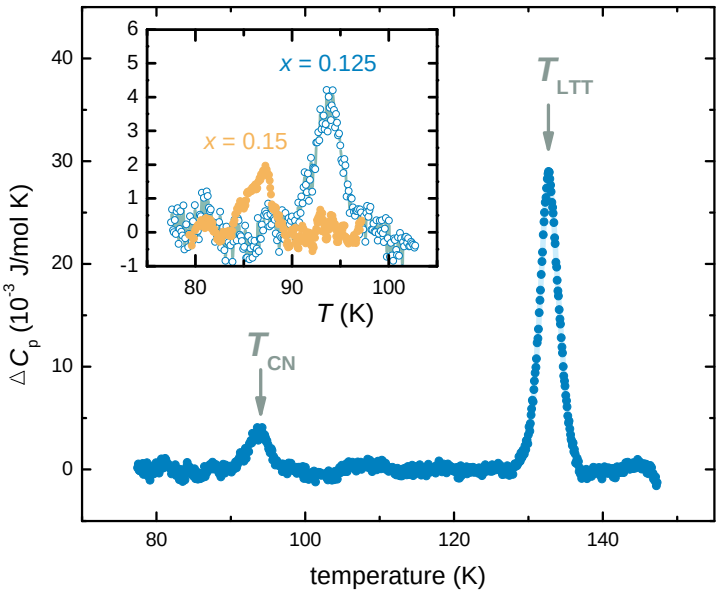

Figure 3.5: LESCO specific heat.

Differential specific heat of LESCO with $x = 0.125$ [181]. Both the structural transition at T_{LTT} and the charge nematic transition at T_{CN} are clearly seen. The inset shows a comparison with the sample with doping $x = 0.15$.

$T_{LTT} \sim 130$ K in the measurements on the sample with $x = 0.125$ (Fig. 3.5). Clearly the transition at T_{CN} involves a much smaller change of the internal energy than the LTO-LTT structural transition, consistent with an electronic ordering. The peak at the structural transition can serve as an internal calibration, enabling us to obtain absolute values of the specific heat difference upon comparing with previous experiment on LESCO powder samples [191].

The combination of NQR and NMR wipeout and specific heat measurements gives a strong indication that a novel electronic phase appears at a temperature T_{CN} which is different from both the structural transition temperature T_{LTT} and the x-ray charge stripe appearance temperature T_{CO}. To show that this phase is in fact the theoretically predicted charge nematic, we employ a third experimental technique – nonlinear conductivity. As discussed in Chapter 2, third order nonlinear response is sensitive to fluctuations of the charge nematic order parameter [106] $Q = \left(S_{\mathbf{k}} - S_{\mathcal{R}(\mathbf{k})}\right) / \left(S_{\mathbf{k}} + S_{\mathcal{R}(\mathbf{k})}\right)$, where S is the static electronic structure factor, and $\mathcal{R}$ denotes a rotation by $\pi/2$. The fluctuations are expected to diverge at a nematic transition, while the order parameter itself measures orientational symmetry breaking and becomes finite below the transition temperature. Nonlinear conductivity only measures the fluctuations (and not the symmetry breaking

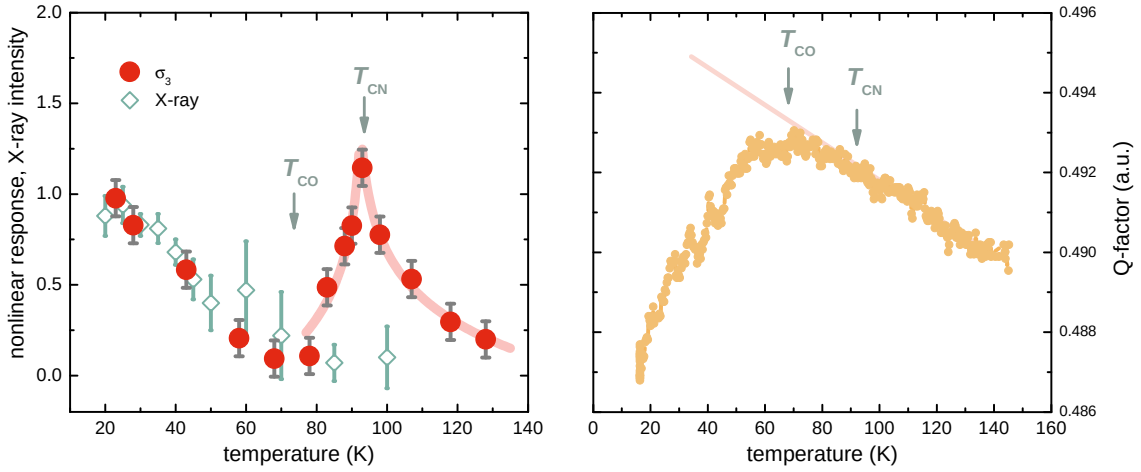

Figure 3.6: Linear and nonlinear conductivity of LESCO.
Third-order nonlinear conductivity of LESCO with $x = 0.125$ [181], compared the charge stripe signal intensity obtained in an x-ray scattering study [29] (left). The nonlinear response shows a strong peak at T_{CN}. In comparison, a contact-free measurement of the linear conductivity of LESCO with $x = 0.11$ (right) is mainly featureless, apart from a smooth deviation from the high-temperature behaviour appearing close to T_{CN}. For simplicity, we show the raw measurement of the Q-factor of the resonant circuit containing the sample, without calculating the linear conductivity.

directly). Measurements of third harmonic signal in LESCO with $x = 0.125$ in dependence on temperature display such a divergence at the temperature T_{CN} (Fig. 3.6). These results can be compared directly to resonant x-ray measurements of the charge stripe order parameter [28], which clearly appears at temperatures below T_{CN}. Since the charge nematic does not break translational symmetry, scattering techniques such as resonant x-ray should not detect it, as is indeed the case. At temperatures below T_{CO}, the nonlinear response follows the charge stripe amplitude, because of nonlinear stripe dynamic effects – this will be discussed in the next section. The linear conductivity was also measured in the temperature range where stripes and nematic order occur, showing no discernible sharp features at either T_{CO} or T_{CN} (Fig. 3.6); instead, a continuous deviation from the high-temperature behaviour starts close to T_{CN}, similar to previous investigations [36,83]. Thus the order appearing at T_{CN} must involve higher-order charge correlations, consistent with a nematic phase.

Taken together, wipeout, specific heat and nonlinear response measurements (Fig. 3.7)

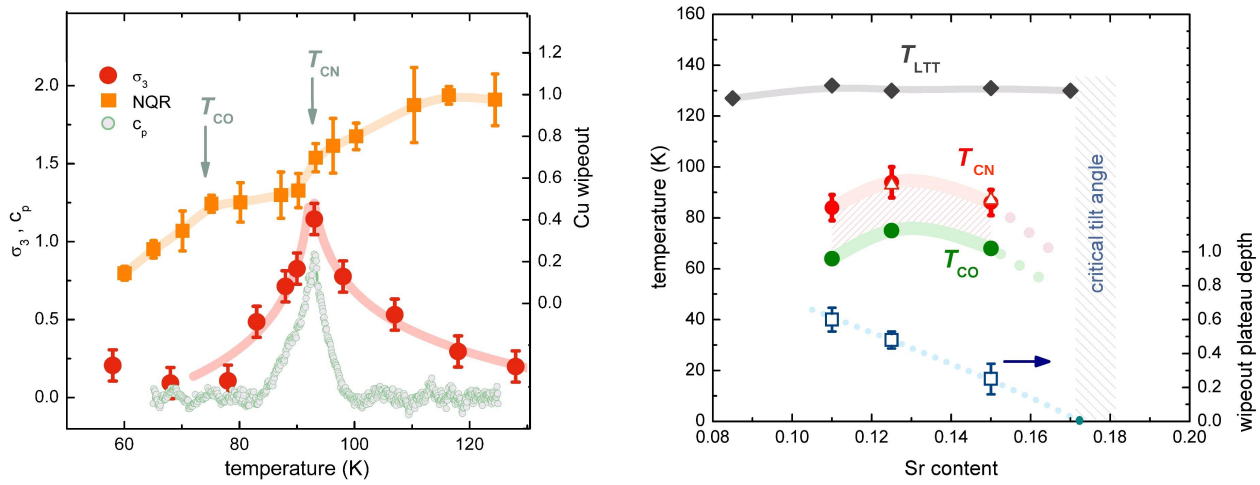

Figure 3.7: The charge nematic phase in LESCO.
Three experimental probes detect a charge nematic transition [181] in LESCO-1/8 (left): copper NQR wipeout (squares), nonlinear conductivity (full circles) and specific heat (empty circles). The nematic phase follows the charge stripes throughout the phase diagram with a characteristic dome shape (right), seemingly disappearing close to the doping concentration where the LTT phase becomes unstable (critical LTT tilt). Values for T_{CN} are from NQR wipeout (full circles) and specific heat (empty triangles). The LTT transition temperatures are from Ref. [191].

provide strong evidence for the existence of a charge nematic in LESCO, enabling us to construct a qualitative scenario for the appearance of charge stripes in agreement with theoretical predictions [40, 105, 186, 187] (Fig. 3.8). Starting from the high-temperature Fermi liquid, a thermodynamically well-defined charge nematic phase transition occurs upon cooling at T_{CN}, showing that the nematic is indeed insensitive to the electrostatic disorder present in LESCO. Charge stripes develop gradually from the nematic phase without a clear phase transition; the stripes are never coherent over long spatial distances, and their formation can be envisaged as a decrease in the number of stripe defects with cooling. This is in line with the predicted sensitivity of stripes to disorder, and previous observations of small stripe correlation lengths and glassy dynamics. The charge nematic transition closely follows the charge stripe appearance in dependence on doping, as seen in the updated LESCO phase diagram in Fig. 3.7. Importantly, T_{CN} is always relatively close to T_{CO} and significantly below T_{LTT}. This shows clearly that the charge nematic

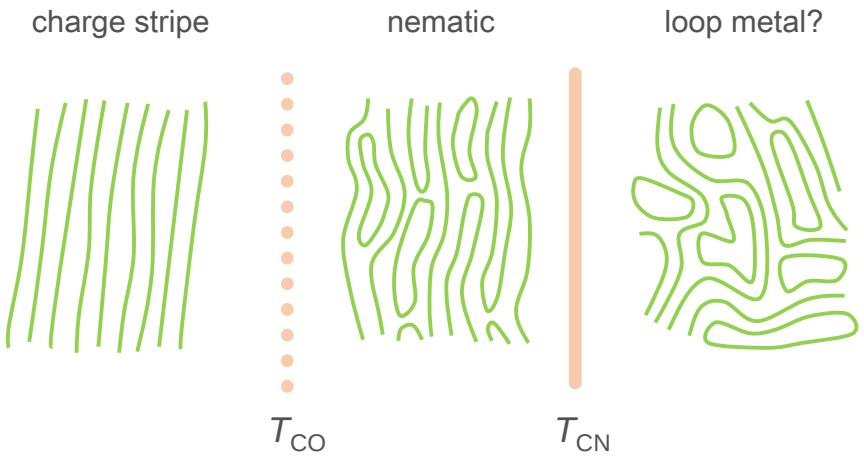

Figure 3.8: The evolution of charge stripes.
Schematic depiction of charge stripe formation in the presence of disorder, as seen in our experiments [181]. The nematic phase remains well defined and appears through a phase transition at T_{CN}, while the stripes form gradually upon cooling. A possible exotic high-temperature phase – the loop metal – is also shown.

cannot be identified with the pseudogap phase, since the pseudogap opening temperatures are significantly higher in the underdoped region of lanthanum-based cuprates. This does not imply that the pseudogap is not present together (and possibly in competition) with the nematic phase, but rather that the nematic forms within the pseudogap regime in the phase diagram. Our work thus confirms the theoretical scenario of charge stripe formation involving a precursor nematic phase [40, 105, 186], but disproves speculation relating the pseudogap to the charge nematic [40]. However, orientational symmetry breaking tendencies have been observed within the pseudogap in other cuprates such as YBCO and BSCCO [69, 70]: this could be a consequence of their more complex structure (e.g. YBCO contains oxygen chains that create a preferred direction in the CuO_2 planes), or may be due to the interaction between pseudogap hidden order and the nematic/charge stripe fluctuations. It is worth noting that charge stripe onset temperatures in YBCO are some 50 K higher than in lanthanum-based cuprates, making it difficult to separate pseudogap from charge stripe effects.

As discussed above, some quantum theories of charge stripe melting predict the existence of more exotic phases than the charge nematic, such as the loop metal phase which does not break any spatial symmetry [186, 187]. The difference between a loop

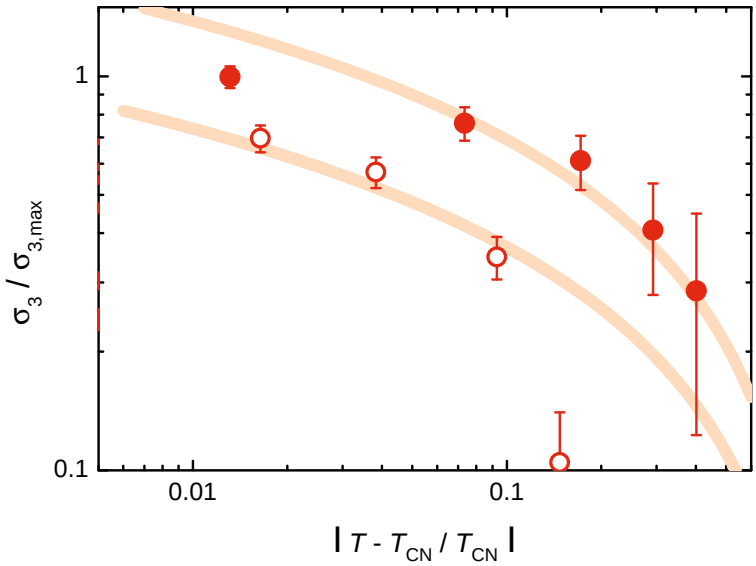

Figure 3.9: Critical behaviour of the nematic susceptibility. The nematic susceptibility $\sigma_3 (k_B T)^3$ in dependence on relative temperature $\varepsilon = |1 - T/T_{CN}|$, below T_{CN} (empty circles) and above T_{CN} (full circles). The log-log plot shows that a simple power-law description is not valid in the nematic critical region. The data are consistent with a logarithmic dependence (lines), but due to the limited sensitivity and number of points, a quantitative analysis of the critical behaviour is difficult.

metal and conventional Fermi liquid is that the loop phase only contains closed charge modulation loops, while a Fermi liquid can be envisioned as a liquid of both open and closed loops. The nematic, in turn, may be viewed as a loop metal wit a preferred direction for the elongation of the loops. Direct detection of a loop metal is even more difficult than the charge nematic, but our results hint at its possible presence above T_{CN}. Namely, if one calculates the nematic susceptibility as $|\sigma_3| (k_B T)^3$ from the generalized fluctuation-dissipation theorem, it is seen that the susceptibility decays rather slowly at high temperatures, indicating that strong nematic fluctuations are present up to T_{LTT}. This is also in agreement with recent x-ray nematicity measurements in LESCO [193].

Quantitatively, one may try to extract a critical exponent from the nematic susceptibility by plotting it on a log-log scale with relative temperature $\varepsilon = (T - T_{CN}) / T_{CN}$. Interestingly, power-law behaviour is not observed in the measured temperature range – the results are, however, consistent with a logarithmic dependence (Fig. 3.9). The small number of data points precludes any strong conclusions about the fluctuation regime, and the deviation from power-law critical behaviour might also be caused by corrections

to scaling [109]. Either way, clearly a simple mean-field description is inadequate for the charge nematic transition. A loop metal phase should possess strong nematic fluctuations, which then imply that renormalization effects are important and mean-field theory does not apply [186, 187]. The large nematic susceptibility and unconventional critical regime are therefore consistent with the existence of a loop metal phase. Yet further experiments are necessary to make a definite identification. Due to the absence of structural transitions, other materials such as mercury-based cuprates [33, 194] might be more convenient for investigating such exotic charge ordered phases.

The finding of a charge nematic phase in LESCO creates a connection between cuprates and other novel materials: the presence of electron nematic order in pnictide superconductors [112, 114, 195, 196] and quantum Hall systems [197] is relatively well established. In these cases, nematic ordering is manifested through macroscopic anisotropies of response functions; in contrast, nematic order in nominally tetragonal layered compounds such as LESCO might be self-masking [54]. Namely, the nematic direction can rotate from plane to plane due to interplane coupling (similar to the charge stripe orientation [37]), resulting in a vanishing macroscopic in-plane anisotropy. Thus the orientational symmetry breaking cannot be measured by macroscopic (linear) transport. Yet as we demonstrate here, the field-induced fluctuations measured by nonlinear conductivity are still be present and detectable, since their direction only depends on the direction of the *applied* electric field. Thus σ_3 is a good probe of nematic fluctuations in self-masked nematics as well, where linear response cannot detect the nematic transition.

3.2 Charge and spin stripe dynamics.

Having established that charge stripes appear through a precursor nematic phase, we now turn to an investigation of the stripe dynamics and related electronic spin fluctuations. Several theoretical arguments are relevant for this discussion. Firstly, in a disordered system the charge stripes are expected to be pinned to impurities and thus relatively static. Charge density wave pinning has been investigated in several materials [159, 162–164, 198–201] and both quantum and quasi-classical models of the process have been developed [159, 202]. The situation in cuprates is more complex than in one-dimensional CDW systems because the stripes are two-dimensional and can deform in many ways to minimize their energy in the presence of point defects [198, 203]. A quantitative theory

of two-dimensional stripe pinning is therefore more difficult to develop and is to our knowledge still an open prospect, but we assume that the qualitative features are similar to one-dimensional CDW.

In the simplest model of stripe pinning, the stripes reside in a periodic pinning potential [159]. An electric field higher than a critical value is needed for the stripes to move between minima of the pinning potential. If a field higher than this unpinning field is applied, the stripes can significantly contribute to charge transport, causing a nonlinear response. Well-known one-dimensional CDW systems [163, 164] are insulators at low electric fields, because the stripe pinning almost completely blocks long-distance charge transfer; application of high electric fields then induces a strong conductivity increase and significant nonlinearity. In cuprates, the unpinning effects are much less dramatic, since the stripes are metallic and but small modulations of the charge density, so linear charge transport is possible even with pinned stripes. Therefore conductivity nonlinearity due to stripe dynamics is expected to be small and superimposed on a large linear conductivity, which makes our nonlinear response measurement setup uniquely suited for studying such effects. On the other hand, the local dynamics of stripe pinning can be investigated using NQR, since the charge modulation changes the local electric fields seen by the nuclei and modifies the NQR spectra (if the stripes are static on NQR timescales), or influences the NQR spin-lattice relaxation (if the stripes fluctuate). Combining NQR and nonlinear conductivity will thus give us a complete picture of charge stripe dynamics in lanthanum-based cuprates.

The second important effect related to charge stripes in cuprates is the appearance of a related spin stripe order, and strong spin fluctuations [37,60,66,67,111,184,192]. In the roughest approximation, the spins order because of the proximity of an antiferromagnetic ground state, making it energetically favourable to couple regions of smaller charge density to increased AFM correlations. Such a view effectively states that the spin degrees of freedom are secondary for the charge stripe formation; comparing different materials will give some credence to this. An increase of spin fluctuations has been predicted in cuprate charge nematics as well [188], providing a link between the nematic order and NMR/NQR signal wipeout. Using these local probes, we will show that the spin stripes have different dynamic properties than the underlying charge order, and that their strength strongly varies between cuprate families.

We use two cuprate compounds for the investigation of stripe dynamics. The europium

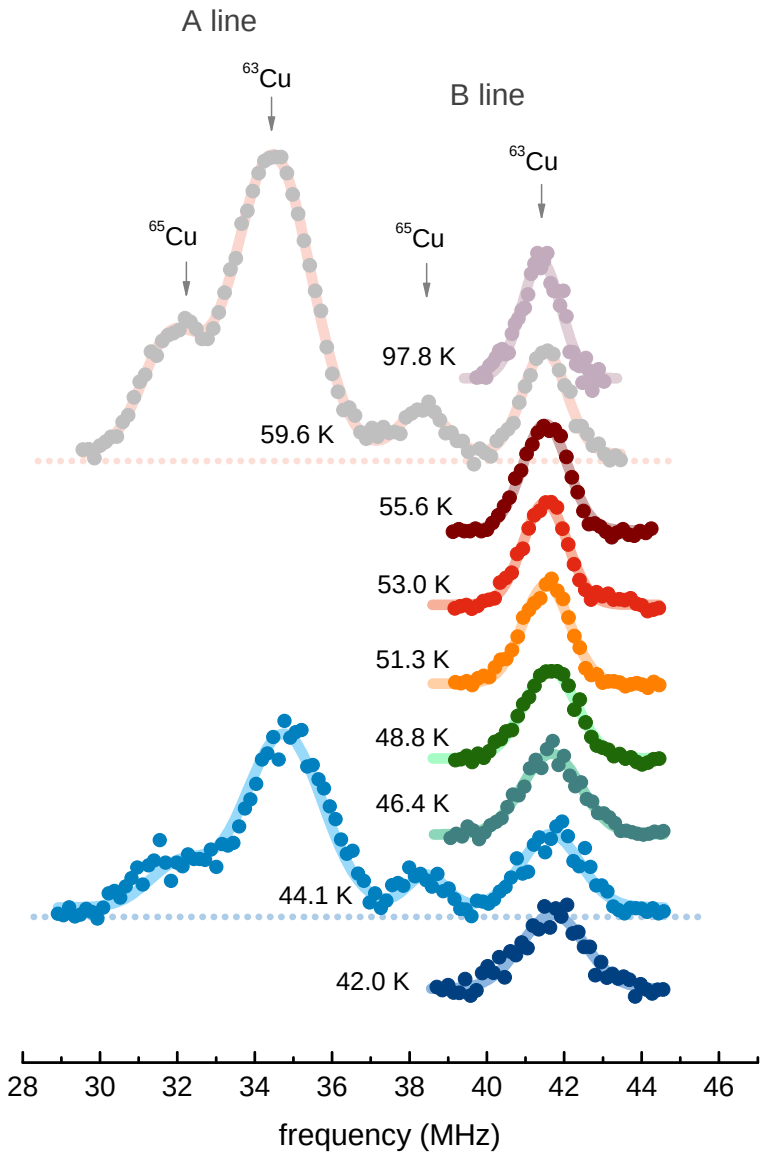

Figure 3.10: The copper NQR spectrum of LBCO-1/8.

The spectra [189] were obtained by integrating the Fourier-transformed spin echo signals with an echo time of 2.3 μs. Four distinct spectral lines are present: two sites (A and B) for two isotopes (^{63}Cu and ^{65}Cu). Lines are Gaussian fits, and T_{CO} denotes the temperature where charge stripe order is first observed in scattering studies [37]. A strong broadening of the B line is observed below T_{CO}, a consequence of incommensurate static charge stripes.

co-doped LESCO is a good model system for the same reasons as mentioned in the discussion of charge nematic order: it possesses charge stripe order in a wide temperature range, without interference from structural effects or superconductivity. In addition, we use one of the most investigated charge stripe cuprates, LBCO-1/8. There the LTT-LTO transition, charge stripes, spin stripes, and unconventional superconductivity all appear within 20 K [37,85,86]. We employ LESCO mainly for nonlinear conductivity experiments due to the clear separation between transition temperatures, while LBCO is better suited for Cu NQR investigations because of a fortunate arrangement of spectral lines. The Cu NQR spectrum of a LBCO-1/8 single crystal is shown in Fig. 3.10, at several temperatures above and below T_{LTT} and T_{CO}. High-temperature spectra are the same as in previous work [65,204]. All spectra were obtained with the fast spin echo methodology described in Chapter 2, enabling measurements at temperatures significantly below T_{CO} where signal wipeout makes conventional spin echo experiments impossible.

Four lines are visible in the NQR spectra: two sets of two lines (from two isotopes ^{65}Cu and ^{63}Cu). Each isotope has two distinct lines, implying two different local environments for the copper atoms. Investigations in related strontium-doped cuprates [95, 205] have shown conclusively that the two lines originate from Cu atoms close to the Ba (or Sr) dopands – the higher-frequency B line – and Cu atoms further away from the dopands – the broad, low frequency A line. The positions (and widths) depend significantly on doping [95]. LBCO is particularly favourable for NQR work due to the large separation between the lines, enabling clear observations of the influence of charge order on the spectra. The effects of incommensurable charge stripe order are indeed observed below T_{CO} as an increase in the width of the lines. A simple Gaussian fit to the B line of ^{63}Cu makes quantitative analysis of the width possible, and its temperature dependence is shown in Fig. 3.11. Since NQR frequencies are proportional to the local charge, the NQR linewidth is a direct measure of the amplitude of the charge modulation. A comparison to the stripe order parameter (which is equivalent to the amplitude) obtained from a hard X-ray scattering study of Tranquada et al. [86] confirms this; the measurements follow each other closely below T_{CO}.

Importantly, the NQR linewidth is a microscopic measure of the stripe amplitude, and its value can be directly compared to experiments in other cuprates. If one assumes that the linewidth corresponds to the X-ray order parameter down to $T = 0$, a ground-state value of the modulation amplitude can be inferred. Taking ν_Q to be the mean

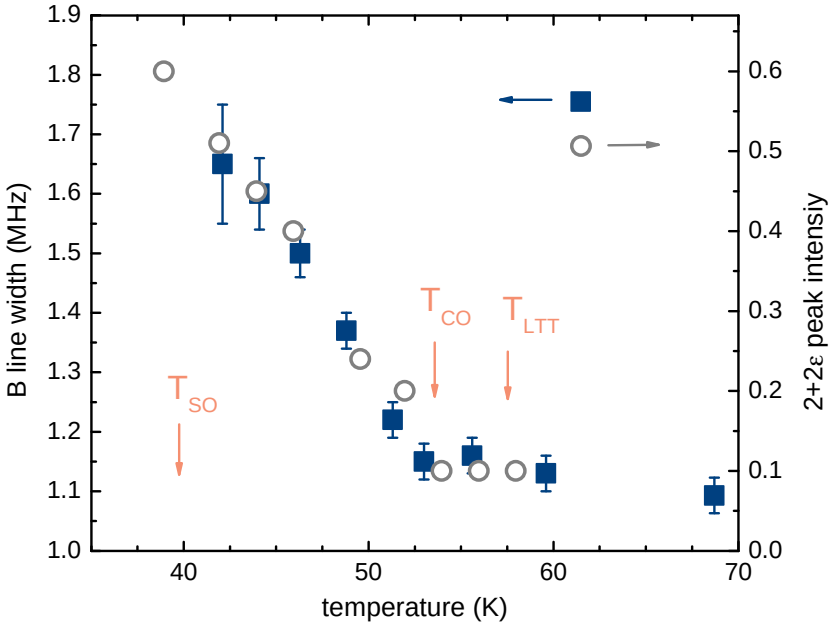

Figure 3.11: Charge stripe order parameter in LBCO.
Widths of the ^{63}Cu B line (see Fig. 3.10) in dependence on temperature [189], compared to the charge stripe amplitude measured with hard x-ray scattering by Tranquada et al. [86]. The NQR linewidth follows the X-ray measurements closely, and is thus a good microscopic measure of the charge stripe amplitude. Below $\sim T_{SO}$ the spin-lattice relaxation is too fast for NQR measurements.

NQR frequency of the B line in LBCO-1/8, the extrapolated relative amplitude becomes $\Delta\nu_Q/\nu_Q \approx 0.02$. A similar amplitude is seen in other cuprate compounds: oxygen NQR satellite linewidths in YBCO [57] and LESCO [47] at doping 1/8 have the same values. The copper NQR satellites in YBCO with doping 0.105, which show evidence of a commensurate charge density wave, display a line splitting similar to the extrapolated width in LBCO as well [26]. We may thus conclude that the amplitude of charge stripe modulation in different cuprate families is universal; this is in agreement with conclusions from recent resonant X-ray scattering work [48], but the precision of our local probe investigation is significantly higher.

The linewidth change also provides an absolute measure of the charge modulation amplitude, which can be estimated by knowing that ν_Q is proportional to the number of doped holes per unit cell with 20 MHz per hole [123]. A significant intrinsic charge inhomogeneity exists in lanthanum-based cuprates at all temperatures [95], determining the high-temperature linewidth of $\sim$ 1.1 MHz in LBCO-1/8 (Fig. 3.10). Charge stripes

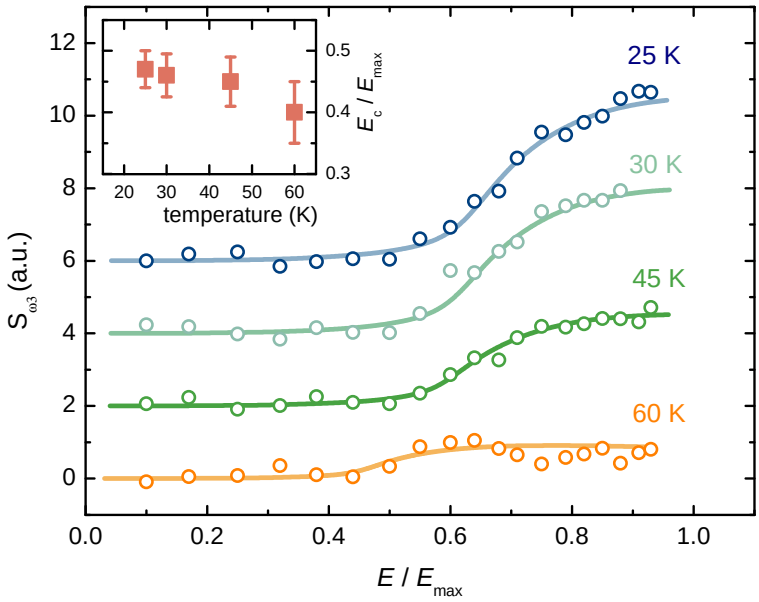

Figure 3.12: Electric field dependence of the LESCO nonlinear conductivity. Third harmonic response of LESCO-1/8 in dependence on the applied electric field (normalized to the maximum attainable field E_0). Lines are fits to a simple one-dimensional washboard stripe pinning model, and the inset shows the temperature dependence of the characteristic depinning field E_c.

add another ~ 1.5 MHz to the linewidth at $T = 0$, implying a stripe amplitude of ~ 0.04 holes. This value is considerable, but still far from the average doping concentration. To understand the value universal amplitude, a microscopic theory of stripe formation is necessary, but our work shows that the formation is likely not material-sensitive. Furthermore, the NQR line broadening indicates that the charge stripes are static on the NQR time scale, since stripes fluctuating on timescales shorter than $1/\nu_Q$ not influence the static linehsapes, but only the spin-lattice relaxation times. A more detailed analysis of the nuclear relaxation in LBCO will indeed show that the relaxation mechanism is purely magnetic, as discussed below. Thus the charge stripes are effectively pinned to lattice defects, and nonlinear conductivity due to stripe depinning is to be expected.

As discussed in the previous section, in LESCO a significant nonlinear response is observed in relation to the charge nematic transition at T_{CN}, but a steadily increasing contribution is also seen at lower temperatures. The low-temperature signal closely follows the X-ray scattering intensity, which is proportional to the amplitude of the charge stripes (Fig. 3.6). We argue here that the low-temperature nonlinear response is consistent with stripe depinning dynamics. Measurements of the nonlinear response dependence on the

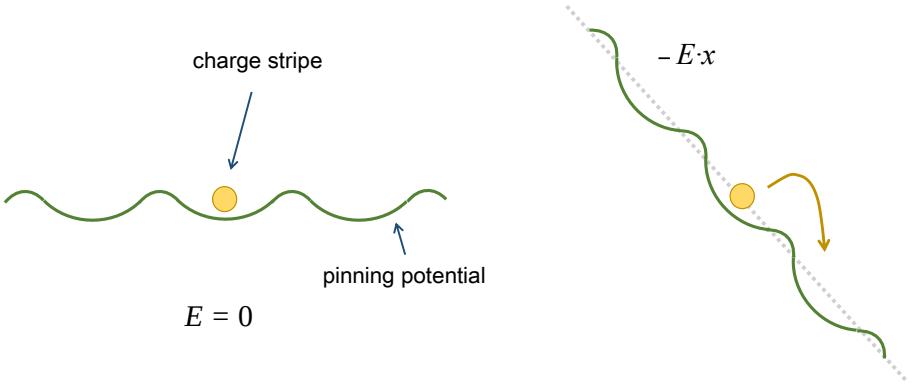

Figure 3.13: The classical washboard model of charge stripe pinning. The charge stripes are imagined as a point with mass m and charge q_{eff}, moving in a periodic pinning potential (line). Without applied electric field, the stripes are pinned in a potential well (left). Application of a large external field tilts the potential and enables stripe unpinning (right).

external field at several temperatures below T_{CO} were performed (Fig. 3.12), in order to compare them with simple models of stripe pinning dynamics. A distinct shape of the field dependence is observed, bearing a likeness to the current-voltage characteristic of well-known charge density wave materials [159]. A naive washboard pinning model may be used to analyse the measurements, assuming simply that the stripes have some effective mass m_{eff} and charge q_{eff} and that they move in a one-dimensional periodic potential [159] (Fig. 3.13). The use of a basic one-dimensional model is somewhat justified because it is known from scattering studies that stripes are predominantly pinned by orthorhombic twin boundaries present in the LTT phase [61, 62]. Since the boundaries are extended (linear) crystalline imperfections, point defects are to one-dimensional CDW what line defects are to two-dimensional stripes. The classical one-dimensional stripe equation of motion is

$$m_{eff}\ddot{\xi} + \Gamma\dot{\xi} + \frac{\partial V}{\partial x} = q_{eff}E(t) \tag{3.1}$$

where ξ is the position (or phase) of the effective stripe, Γ a damping coefficient, V the pinning potential and E the external electric field. Notably, the washboard model assumes that the stripes are rigid in the sense that their dynamics can be described through the single phase parameter ξ (without appreciable amplitude changes) – this is a radical approximation, and thus the entire analysis should be taken semiquantitatively.

Taking the pinning potential to be a simple sinusoidal function, the equation of motion becomes tractable [159]. We note that similar dynamic models are used e.g. for vortex pinning in superconductors [206], and hopping conduction in semiconductors [207]. No thermal excitation contribution is present, since both NQR and X-ray scattering experiments show that the stripes are static on long timescales, implying that the barriers between the minima of the pinning potential are significantly higher than $k_B T$. For simplicity, we assume that the damping term dominates the inertial term, which leads to conventional exponential relaxation of the stripe system in response to a small pulsed external field. The inertial term gives rise to a collective mode, which is shifted to a finite frequency in the presence of pinning [159]. Without the inertial term, the case of a constant electric field is easily solved: no stripe motion occurs unless the field is higher than the critical value $E_c = 1/q_{eff} \left|\partial V/\partial x\right|_{L_{pin}}$, where L_{pin} is the characteristic pinning length, corresponding to the spatial period of the pinning potential. A complementary analysis of small stripe oscillations in the pinning potential can be performed by retaining only the linear term in the derivative $\partial V/\partial x$, which for a sinusoidal pinning potential yields a characteristic collective stripe motion frequency [159]

$$\omega_0^2 = \frac{1}{m_{eff}} \left|\frac{\partial V}{\partial x}\right| = \frac{2\pi}{L_{pin}} \frac{q_{eff}}{m_{eff}} E_c \tag{3.2}$$

This relation between the frequency ω_0 and pinning field E_c provides a way to estimate one quantity if the other is known, and will be used below. For electric fields higher than E_c, the stripes can cross the pinning barrier and obtain a velocity which has both a constant and a periodic part. Yet our experimental situation requires solving eq. (D.1) for an oscillating external field, which cannot be done in closed form. A numerical solution is necessary, and the third harmonic response is obtained by a Fourier expansion of $\xi(t)$ for different values of the electric field amplitude (see Appendix D). Experimental data can be fitted to the resulting curves in a satisfactory manner (lines in Fig. 3.12), validating our simple effective approach to stripe pinning dynamics.

Stripe-related nonlinear conductivity was investigated in cuprates and similar systems before, with mixed results – it was always difficult to separate the intrinsic response from heating contributions [161,198–200]. Since our nonlinear measurement method eliminates heating, it makes the detection of stripe pinning signals possible. However, a downside is that we cannot know the absolute values of the induced electric fields, and can thus only compare the relative critical fields for different temperatures. The maximum electric field induced in the excitation coil of our setup may be roughly estimated from the Maxwell

equations, as $E_0 \sim B_0 \omega L$, where $B_0 \sim 100$ Gauss is the typical magnetic field amplitude, $\omega \sim 2\pi \cdot 20$ MHz the oscillation frequency, and $L \sim 2$ mm the linear dimension of the sample. The electric field is then ~ 20 V/cm, implying that the pinning fields are of the order of 10 V/cm. This is two to three orders of magnitude higher than in conventional CDW systems [159, 163, 164], but somewhat lower than the values measured in quasi-two-dimensional materials such as nickelates [198]. Importantly, the quasi-one-dimensional pinning model in cuprates is plausible because line defects (twin boundaries) cause the pinning. For the case of point defect pinning of two-dimensional stripes, their dynamics might be qualitatively different because of the possibility of curving around the pinning centers. The theory of such pinning is to our knowledge not developed, but might be relevant to other materials. Another salient point is the assumption that the stripes in lanthanum-based cuprates are uniaxial in the CuO_2 planes, and not of the chequerboard type. Strong evidence for uniaxial stripes exists from scattering experiments on LBCO [37] and LESCO [28]. Presumably the pinning dynamics of chequerboard order is also qualitatively different, which might be important for other cuprates such as BSCO.

To estimate the collective mode frequency, we must make assumptions about the pinning length and effective mass and charge of the pinned stripe in eq. (3.2). To obtain an upper limit on the frequency, we may take $q_{eff} = e$ and $m_{eff} = m$, where e and m are the charge and mass of the electron, respectively. The pinning length should be comparable to the stripe coherence length, $L_{pin} \sim 10$ nm. This gives $\omega_0 \sim 10^{11}$ Hz, in the far infrared frequency range. Note that the frequency only depends on the ratio of effective mass and charge, so taking a lower charge (e.g. the stripe amplitude of 0.04 holes per unit cell calculated above) should imply also taking a smaller mass, leaving the frequency roughly the same. Finding the collective mode would be independent evidence of the stripe pinning model in LESCO and other cuprates; yet the infrared spectra of cuprates are rather complicated, and a large low-frequency Drude contribution [91] might obscure the collective mode (especially in the case of strong damping).

Stripe-related nonlinearities in cuprates around doping 1/8 have to our knowledge not been demonstrated before, and the pinning field values appear to be reasonable in view of the enhanced stability of two-dimensional stripes. Yet the possibility remains that the nonlinear conductivity we observe in LESCO below T_{CO} has a different origin: some components of the nonlinear response tensor are sensitive to orientational symmetry breaking, in particular $\sigma_{3,xxxy}$ [174] (the indices denote the directions of the electric field and current

components). The signal might then simply be a measure of the nematic order parameter, since in our experimental configuration the magnetic field induces electric fields in both x and y directions. This would also explain the apparently weak dependence of the pinning field on temperature, shown in the inset of Fig. 3.12 (although similar dependences also appear in some CDW systems [159]). To distinguish between the alternative origins of the nonlinear signal, a phase-sensitive measurement would be required, and detection of the collective mode would be highly desirable. Other tell-tale signs of stripe collective motion, such as narrow band noise and conductivity relaxation after a temperature quench should also be observable in principle [159], but could again be obscured due to the relatively large conductivity of cuprates. In any case, the depinning fields are at least 10 V/cm, and possibly much higher if the nonlinear conductivity is proportional to the nematic order parameter.

We have seen that a relatively large electric field is needed to unpin the charge stripes in LESCO, and the Cu NQR spectra in LBCO are consistent with static stripes as well. Yet significant spin dynamic effects are known to occur in relation to charge stripes: lanthanum NQR and NMR studies consistently detect strong and slow spin fluctuations [65,66,111,184], while neutron scattering measurements of the spin susceptibility see a spin gap opening [37,86]. To gain deeper insight into the spin dynamics, we measure the spin-spin and spin-lattice relaxation times in LBCO-1/8, using our fast spin echo methodology. The first important result is that fast spin-spin relaxation completely explains the previously observed signal wipeout in LBCO. We find that the Cu T_2 drops sharply below T_{CO}, to values around 3 μs. In a conventional NMR or NQR experiment, the echo times are larger than 10 μs – the signal below T_{CO} is completely unobservable in such conditions. Yet no appreciable signal decrease is observed if the spin-spin relaxation is extrapolated to zero echo times in our measurements above 40 K (Fig. 3.14), demonstrating that the entire wipeout effect is accounted for by the fast relaxation. Furthermore, the spin-spin relaxation curves change in shape. Above T_{CO} they are predominantly Gaussian, implying that there the decoherence is caused by indirect nuclear coupling through the electron gas; such a situation is frequently encountered in other cuprates at high temperatures. Below T_{CO}, the relaxation is pure exponential, meaning that the surrounding electrons cause nuclear spin flips [119, 120] and indicating large electronic local fields on the NQR timescale. A similar change from Gaussian to exponential relaxation appears in other cuprates such as YBCO [26], but in lanthanum-based cuprates the spin fluctuations

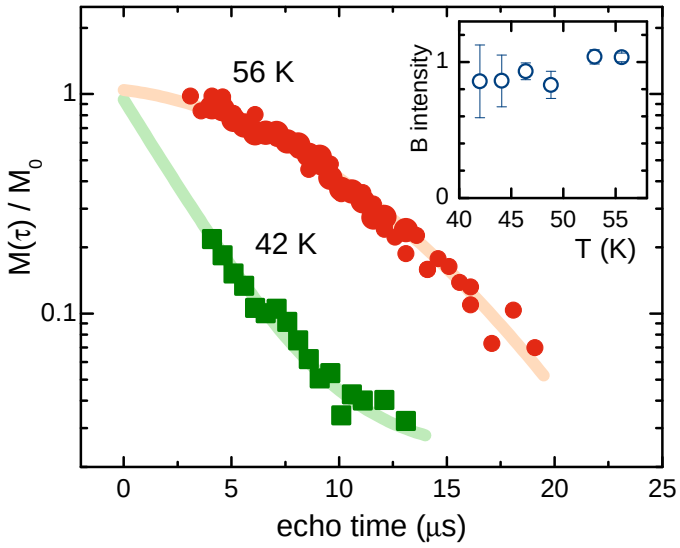

Figure 3.14: Copper spin-spin relaxation in LBCO-1/8.
Spin-spin relaxation curves [189] are shown for the Cu B line at two representative temperatures above and below the charge stripe onset temperature $T_{CO} \approx 53$ K. The relaxation is Gaussian at high temperatures and pure exponential in the charge-ordered phase, but the extrapolated intensities are roughly the same. Inset shows the dependence of extrapolated intensity on temperature, demonstrating the absence of signal wipeout.

associated with charge stripes are significantly stronger, leading to very fast spin-spin relaxation and apparent signal wipeout.

In previous work on Cu wipeout in powder samples, the wipeout fraction increases by decreasing the temperature in a relatively mild manner, superficially similar to the behaviour of the charge stripe order parameter [63–65]. Elaborate microscopic models of the stripes have been proposed and fitted to the data [65], and the crossover from Gaussian to exponential relaxation was explained through strong spatial inhomogeneity of nuclear relaxation rates [65,110]. A fraction of the nuclei was supposed to relax quickly and thus be invisible in the experiment, causing Redfield-like exponential spin-spin relaxation of the visible nuclei. Our work refutes these hypotheses: we see no significant stretching of either the spin-spin or the spin-lattice relaxation curves (to be discussed below), and all nuclei are accounted for below T_{CO}. Therefore the majority of nuclei relax in the same way, and the exponential spin-spin relaxation must have a different cause. Notably, the same Gaussian-exponential crossover is observed in charge-ordered YBCO [26], where the spin-spin relaxation is an order of magnitude slower than in LBCO and no wipeout is seen. A possible explanation of the exponential relaxation may come from slowly fluctuating

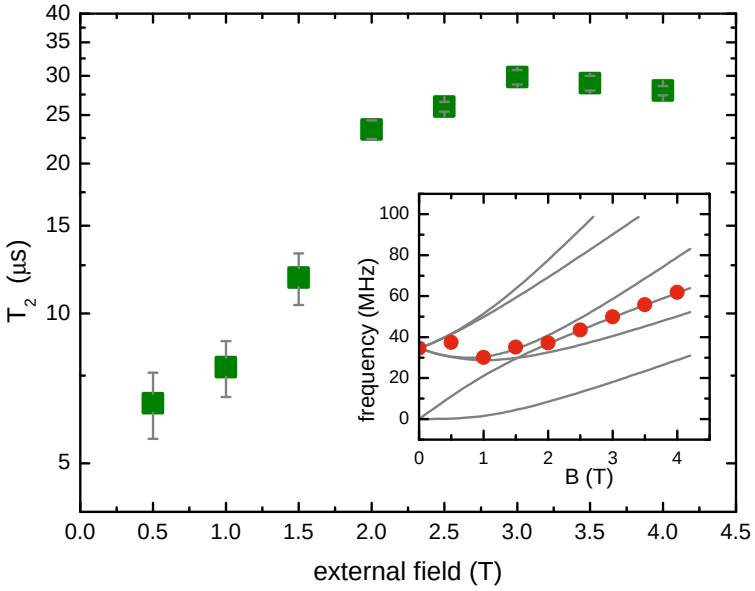

Figure 3.15: Cu spin-spin relaxation times in dependence on external magnetic field. The spin-spin relaxation rate of the Cu B line of LBCO-1/8 depends strongly on an in-plane applied magnetic field [189], with a critical field $B_c \sim 2$ T. An in-plane field suppresses the spin fluctuations induced by charge stripe order, thus increasing T_2. Inset shows all possible resonant frequencies obtained by numerical diagonalization of the full NMR Hamiltonian (lines), and the frequencies used in the measurement (points).

local fields within the CuO_2 planes caused by electronic spins, which induce nuclear spin-flips in the same way as an external in-plane field would. The large difference between crystals and powder samples then probably comes from surface pinning effects, although the powders may have a larger concentration of structural defects as well. A detailed investigation of this is beyond our work, but would be required to assess quantitatively the significant body of previous wipeout measurements.

Further insight into this point can be obtained by applying an actual static external magnetic field in the planes, which suppresses the in-plane spin fluctuations. To calculate the resonant frequencies, an exact diagonalization of the NMR Hamiltonian is necessary, as demonstrated in Chapter 2. We have measured the spin-spin relaxation at 45 K in dependence of the external field up to 4 T, with dramatic results (Fig. 3.15). The spin-spin relaxation time quickly increases with applied field up to a critical value $\sim$ 2.5 T, and then levels off – notably, the relaxation curves are always exponential. This suggests that already a small in-plane field suppresses the spin fluctuations that cause the fast relaxation, by introducing a defined magnetic direction in the CuO_2 planes.

The field sets a direction in the planes for the electronic spins, thus frustrating their possibility of free in-plane rotation and decreasing the spin fluctuations. Similar effects have been observed previously in lanthanum NMR in LBCO [111], and our measurements of partial wipeout in LESCO discussed in the previous section show a marked decrease of the wipeout fraction when external in-plane fields are applied. It is probable that the same spin fluctuation suppression mechanism is present in both materials. We note that the magnetic field dependence of the spin-spin relaxation makes the apparent wipeout fraction field-dependent as well, leading to possible discrepancies in previous work between NMR and NQR wipeout fractions.

Magnetic fields perpendicular to the planes were not applied, since it is known that their influence is small (at least for values up to $\sim$ 10 T) [111]. Much larger fields have been shown to induce charge stripes in cuprates such as YBCO, but such effects were not considered here.

While the spin-spin relaxation shows qualitatively that significant electronic spin fluctuations appear in LBCO below T_{CO}, a quantitative analysis is much easier for spin-lattice relaxation. We therefore measure the spin-lattice relaxation time T_1 on both A and B lines of ^{63}Cu in dependence on temperature. The decrease of T_1 is not as abrupt as the changes in spin-spin relaxation, and below $\sim$ 38 K the T_1 values fall below 10 μs, making further measurements unreliable and setting the lower temperature limit for our NQR investigations. To establish firmly the nature of the relaxation mechanism, we also measured the relaxation times for both copper isotopes at 45 K (Fig. 3.16) and both A and B lines. For a quadrupolar mechanism, the ratio of the relaxation times should be $^{63}T_1/^{65}T_1 = (^{65}Q/^{63}Q)^2 \approx 0.85$, while in case of a purely magnetic mechanism the ratio becomes $^{63}T_1/^{65}T_1 = (^{65}\gamma/^{63}\gamma)^2 \approx 1.15$ [117]. The experimental ratios are 1.04 ± 0.07 for the A lines, and 1.2 ± 0.1 for the B lines, with the result for the B lines being more reliable because of vanishing line overlap. The A signals are stronger (resulting in better signal-to-noise ratios and smaller relaxation curve fitting error), but the lines overlap significantly, which can artificially make the T_1 values closer than they are. Taking this into account, the values of the ratios are wholly consistent with a purely magnetic mechanism, further confirming the fact that charge stripes are strongly pinned in LBCO-1/8 as discussed above. We note also that the spin-lattice relaxation curves are almost perfectly exponential, showing that no significant distribution of T_1 is present. Fitting the curve for the A line with a stretched exponential $\sim \exp\left[-(t/T_1)^{\beta}\right]$ gives an exponent $\beta \approx 0.9$,

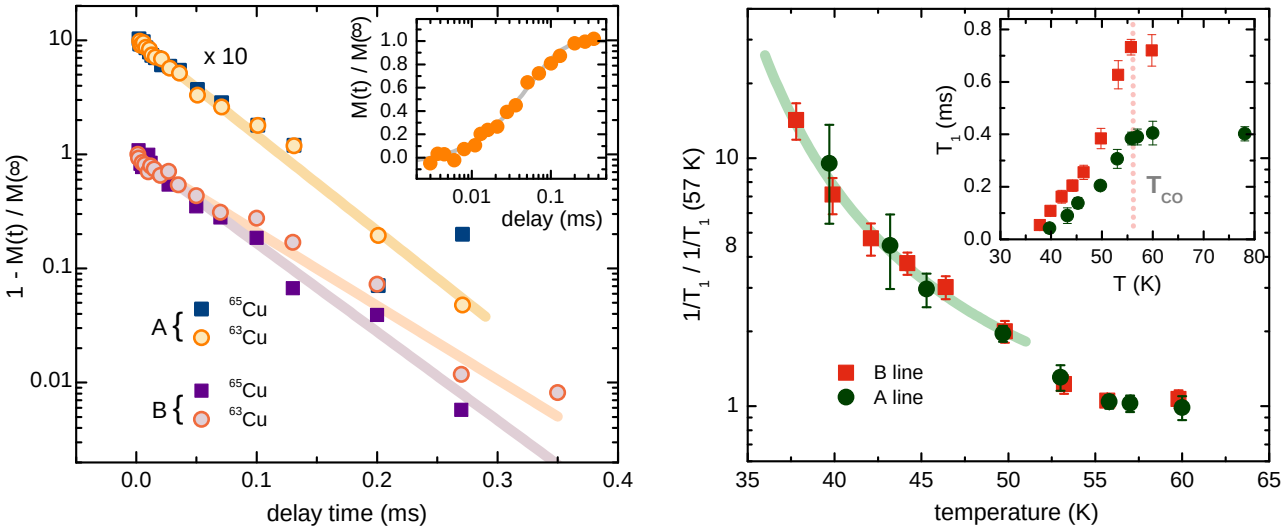

Figure 3.16: Cu spin-lattice relaxation in LBCO-1/8.
Spin-lattice relaxation curves at 45 K for the two sites and two isotopes (left), showing exponential decay and the differences between isotopes [189]. The inset is the raw magnetization recovery data in dependence on delay time for ^{63}Cu A line. The temperature dependence of the relaxation rates is shown in the right, normalized to the high-temperature values (main panel) and raw measured values (inset). Within the charge-ordered phase, spin fluctuations cause a glassy temperature dependence of $1/T_1$, consistent with a Vogel-Tamman-Fulcher law (line).

close to the pure exponential value of $\beta = 1$. Again, this is similar to results in YBCO, and invalidates the previously proposed models of inhomogeneous spin coupling for the exponential spin-spin relaxation.

The temperature-dependent T_1 measurements (Fig. 3.16) demonstrate two important points: the relaxation mechanism is the same for the A and B lines (up to a constant, temperature-independent factor), implying that the local spin and charge dynamics is not sensitive to the proximity of Ba dopands; and the temperature dependence of the relaxation rate is consistent with glassy spin freezing. As already discussed in relation to the pinning model, the first point is in agreement with scattering studies of charge stripes in lanthanum cuprates, which show that the stripes are predominantly pinned not by the Ba impurities, but by orthorhombic twin boundaries present in the LTT phase [61, 62]. To analyse the second point – glassy behaviour of spin fluctuations – we introduce a simple model for the low-frequency electronic susceptibility in line with neutron scattering and previous NMR investigations [50,65,86,92]. We take the imaginary

part of the susceptibility, which determines T_1, to have an asymptotic linear form at low frequencies: $\Im\chi(\omega) \sim \tau_c\omega$, where τ_c is a characteristic spin correlation time. Such a form is consistent with a simple Lorentzian frequency dependence of the susceptibility observed in neutron scattering experiments on LBCO and other cuprates [37,85,92,208]. It also leads to the low-frequency limit of a standard Bloembergen-Purcell-Pound (BPP) T_1 mechanism [210] used extensively in diverse solid and liquid systems [117], as well as cuprates with slow spin fluctuations [50, 111, 184]. According to the general theory of spin-lattice relaxation expounded in Chapter 2, in the limited temperature range below T_{CO} in LBCO-1/8 we may write $1/T_1 \sim \tau_c$. This seemingly counter-intuitive relation is true within BPP theory as long as the nuclear resonance frequency ω_0 is significantly smaller than τ_c: as the electronic correlation time decreases towards ω_0, its influence on the nuclear relaxation increases. Thus the spin-lattice relaxation rate is a direct measure of the spin correlation time, and it clearly diverges at some temperature below T_{CO} (Fig. 3.16).

To make a quantitative analysis, we use the well-known phenomenological model for motional correlation times in glassy liquids, known as the Vogel-Tammann-Fulcher (VTF) relation [169, 211, 212]:

$$\tau_c = \tau_0 e^{\Delta/(T-T_{VTF})} \tag{3.3}$$

where τ_0 is a microscopic correlation time, Δ plays the role of an energy gap, and T_{VTF} is the characteristic temperature where the dynamics freezes. Conventional Arrhenius activated dynamics would imply $T_{VTF} = 0$, as seen e.g. in ordinary liquids [212]. Glassy many-body correlations induce the strong dynamic slowing down at finite temperatures [169, 212]. The VTF relation fits our $1/T_1$ data well (Fig. 3.16), with $T_{VTF} \approx 20$ K and $\Delta \approx 80$ K. Although the experimental temperature range is rather limited, the obtained value of T_{VTF} coincides with the temperatures where spin freezing is observed in LBCO and LSCO using lanthanum NMR [50, 111], and it is also close to the temperature of the superconducting Berezinski-Kosterlitz-Thouless transition [85], as discussed in the next Section. Notably, inelastic neutron scattering experiments detect a spin ordering temperature $T_{SO} \sim 40$ K significantly higher than T_{VTF} and clearly not consistent with our T_1 data regardless of fitted models [37]. Yet the neutrons probe timescales which are about four orders of magnitude shorter than T_1, and in a glassy spin stripe scenario one would expect a significant frequency dependence of the apparent freezing temperature.

Our experiments show clearly that the spin fluctuations are dynamically decoupled

from the pinned charge stripes. Also, the universality of the charge stripe amplitudes is in stark contrast to the material-specific strength of the spin fluctuations. This suggests that the spin freezing is an induced effect, and not an integral part of charge stripe formation, as in Hubbard [55,56] and phase separation [45,105] models. Any model which does include spins as an important ingredient in charge stripes must then explain the large differences in material sensitivity between charge and spin stripe order. Although our work is more directly concerned with stripe thermodynamics and the influence of disorder than with their microscopic formation mechanism, the spin-charge stripe dynamical decoupling does provide constraints on the mechanism.

We have seen in this section that combined NQR, NMR and nonlinear conductivity measurements in LBCO and LESCO demonstrate that charge stripes are strongly pinned in these compounds, and that their amplitude is similar in several cuprate families. The induced spin stripes, however, fluctuate strongly and freeze in a glassy fashion. As we will find in the final section of this chapter, such complex spin and charge interplay bears a deep influence on the superconductivity developing on top of it.

3.3 Striped superconductivity.

The final question to be discussed in this thesis is the interaction between charge stripes and superconductivity, leading to dramatic CuO_2 plane decoupling in LBCO-1/8 [85,86]. Two important questions are to be answered: can the dynamics of the unconventional superconducting state in LBCO-1/8 be understood within established theories of two-dimensional superconductivity? and perhaps more importantly, what are the implications of such a state in charge-ordered compounds such as LBCO for cuprate superconductivity in general?

We first focus on a deeper understanding of the superconductivity in LBCO-1/8, through measurements of its conductivity in a wide frequency range. As discussed in Chapter 2, LBCO-1/8 displays an extremely rich phase diagram: the structural LTO-LTT transition occurs at $\sim$ 56 K, followed closely by the charge stripe onset at $\sim$ 53 K and spin stripe glassy dynamics with a freezing temperature $\sim$ 20 K [37,85,86], as seen in the previous section. In addition, a strong increase of in-plane conductivity is observed close to 40 K, and the conductivity increases further until diverging at $\sim$ 16 K [85]. The c-axis conductivity, however, remains finite down to $\sim$ 10 K, and a full superconducting Meissner

response only appears at ~ 4 K. Thus the ratio of in-plane to c-axis conductivity is essentially infinite in a considerable temperature range, indicating that true two-dimensional superconductivity is present in this compound. The results of the conductivity measurements were modelled in Ref. [85] with a conventional Berezinski-Kosterlitz-Thouless (BKT) expression [85,155], and a theoretical framework was devised to explain the decoupling of CuO_2 planes necessary for 2D superconductivity to occur [87–89]. The essential ingredient is the interplay between superconductivity and charge stripes, supposedly resulting in a spatially modulated superconducting state known as a phase density wave (PDW).

Superconductivity in a large majority of materials is spatially uniform, as is the BCS theory of superconductivity and most of its generalizations (such as Eliashberg theory) [118, 144]. Yet soon after the consolidation of BCS theory, a spatially modulated superconducting state was suggested close to interfaces between superconductors and ferromagnets, known as the Fulde-Ferrell-Larkin-Ovchinnikov (FFLO) state [213, 214]. There a strong external magnetic field causes the Fermi surface to split in two (for spin up and spin down electrons), and superconducting Cooper pairs form between electrons on different Fermi surfaces; the pairing therefore has a finite wave-vector. In LBCO, a similar phenomenon is proposed to occur: the superconducting phase becomes periodic with wave-vector $\mathbf{Q}_{SC}$, due to the interaction with underlying charge and spin stripe order [39, 87–89]. If the cuprates are regarded as stacks of two-dimensional superconductors with Josephson coupling between the layers, particular arrangements of the PDW phases across the layers can frustrate the interlayer coupling which would otherwise induce three-dimensional superconductivity. Broadly, such a frustrated coupling is proposed to explain the 2D superconducting physics observed in LBCO-1/8. Yet experiments probing the modulated superconductivity itself are rather difficult to perform, especially since the layer decoupling is not perfect and 3D superconductivity does appear eventually. In fact, the mean-field PDW model requires a finite interplane coupling for energy minimization [89]. Imaging the modulated superconductivity with surface sensitive probes in LBCO is impossible because of the strong ionic character of the bonding between CuO_2 and LaO layers, resulting in poor cleavability and large electric fields at the surface. However, recently an STM study has claimed the first direct detection of modulated superconductivity in a different, strongly anisotropic cuprate BSCCO [185], indicating that such a state is at least possible in principle. Signatures of the PDW state in other, less

direct probes such as ARPES are predicted to be relatively weak [215], and local probes such as NMR and muon rotation spectroscopy are confounded by the coexisting charge and spin stripes. It is thus fair to say that while the two-dimensional nature of superconductivity in LBCO-1/8 is relatively well established, the tentative underlying phase density wave is much more speculative. Alternative mechanisms of interlayer coupling frustration are thus possible.

To date the best evidence of BKT physics in LBCO comes from investigations of linear and nonlinear conductivity [85], where both the above-mentioned in-plane conductivity divergence and characteristic current-voltage power laws were observed. Here we measure the conductivity in dependence on frequency, to place much stronger constraints on the validity of BKT physics in LBCO and show that an ultra-slow timescale characterizes the superconducting dynamics.

The in-plane conductivity of LBCO-1/8 was measured using the contact-free methodology described in Chapter 2, with excitation frequencies ranging from 10 kHz to 10 GHz. A dramatic frequency dependence is observed below temperatures corresponding to the onset of two-dimensional superconducting fluctuations in previous work (Fig. 3.17). Almost no change is seen in the microwave conductivity, while the low-frequency results correspond closely to the nominally direct current (dc) conductivity from Ref. [85]. Measurements at intermediate frequencies show a smooth evolution, indicating the presence of a characteristic superconducting timescale in the millisecond range. In view of such a strong frequency dependence at low frequencies, it is important to note that the previously obtained conductivity is not truly dc, but measured using millisecond pulses (and thus effectively in the kHz frequency range). The temperature in our measurements is limited to above $\sim$ 15 K due to a relatively weak thermal contact between the sample holder and liquid helium (as described in Chapter 2), but the microwave measurements are performed in a different probe and thus extend to lower temperatures. No clear signs of superconductivity are seen at microwave frequencies down to at least 5 K.

Qualitatively, an extremely slow characteristic fluctuation timescale is consistent with vortex-antivortex dynamics of two-dimensional superconductors both above and below their BKT transition temperatures [156–158]. This is an important and nontrivial confirmation of BKT physics in LBCO-1/8. To make quantitative conclusions, we may compare the results to standard expressions for dynamic conductivity above T_{BKT}, where our measurements are reliable. We have shown in Chapter 2 that the dynamics of unbound

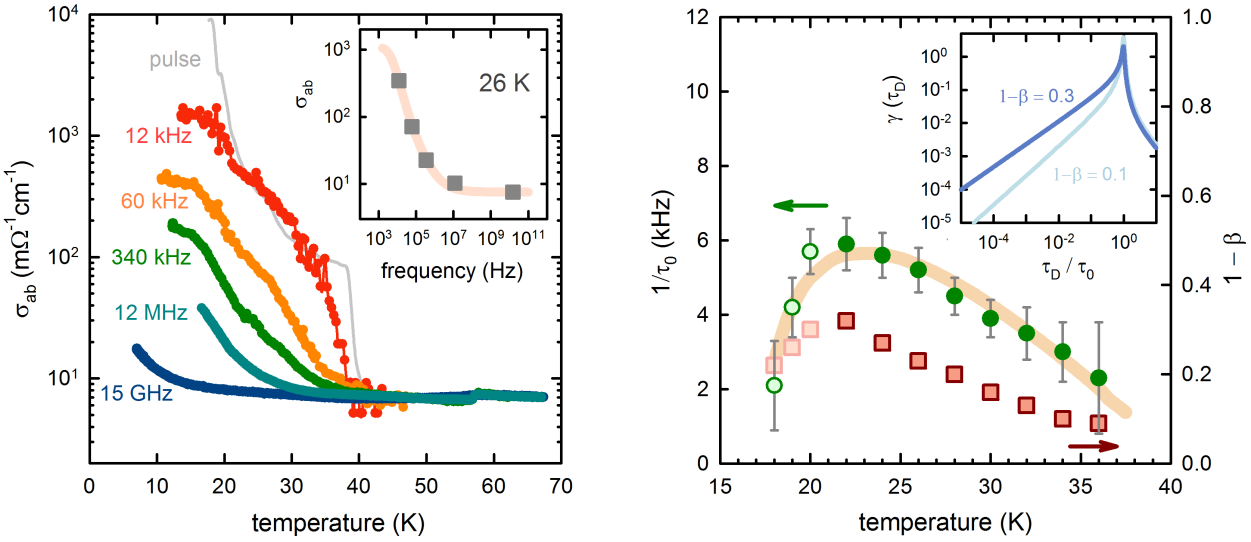

Figure 3.17: Frequency-dependent conductivity of LBCO-1/8.
AC conductivity of LBCO-1/8 in dependence on temperatures, at different frequencies of the applied electric field (left), showing a dramatic frequency dependence below ~ 38 K. Previous current pulse measurements from Ref. [85] are shown for comparison (line). The frequency dependence at 26 K is extracted in the inset, with a Davidson-Cole fit (see text). The temperature dependence of the characteristic relaxation time τ_0 obtained from the fits (right) follows a conventional Halperin-Nelson function (line – see text); the full circles were calculated only from our data, while the empty circles include the pulse measurements. The relaxation stretching parameter $1-\beta$ quantifies the influence of disorder on the superconducting dynamics and increases upon cooling, in broad agreement with lanthanum NMR studies. The inset shows the distributions of elementary relaxation times leading to the Davidson-Cole relaxation, for two values of $1-\beta$.

vortices high above T_{BKT} is essentially diffusional in a clean system, leading to simple exponential relaxation in the time domain and a Debye-Drude dependence of conductivity on frequency. Yet the measured dependence in Fig. 3.17 is stretched out over many orders of magnitude in frequency, especially at temperatures closer to T_{BKT}, and clearly cannot be fitted with a simple Drude form (2.10). The bound-vortex dynamical conductivity, i.e. the Minnhagen phenomenology (2.11) is also not appropriate, since its high-frequency behaviour is similar to a Drude form. To fit our data, we then take a phenomenological expanded Drude form used extensively in the analysis of glassy relaxation processes in

polymers and liquids, known as Havriliak-Negami dynamics [216]:

$$\sigma(\omega) = \sigma_\infty + \frac{\sigma_0}{\left[1 + (i\omega\tau_0)^\alpha\right]^\beta} \tag{3.4}$$

where τ_0 is the mean relaxation time, and α and β exponents describing the underlying spatial distribution of relaxation times. The Havriliak-Negami function in the frequency domain is closely related to stretched exponential relaxation in the time domain [217], and they both arise from a distribution of local characteristic times. To use a minimal number of free parameters in analysing the conductivity, we set $\alpha = 1$ and obtain a variant of the Havriliak-Negami relaxation called the Davidson-Cole form [218, 219]. The single stretching parameter β then provides information on the influence of disorder on the vortex dynamics. If the conductivity function is viewed as a superposition of elementary Drude processes with different τ_D, we can write it as

$$\sigma(\omega) = \int_0^\infty \frac{\gamma\left(\tau_D\right) d\tau_D}{1 + i\omega\tau_D} \tag{3.5}$$

with $\gamma\left(\tau_D\right)$ the distribution function, which is known in analytical form (see Appendix E). A plot of $\gamma\left(\tau_D\right)$ for different β (inset of Fig. 3.17 right) shows that the distribution is heavy-tailed at small relaxation times (i.e. high frequencies), as is indeed observed in experiment: the data can be satisfactorily fitted to the Davidson-Cole function at all measurement temperatures, enabling the extraction of both the characteristic time and β in dependence on temperature. A more physically realistic distribution of τ_D would probably provide a more accurate description of the measurements, but would forfeit the simplicity of the analytical Davidson-Cole expression.

In BKT theory, the relaxation time is proportional to the vortex density n_v, as discussed in Chapter 2. The temperature dependence of the density is modelled within the theory with a phenomenological relation known as the Halperin-Nelson equation [155],

$$n_v \sim 1/\xi_0(T)^2 e^{-\sqrt{b(T_{c0}-T_{BKT})(T-T_{BKT})}} \tag{3.6}$$

where b is a constant, T_{c0} the mean-field superconducting transition temperature, and ξ_0 is the Ginzburg-Landau superconducting correlation length with $1/\xi_0^2 \sim T_{c0} - T$ [144]. This formula describes the measured temperature dependence of τ_0 rather well in the entire range (noting that values from the previous voltage pulse study have been used in determining τ_0 below 20 K). The characteristic temperatures are $T_{BKT} = 16$ K and $T_{c0} = 41$ K, and the value of $b = 0.084 \pm 0.003$ can be directly compared with a similar fit to the temperature dependence of the linear dc (pulsed) conductivity [85]. There

$b = 0.29 \pm 0.02$ was obtained, which is about 3.5 times larger than our estimate. The difference may be attributed to two effects: as already discussed, the dc conductivity of Ref. [85] should in fact be considered to be appropriate for frequencies in the kHz range – the strong frequency dependence of the conductivity then introduces large corrections at lower temperatures and the true dc value cannot be obtained from the pulsed measurements alone. Furthermore, our frequency-dependent measurements show that clean BKT vortex dynamics is modified by disorder in LBCO, inducing a stretching of the relaxation process and, plausibly, a distribution of local vortex densities. It is thus naive to expect the 'clean' BKT theory, which predicts a simple Drude dynamical conductivity, to quantitatively describe LBCO. In view of these facts, the theoretical description of the temperature dependence of τ_0 by the Halperin-Nelson function is remarkable, and the agreement between the two values of b obtained from different experiments appears reasonable. We may thus conclude that our dynamic conductivity measurements confirm the basic assumptions of BKT theory in LBCO and reveal a slow vortex fluctuation timescale, while enabling us to quantify the effects of disorder.

It has long been known from lanthanum NMR studies that in 214 cuprates around doping 1/8 the characteristic spin relaxation times have a wide distribution in real space [50, 111, 184], which we have seen is closely related to the glassy slowing-down of spin correlations in the charge stripe state. Clearly the spatially heterogeneous spin relaxation bears an influence on the superconducting dynamics, as displayed by the significant stretching of the conductivity curves in Fig. 3.17. As discussed above, a pure BKT system would have a Drude conductivity relaxation, and the simplest interpretation of the stretching is through a distribution of relaxation times. If we plot the stretching parameter as $1-\beta$ to highlight the deviation from simple Debye-Drude dynamics, a consistent picture emerges. The stretching is small close to $T_{c0} \sim 40$ K, as should be expected by comparison with our Cu NQR relaxation measurements, where no significant stretching is observed as well. $1-\beta$ then increases continuously down to the spin freezing temperature $T_{VTF} \sim 20$ K determined from our Cu NQR experiments and in agreement with previous lanthanum NMR studies. If the theory of intertwined charge, stripe and superconducting orders is taken at face value, the different couplings present in it suggest that a glassy spin dynamics should influence the vortex dynamics and induce heterogeneity as well. Yet this is rather hard to include in a quantitative theory [89].

Interestingly, numerical work on 2D spin systems [220, 221] indicates that disorder

significantly suppresses T_{BKT}; an analogous effect might explain the anomalously broad fluctuation temperature region $\epsilon = 1 - T_{BKT}/T_{c0} \approx 0.6$ present in LBCO. Values of ϵ in thin films are significantly smaller for planar resistivities similar to LBCO [156], a typical value being $\epsilon \approx 0.1$. More detailed numerical simulations of superconducting BKT physics with disorder are necessary to confirm the effect, but it seems plausible that the underlying spin heterogeneity induces dynamical vortex heterogeneity and broadens the fluctuation range.

Further evidence for this comes from nonlinear conductivity measurements we have performed, i.e. the dependence of conductivity on the applied electric field amplitude (Fig. 3.18). Below T_{c0} a large nonlinearity is present at 340 kHz, but not at 10 GHz or in the pulsed kHz measurements (at least above 20 K). Thus there seems to exist a characteristic frequency $\sim 1/\tau_0$ where nonlinear response is strongest. As we have discussed extensively in Chapter 2, nonlinear conductivity is directly related to higher order correlation functions; it has been shown that in glass-forming and dynamically heterogeneous materials the nonlinear response exhibits a peak at a specific frequency related to the heterogeneity scale [167–169]. Our measurements in LBCO therefore create in interesting link to other classes of disordered materials, and indicate that vortex dynamic correlations are important.

The most striking result of our dynamical conductivity studies in LBCO is the appearance of a slow fluctuation timescale τ_0. We stress that τ_0 is many orders of magnitude larger than typical electronic and superconducting scales seen in the cuprates and other conducting systems [130, 144, 145, 222]. Its existence in itself demonstrates that the superconductivity of LBCO-1/8 is highly unconventional, and we have shown that it can be understood within the BKT framework (with included effects of disorder). However, such a slow superconducting timescale has never been observed in other prominent cuprates such as LSCO, YBCO and Hg1201, although it has long been speculated that BKT physics may universally play a role in cuprate superconductivity [145, 223, 224]. It is true that superconductivity is an inherent property of the quasi-two-dimensional CuO_2 planes: interfacial superconductivity in cuprate heterostructures was shown to be possible in a single doped CuO_2 layer in high-precision engineered films [225, 226]. Yet these experiments do not find the characteristic signs of BKT, but instead detect a well-defined T_c and significant Meissner shielding, which should not be possible in a true 2D superconductor [150, 151]. Thus the superconductivity is either not truly limited to one plane,

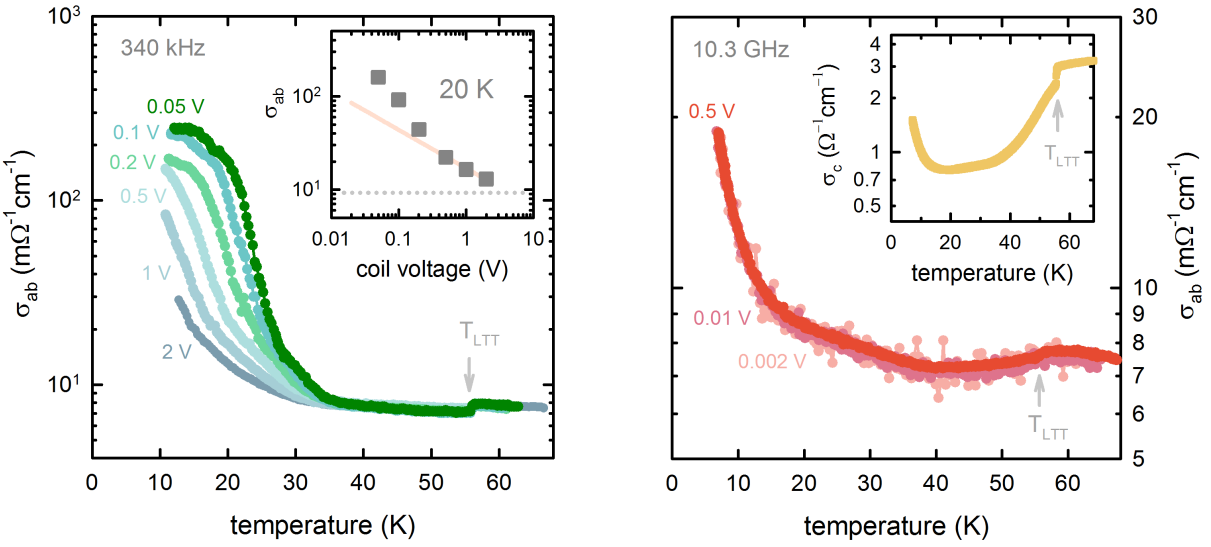

Figure 3.18: LBCO conductivity nonlinearities.
The conductivity of LBCO-1/8 is shown at two frequencies: 340 kHz (left) and 10.3 GHz (right), for different excitation fields. AT the lower frequency, a strong nonlinearity is present below $\sim$ 36 K, signalling the onset of 2D superconducting fluctuations. The left inset shows the dependence of conductivity on applied field (i.e. voltage on the coil), compared to a power law dependence similar to Ref. [85] (line). In the microwave frequency range, no noticeable nonlinearities are present in a wide range of excitation voltages. The right inset shows the c-axis microwave conductivity, with a clearly visible LTT structural transition and increase at low temperatures.

or some as yet unknown aspect of the superconducting mechanism voids the argument that in two spatial dimensions the fluctuations are always too strong for long-range phase coherence to appear. In either case, a BKT interpretation is not plausible. The finding of BKT physics in the exceptional compound LBCO-1/8 therefore highlights the fact that such 2D superconductivity is not the norm in cuprates. In other words, our results are strong evidence against the ubiquity of two-dimensional vortex fluctuations in cuprates, since LBCO is a very special case where the complex interaction of charge and spin stripes with superconductivity induces BKT physics.

Although critical behaviour consistent with 2D exponents has been observed in some underdoped compounds such as LSCO films using microwave conductivity measurements [222], the timescales remain significantly shorter and the fluctuation region much narrower

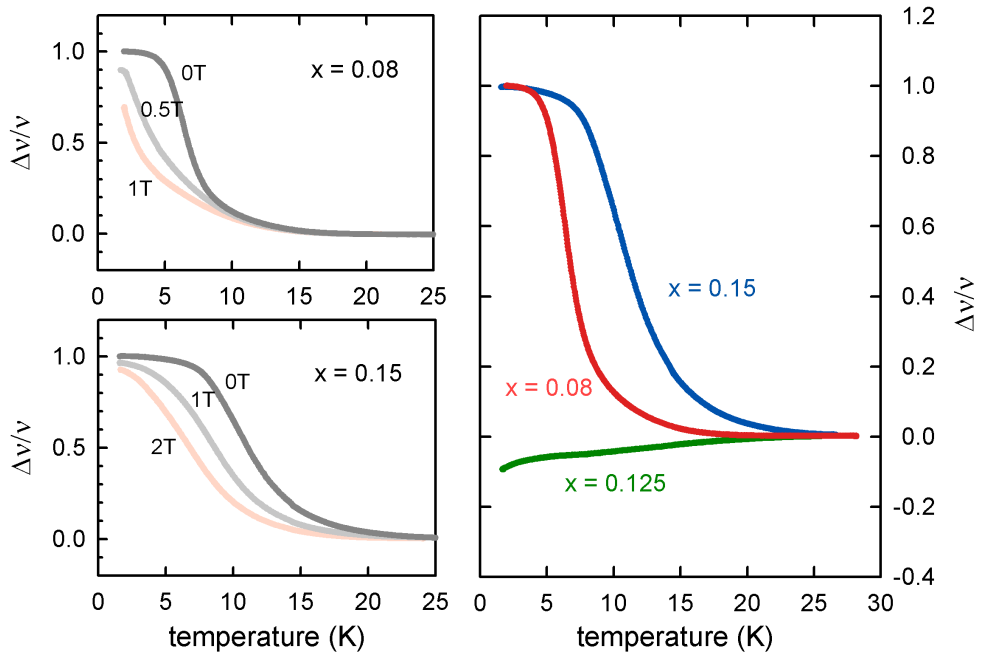

Figure 3.19: Superconductivity of LESCO.
The radiofrequency magnetic susceptibility of three LESCO samples measured at 50 MHz is shown, with doping levels $x = 0.08$, $x = 0.15$ and $x = 0.125$. Bulk superconductivity is clearly observed in the $x = 0.08$ and $x = 0.15$ samples, while the sample with doping 1/8 is not superconducting down to the experimental base temperature.

than what is found in LBCO. Furthermore, several recent studies of different cuprates – including LSCO, YBCO and Hg1201 – demonstrate that superconductivity essentially appears in a three-dimensional way, with a relatively narrow temperature range above T_c where traces of superconductivity are detected [101, 131, 133, 147, 227]. The stark contrast between superconducting fluctuations in LBCO and other cuprates serves to emphasize that the superconducting fluctuations in 'normal' cuprates are not caused by vortex unbinding and two-dimensional physics.

The superconductivity in LBCO-1/8 is clearly exceptional, but that does not imply that it is unique. If charge stripes in LBCO are capable of inducing layer decoupling and two-dimensional superconductivity, it should be expected that similar effects take place in related materials. So far there is little experimental evidence of this [39, 89]. Depressions of bulk T_C around doping 1/8 in representative cuprates such as LSCO and YBCO have long been known, but no clear indication of stripe-induced layer decoupling has been found [39, 89, 228]. Here we investigate the superconductivity of LESCO, a 214

cuprate with prominent stripe order, to compare it to LBCO. Our contact-free conductivity measurement setup is used to determine the conductivity both in the CuO_2 planes and perpendicular to them, for three LESCO samples with different doping concentrations. Three-dimensional bulk superconductivity is clearly seen in samples away from doping 1/8 (Fig. 3.19). Yet the sample with doping 1/8, with the most prominent charge and spin stripe order, does not become superconducting along the c-axis down to the base temperature of our experiment of 1.5 K. In contrast, the in-plane conductivity shows signs of superconductivity as high as 12 K, as demonstrated by the effect of external magnetic fields (Fig. 3.20). Below 12 K the conductivity curves upwards and the fields shift the curve to lower temperatures, consistent with a superconducting response. The rate of shift is roughly 4 K/T, similar to the shift of T_{c0} and T_{BKT} in LBCO [85], but much larger than the change of T_c in external fields for cuprates such as YBCO and LSCO away from doping 1/8 [131, 133, 229–231].

Furthermore, strong current-voltage nonlinearity appears below 12 K in the in-plane response, while the c-axis response remains linear in a wide range of excitation voltages (Fig. 3.20). Low-current measurements below 10 K can be analysed using a power law temperature dependence $\sigma \sim T^{-a}$ with $a \approx 0.2$ – such behaviour was predicted for a 'sliding phase' stack of 2D superconductors [232] and is also observed in LBCO (but in a narrower temperature range and exponent closer to 1) [86]. We note that a previous Nernst effect study of LESCO [233] has also found behaviour consistent with 2D Gaussian fluctuations above T_c. However, the work advocates that 2D superconductivity in LESCO implies an universal importance of similar effects in cuprates. Our experiments clearly demonstrate that such a view is flawed, since other cuprates do not possess the ultra-slow vortex dynamics detected here, and in both LESCO and LBCO the pinned charge order underlies strong layer decoupling. The 2D superconductivity may thus be viewed as an emergent phenomenon limited to doping concentrations around 1/8 and resulting from the interplay between charge stripes and pairing tendencies. While the stripes are clearly responsible for the dramatic interlayer tunnelling frustration, our experiments cannot be seen as strong evidence for (or against) the phase density wave model. Yet we have shown that the stripes are disordered, and this disorder is reflected in the superconducting dynamics. Since the PDW layer decoupling scheme implies well-defined phase differences between density waves in different layers, it seems that in-plane disorder could significantly affect the decoupling.

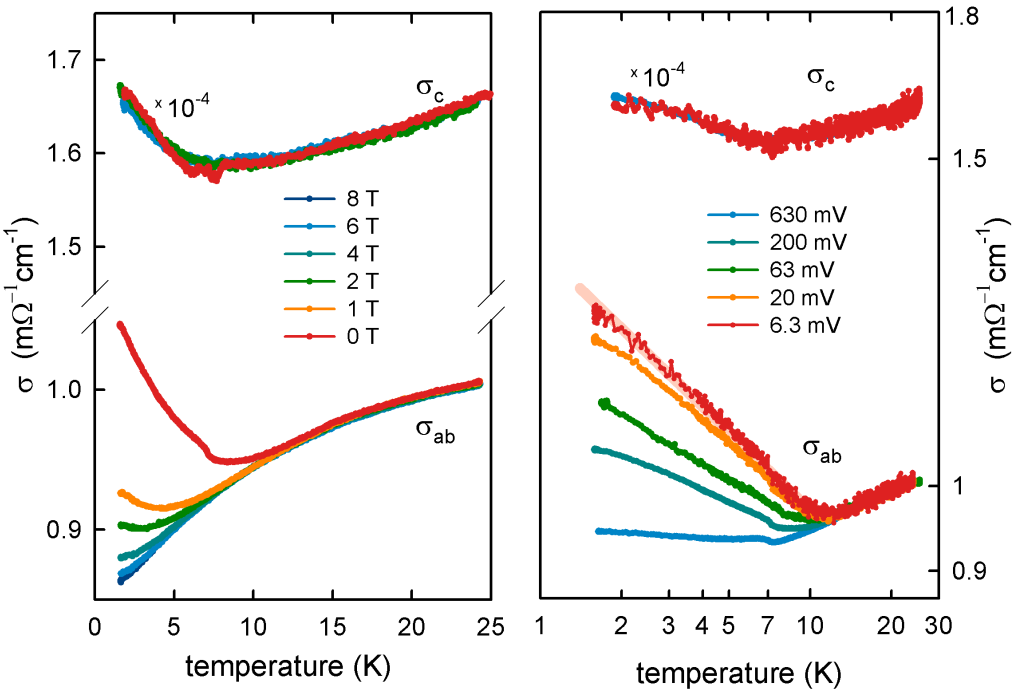

Figure 3.20: Two-dimensional superconductivity in LESCO-1/8.
The in-plane and c-axis conductivity of LESCO-1/8, for different out-of-plane external magnetic fields (left) and excitation voltages (right). The in-plane response is very sensitive to both external fields and changes in excitation amplitude, while the c-axis conductivity is always the same. This strongly suggests the presence of 2D superconducting fluctuations in the sample. The in-plane conductivity for low excitation amplitudes follows a power law in temperature (line), in accordance with theoretical predictions (see text). The small kink at ~ 7 K is the superconducting transition of Pb-Sn solder used in the coil contacts.

The experiments show unambiguously that a two-dimensional superconducting fluctuation state similar to LBCO-1/8 occurs in LESCO-1/8 as well, but the characteristic temperatures are about three times lower in LESCO than in LBCO. We thus cannot clearly observe the BKT transition in LESCO with our setup, since temperatures below 1.5 K are needed. Yet the fluctuation regimes in the two compounds are remarkably similar, except for the overall temperature shift. Putting the effects of charge stripes and layer decoupling aside, the shift itself provides important insight into the makeup of the superconducting condensate, as follows. It has been theoretically argued that symmetric combinations of oxygen orbitals are involved in cuprate superconductivity [6,90,235]. The

canting of CuO octahedra in the LTT structure would then be detrimental to superconductivity [234] because it breaks the symmetry between two oxygen atoms in the unit cell [6, 91, 235]. Co-doped lanthanum cuprates with prominent LTT phases indeed have smaller T_c than their LTT-free counterparts, but so far the effect has not been investigated quantitatively due to the many complications of the 214 phase diagram. Here we have the opportunity to separate the influence of charge order around doping 1/8 from an overall LTT suppression of T_c for two compounds with different T_{LTT}, LESCO and LBCO. If their characteristic temperatures are plotted together, the phase diagrams indeed look similar (Fig. 3.21), with superconductivity shifted to lower temperatures where T_{LTT} is higher.

Phenomenologically, the LTT effect on T_c (and the superconducting onset temperature T_{c0}) can be eliminated if the two scales are multiplied: $T_c \cdot T_{LTT}$ and $T_{c0} \cdot T_{LTT}$ fall on the same curves for both compounds, yielding a universal phase diagram. Of course, the simple multiplication should be taken as a semiquantitative indicator of the suppression of T_c when T_{LTT} increases; it is presumably only useful in a limited range of T_{LTT}, since e.g. if T_{LTT} is very small, T_c will not diverge. An analogous analysis can be made for the neodymium co-doped compound $La_{2-x-y}Nd_ySrxCuO_4$, keeping in mind that it has an additional structural transition to a low temperature less-orthorhombic (LTLO) phase at low doping concentrations [84, 91]. Including only compounds with a well-defined T_{LTT}, we plot the superconducting *onset* temperatures T_{c0} from LNSCO resistivity [84] on the universal phase diagram, obtaining agreement with the values in LBCO and LESCO. To our knowledge, bulk T_c data for the same LNSCO compositions are not available, and are thus not included. Yet magnetic susceptibility studies on samples with different Nd concentrations show a strong suppression of bulk T_c close to doping 1/8, similar to LBCO and LESCO. Notably, in several previous investigations the onset of superconductivity in resistivity was ascribed to sample inhomogeneities [84, 236], since the corresponding bulk T_c is significantly lower around doping 1/8. It is now clear that the large difference is due to stripe-induced two-dimensionality, since a 2D superconductor has negligible Meissner shielding. The effects of stripes and LTT oxygen symmetry breaking are thus clearly separated in the phase diagram in Fig. 3.21.

Charge stripe order and LTT effects in the phase diagram are clearly separated: the stripes induce a suppression of bulk T_c around doping 1/8, but leave the onset temperatures T_{c0} largely intact; the LTT effect is superimposed on the charge stripe effect and

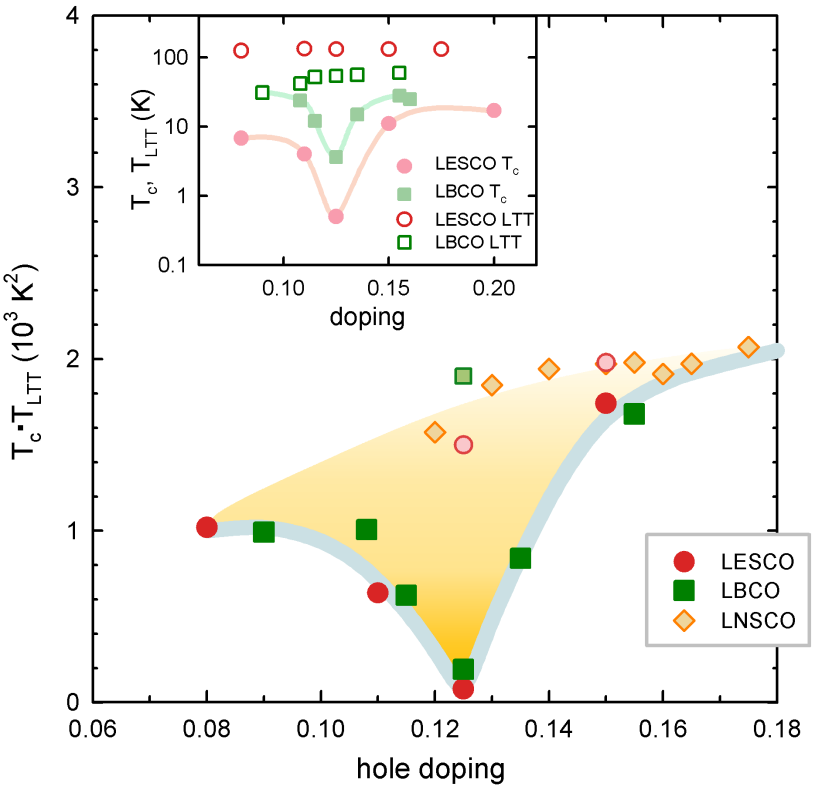

Figure 3.21: Effect of the LTT shift on superconductivity.
The superconducting phase diagram of three lanthanum-based cuprates: LBCO, LESCO and LNSCO, demonstrating the strong influence of the LTT phase on superconductivity. A universal phase diagram is obtained when the superconducting and structural transition temperatures are multiplied. Bulk $T_c \cdot T_{LTT}$ values are shown for LBCO [37] and LESCO (full symbols), while resistivity T_c are plotted for LBCO and LESCO from data ontained in this work, and for LNSCO from available data [84] (empty symbols). The charge-stripe-induced effects around doping 1/8 only influence bulk superconductivity, while the onset temperatures remain roughly the same and follow the well-known parabolic doping dependence once the LTT effect is taken into account. The inset shows the raw phase diagrams of LESCO and LBCO, exhibiting the wide range of transition temperatures involved in the scaling in the main panel.

equally suppresses all forms of superconductivity. The suppression of T_c and T_{c0} is roughly inversely proportional to T_{LTT} over a significant range; the structural transition temperatures for LBCO and LESCO differ by a factor of two. More importantly, no apparent doping dependence of the LTT suppression is seen. We note that in some previous work the LTT tilt angle has been taken as a microscopic measure of the stability of the phase, in place of T_{LTT} [84]. Yet more recent work on LBCO has demonstrated that the tilt angle is not an unambiguous indicator of LTT stability [37]: the tilt angle decreases with doping, while T_{LTT} increases slightly. Other stabilising factors thus come into play, with point disorder being one candidate. The transition temperature is then taken as a more reliable measure of LTT effects here, although a relation between T_{LTT} and microscopic parameters such as oxygen orbital symmetry breaking might not be simple as well. Regardless of the exact pairing mechanism, the oxygen orbital symmetry breaking presumably enters into the effective electron-electron coupling λ, and thus strongly influences T_c due to its exponential dependence on $1/\lambda$.

The suppression of superconductivity by the LTT octahedral tilt has important repercussions for understanding the orbital conditions necessary for high-T_c pairing in cuprates. Generally, in single-layer cuprates T_c is inversely correlated with the deviation of CuO_2 units from perfect squares [91]: the tetragonal material Hg1201 has a maximum $T_{c,max} \sim$ 100 K, compared to the orthorhombic LSCO with $T_{c,max} \sim 40$ K. This indicates that oxygen-oxygen orbital symmetry is beneficial for superconductivity. The notion is confirmed by two further experiments: the influence of the LTT phase discussed here, and a recent study of Zn-substituted YBCO [6], where it is shown that a Zn-induced local oxygen symmetry breaking is responsible for strong T_c suppression. Interestingly, Zn substitution also suppresses charge stripe order in LBCO and stabilizes the LTT structure [237]. This is reasonable, since the LTT and Zn-induced tilts are similar and point to the same physical mechanism. Oxygen symmetry breaking poses a strong constraint on possible theories of high-T_c superconductivity.

Chapter 4

Conclusions and Outlook

This thesis provides comprehensive experimental insight into the behaviour of charge order in cuprates and its relation to superconductivity. Here we summarize the most important open questions addressed by our experiments, put the results in a broader context, and discuss possible avenues for further work.

The first significant result is the evolution of charge stripe order through a precursor charge nematic phase in LESCO. We have shown that the nematic appears through a well-defined phase transition, while charge stripes are not a true thermodynamic phase. Theories of stripe emergence predict precisely such an evolution, and our combined experimental investigation confirms them, highlighting the role of disorder in cuprate charge stripe physics. We gain the first firm experimental evidence of a charge nematic phase in cuprates, establishing a link to other classes of materials with strong electronic correlations that also undergo nematic ordering; prominent examples are pnictide superconductors and quantum Hall systems. Furthermore, our experimental methodology, and especially the newly developed nonlinear response measurement setup, pave the way for further studies of unconventional electronic order in a diverse range of materials. It would be interesting to search for the charge nematic in other tetragonal cuprates as well, with Hg1201 being a prime candidate.

Importantly, the charge nematic transition temperatures we detect in LESCO are well below the pseudogap opening temperatures T^*, thus disproving the direct relation between pseudogap and charge nematic suggested in recent theoretical work. Yet our experiments leave open the possibility for the existence of even more exotic ordered phases such as the tentative loop metal, which might be associated with the pseudogap state. Further work is needed to clarify this issue, but such a connection is in our view unlikely due to the

significantly different evolution of pseudogap and charge order with doping.

Having resolved the thermodynamic properties of charge stripes, we use nuclear magnetic resonance as a local probe of stripe dynamics in LBCO-1/8. The measurements show that charge stripes are strongly pinned to the lattice, in agreement with previous X-ray scattering investigations. Yet our NQR experiments provide a way of estimating the amplitude of the charge modulation, which turns out to be similar in LBCO and other cuprates such as LESCO and YBCO. This suggests that the charge stripe amplitude in cuprates is universal. Nonlinear conductivity measurements in LESCO also detect a stripe pinning-induced signal and confirm the strong pinning of charge stripes in lanthanum-based cuprates. In contrast, the spin stripes induced by the charge order fluctuate intensely and their amplitude significantly depends on the cuprate family. Our fast relaxation NQR experiments demonstrate that these fluctuations are responsible for the decrease of Cu NMR/NQR signal intensity observed in previous work. The nature of the signal wipeout effect is thus resolved after two decades of debate.

Finally, we investigate the unusual two-dimensional superconductivity in LBCO-1/8 induced by charge stripes. Measurements of frequency-dependent conductivity reveal an extremely slow superconducting fluctuation timescale, in line with Berezinski-Kosterlitz-Thouless vortex physics. This confirms that LBCO-1/8 exhibits true 2D superconductivity, and gives credence to the idea of a phase density wave as the origin of CuO_2 layer decoupling. However, effects of disorder on the vortex dynamics are also seen in the conductivity, indicating that a pure BKT description is overly simplistic. To determine if the 2D superconductivity is endemic to LBCO-1/8, we perform conductivity measurements on LESCO, finding similar features at doping 1/8. The experiment allows us to disentangle the influence of charge stripes from a systemic effect of the LTT tilt, which breaks the symmetry between oxygen orbitals in the unit cell. The pronounced doping-independent suppression of superconductivity in the LTT phase suggests that symmetric oxygen orbital combinations are important for cuprate superconductivity in general.

An omnipresent motive throughout our investigations is disorder: it destroys long-range charge stripes, causes stripe pinning and glassy spin dynamics, and influences superconducting vortex fluctuations. Perhaps the most important message of this work is that disorder is a vital ingredient of cuprate physics, and cannot be disregarded in understanding prominent electronic ordering tendencies.

Chapter 5

Nabojne pruge u kupratima

5.1 Uvod.

Predmet istraživanja ovog rada su kupratni supravodiči: materijali koji su u fokusu fizike kondenzirane materije već trideset godina. Unatoč intenzivnom istraživanju, još uvijek ne postoji slaganje oko prirode glavnih značajki kuprata. Od njih je svakako najvažnija supravodljivost – makroskopsko kvantno stanje elektrona u materijalu koje ima električni otpor jednak nuli – ali se pojavljuju i druge srodne elektronski uređene faze. Zbog velikog bogatstva elektronske fizike, možemo reći da su kuprati iznimno kompleksni materijali. Tri su glavna razloga za tu složenost: smanjena efektivna dimenzionalnost, jake korelacije među elektronima, i intrinzični nered.

Kuprati su spojevi perovskitne kristalne strukture na bazi bakra i kisika, čiji su glavni strukturni elementi CuO_2 ravnine. Pri formiranju trodimenzionalnog kristala, CuO_2 ravnine se izmjenjuju s ionskim slojevima koji služe kao rezervoari naboja. Različiti ionski slojevi daju različite obitelji kuprata. Većina zanimljivih elektronskih fenomena odvija se unutar CuO_2 ravnina, i zbog te slojevitosti se kuprati smatraju kvazidvodimenzionalnim materijalima, odnosno materijalima smanjene efektivne dimenzionalnosti. Jake elektronske korelacije nastaju zbog kulonskog odbijanja elektrona u d-orbitalama atoma bakra, što vodi na izolatorsko i antiferomagnetsko osnovno stanje polaznih spojeva kuprata. Konačno, za dobivanje supravodljivosti i ostalih elektronskih uređenja, slobodni nosioci naboja ubacuju se u CuO_2 ravnine dopiranjem ishodišnih spojeva. Kemijski proces dopiranja nužno unosi nered u kristal, no poznato je da su perovskiti i intrinzično skloni lokalnim deformacijama kristalne rešetke. Nered je zato neizbježan aspekt fizike kuprata, i kao što ćemo ovdje pokazati, važan za razumijevanje elektronskih

uređenja.

Fazni dijagram kuprata u kojem su kontrolni parametri dopiranje (odnosno koncentracija slobodnih nosioca naboja) i temperatura ima nekoliko važnih univerzalnih svojstava. Prije svega, nedopirani spojevi su zbog jakih korelacija Mottovi izolatori i antiferomagneti. No već nekoliko postotaka dopiranih šupljina po jediničnoj ćeliji uništava dugodosežni magnetizam, stvara se spinsko staklo i supravodljivost. Temperatura supravodljivog prijelaza je maksimalna oko dopiranja 16%, i ima karakterističan kupolast oblik u faznom dijagramu. Zato se spojeve s dopiranjem ispod 16% naziva poddopiranima, a one iznad 16% naddopiranima. Poddopirano područje faznog dijagrama je naročito zanimljivo zbog pojave elektronskih uređenja, poput još nerazjašnjenog pseudoprocjepa, te nabojnih i spinskih pruga. Nedavno je eksperimentalno ustanovljeno da su nabojne pruge univerzalno prisutne u kupratima, no razumijevanje njihovog nastanka i dinamike je nepotpuno. Stoga su nabojne i spinske pruge glavni predmet ovog istraživanja.

Teoretska istraživanja ponašanja prugastih faza općenito predviđaju da je dugodosežno prugasto uređenje iznimno osjetljivo na nered. U prisutstvu točkastog nereda prugasto uređenje gubi dugodosežne korelacije i postaje staklasto, uz nedostatak pravog faznog prijelaza. Međutim, faza koja lomi samo orijentacijku simetriju, poznata kao nabojni nematik, preživljava i ostaje dobro definirana. Prema tome, nabojne pruge u kupratima bi trebale nastajati postepeno iz nematske faze. Neki teorijski radovi zato povezuju nematik s pseudoprocjepom, zaključujući da je veći dio faznog dijagrama kuprata određen nabojnim uređenjima. Eksperimentalna detekcija nematika i provjera teorijskih razmišljanja prvi je cilj ovog rada.

jednom kad su nabojne pruge formirane, zbog gore spomenute jake interakcije s neredom njihova dinamika postaje netrivijalna. Tu je najvažniji koncept zapinjanja, odnosno onemogućavanja 'klizanja' nabojnih pruga kroz materijal zbog vezanja na lokalne potencijale defekata u kristalnoj rešetci. Dinamika zapinjanja u kupratima je slabo istražena zbog njihove velike vodljivosti i poteškoća s mjerenjem lokalnih odziva poput nuklearne magnetske rezonancije jezgri bakra. Novim eksperimentalnim metodologijama će ovdje biti moguće istraživati i razumjeti dinamiku pruga u reprezentativnim kupratnim spojevima.

Napokon, interakcija nabojnih pruga i spuravodljivosti daje zanimljive nekonvencionalne supravodljive faze, i može pružiti uvid u dimenzionalnost supravodljivosti u kupratima općenito. Mjerenjem eletričnog odziva u širokom rasponu frekvencija dokazat ćemo postojanje prave dvodimenzionalne supravodljivosti pod utjecajem nabojnih pruga,

te usporediti taj specijalni slučaj s tipičnim kupratima bez nabojnih uređenja.

5.2 Eksperimentalne metode.

U ovom radu korišteno je nekoliko komplementarnih eksperimentalnih metoda, s ciljem što potpunije karakterizacije novih elektronskih faza u odabranim kupratima. Naročito važan aspekt eksperimentalnog rada bile su inovacije u primjeni različitih tehnika, koje su omogućile otkrivanje nekonvencionalnih elektronskih uređenja.

Četiri različite tehnike su upotrebljavane u istraživanju: nuklearna magnetska rezonancija (NMR), linearna i nelinearna vodljivost, te diferencijalni toplinski kapacitet. NMR je metoda koja se zasniva na mjerenju koherentnog odziva spinova atomskih jezgri unutar materijala, te daje informacije o lokalnoj elektronskoj fizici. U ovom radu korištene su jezgre bakra, koje se nalaze u CuO_2 ravninama pa daju izravan uvid u njihova lokalna statička i dinamička svojstva. Za opažanje nuklearne rezonancije nužno je da se nuklearni spinski nivoi rascijepe pomoću vanjskog polja. Tada se može manipulirati nuklearnim spinskim sustavom pomoću pulseva izmjeničnog magnetskog polja na frekvenciji koja odgovara cijepanju energija. U slučaju magnetske rezonancije, to vanjsko polje je magnetsko, i procjep između spinskih nivoa je proporcionalan polju. No postoji i druga, srodna tehnika poznata kao nuklearna kvadrupolna rezonancija (NQR), gdje lokalni gradijent električnog polja uzrokuje cijepanje. S obzirom da lokalna električna polja ovise o gustoći naboja, NQR je posebno pogodna tehnika za proučavanje nabojnih uređenja. Statički NQR spektri izravno daju informaciju o raspodjeli nabojne gustoće. Dinamička svojstva mogu se također istraživati, mjerenjem relaksacijskih vremena nuklearnih spinova. Spinski sustav ima dva karakteristična vremena: spin-rešetka relaksacijsko vrijeme T_1, koje mjeri brzinu izmjene energije spinova s okolinom u materijalu, te vrijeme spinske dekoherencije T_2. Općenito se može pokazati da je u sistemima s vodljivim elektronima domantni doprinos spin-rešetka relaksaciji proporcionalan elektronskoj spinskoj susceptibilnosti, što daje jednostavnu mjeru te važne veličine. Teorija dekohenercije je nešto složenija, no T_2 u principu ovisi o lokalnim magnetskim poljima i daje informaciju o njihovim fluktuacijama. U ovom radu su kombinirana mjerenja statičkih NQR i NMR spektara za dobivanje informacije o lokalnim gustoćama naboja, te mjerenja T_1 i T_2 za određivanje niskofrekventne dinamike elektronskih spinova.

U praksi se za mjerenje NMR/NQR signala koristi metoda spinske jeke, pa deko-

herencijsko vrijeme T_2 ograničava brzinu mjerenja. Ako T_2 padne ispod ~ 15 μs, mjerenja uobičajenim postupcima su znatno otežana, no u kupratima s nabojnim uređenjem se upravo to događa. Zato je osmišljena nova metodologija za eksperimente koji omogućuju određivanje vrijednosti T_2 kraćih od 3 μs. Najvažniji elementi su signalno predpojačalo s kratkim vremenom zasićenja, uvođenje pasivnog gušenja, te posebna sekvenca cikliranja faza pulseva.

Linearna i nelinearna vodljivost mjerene su sličnim metodama, koje eliminiraju kontakte na uzorku i omogućuju eksperimente u širokom rasponu frekvencija. Uzorci se stavljaju u zavojnicu, koja je dio rezonantnog LC kruga ili mikrovalne šupljine. Za mjerenje linearne vodljivosti, dovoljno je odrediti rezonantnu frekvenciju i Q-faktor kruga sa i bez uzorka. Za nelinearnu vodljivost potreban je dodatni pobudni krug. Nelinearna vodljivost se općenito definira kao najniža korekcija uobičajenom Ohmovom zakonu, odnosno u shematskom obliku

$$j = \sigma E + \sigma_3 E^3 + ... \tag{5.1}$$

gdje je j gustoća električne struje, E vanjsko električno polje, σ linearna vodljivost i σ_3 nelinearna vodljivost trećeg reda. Odziv drugog reda je simetrijski ograničen i u većini slučajeva jednak nuli. Naravno, u anizotropnom materijalu poput kuprata je σ tenzor drugog reda, σ_3 tenzor četvrtog reda, i tako dalje. Ako je električno polje oscilatorno u vremenu s frekvencijom ω, lako je pokazati da će signal na frekvenciji 3ω biti proporcionalan komponentama σ_3. Zato pobudni krug u eksperimentu stvara polje neke frekvencije (tipično reda 10 MHz), a detekcijski krug je namješten na trostruku frekvenciju. Visoka primijenjena frekvencija polja eliminira najvažniji izvor artefakata u mjerenju nelinearne vodljivosti – grijanje uzorka. Naime, ako je oscilacija polja dovoljno spora, temperatura uzorka može pratiti polje i dovesti do signala na trostrukoj frekvenciji koji nema veze s intrinzičnim nelinearnim odzivom. U našem slučaju je frekvencija dovoljno visoka da nema temperaturnih oscilacija.

Linearna vodljivost u širokom rasponu frekvencija dat će nam informaciju o supravodljivim relaksacijama, dok je nelinearna vodljivost iznimno pogodna proba za nematske fluktuacije. Na temperaturi faznog prijelaza iz Fermijeve tekućine u nematik, fluktuacije nematskog parametra reda divergiraju; detekcija te divergencije daje jednoznačnu potvrdu prirode prijelaza. Unutar teorije Fermijevih tekućina u blizini nematske nestabilnosti Fermijeve površine (Pomerančukova nestabilnost) može se pokazati da je $\sigma_3 \sim \chi_N$, gdje je χ_N nematska susceptibilnost. Ta veza je posljedica iste kvadrupolne simetrije nematskog

parametra reda i tenzora odziva trećeg stupnja.

Posljednja korištena eksperimentalna tehnika je diferencijalna metoda mjerenja toplinskog kapaciteta. Toplinski kapacitet je ključan za određivanje prirode faznih prijelaza, ali je za male uzorke teško odvojiti veliki fononski doprinos od malog elektronskog. Zato je izrađena proba za mjerenje metodom diferencijalne termalne analize, u kojoj se mjeri relativno kašnjenje temperature uzorka za referentnim senzorom. Ako se temperatura reference mijenja jednoliko u vremenu, razlika temperatura uzorka i reference je proporcionalna toplinskom kapacitetu uzorka. Za mjerenje na uzorcima malih masa, korišteni su platinski otporni senzori u visokom vakuumu, uz veliku stabilnost i osjetljivost.

Kao reprezentativni sustavi za proučavanje nabojnih uređenja odabrani su kuprati na bazi lantana, s ishodišnim spojem La_2CuO_4. Kod njih se dopiranje postiže zamjenom dijela atoma lantana dvovalentnim ionima poput stroncija ili barija. Također, moguće je i izovalentno dopiranje, npr. europijem. Dvije obitelji lantanovih kuprata su naročito pogodne: $La_{2-x}Ba_xCuO_4$ (LBCO) i $La_{2-x-y}Eu_ySr_xCuO_4$ (LESCO). Visokokvalitetni monokristali tih kuprata dobiveni su metodom rasta plutajuće zone i karakterizirani u brojnim prethodnim istraživanjima.

5.3 Rezultati i diskusija.

Najvažniji rezultati ovog rada mogu se podijeliti u tri skupine: razjašnjavanje nastanka nabojnih pruga i pronalazak nematske faze; istraživanje dinamike zapinjanja nabojnih pruga; te interakcija pruga sa supravodljivošću.

Kombinacijom mjerenja intenziteta NQR signala na jezgrama bakra, nelinearne vodljivosti i specifičnog toplinskog kapaciteta jednoznačno je pokazano da se nabojne pruge u kupratu LESCO formiraju postepeno, te da postoji nematska faza. Iz toplinskog kapaciteta se vidi da nabojno nematsko uređenje nastaje na pravom termodinamičkom faznom prijelazu, koji je opažen u uzorcima različitih dopiranja u blizini $x = 0.125$. Također, nelinearna vodljivost σ_3 daje divergenciju odgovarajuće nematske susceptibilnosti na temperaturi faznog prijelaza. Ti rezultati su u skladu s teorijskim predviđanjima za nastanak nabojnih pruga u prisutstvu nereda, i predstavljaju prvo jednoznačno eksperimentalno opažanje nabojnog nematika u kupratima. Međutim, u faznom dijagramu nematska faza usko prati nabojne pruge, i nastaje na temperaturama znatno nižim od temperatura otvaranja pseudoprocjepa. Prema tome veza između nematika i pseudoprocjepa ne može

biti izravna, što opovrgava neke teorijske pretpostavke. Zanimljivo je da mjerenja nematske susceptibilnosti pokazuju njen znatan porast na temperaturama iznad nematskog faznog prijelaza, ukazujući na prisutstvo jakih nematskih fluktuacija. To je u skladu s nedavnim opažanjima lokalnog nematiciteta u raspršenju X-zraka, i može se povezati s teorijski predviđenom egzotičnom fazom poznatom kao 'loop metal'. No za potvrđivanje postojanja takve faze, potrebni su dodatni eksperimenti. Također je zanimljivo pitanje univerzalnosti nabojnih nematika u kupratima – iz naših rezultata bilo bi očekivano da i u drugim kupratima (npr. u tetragonalnom $HgBa_2CuO_{4+\delta}$) nabojne pruge nastaju kroz nematsku fazu.

Zbog utjecaja nereda i zapinjanja nabojnih pruga, njihova dinamika je zanimljiva i relativno neistražena. U kupratima se uz nabojne pruge veže i pojava jakih fluktuacija elektronskih spinova, te staklaste spinske pruge. Drugi dio rezultata bavi se tim dinamičkim fenomenima, koristeći modelni kuprat s nabojnim prugama LBCO (dopiranje $x = 0.125$). U njemu je ovdje po prvi puta izmjeren NQR signal bakra ispod temperature nastanka nabojnih pruga, koji je dosad bio nedostupan zbog vrlo brze spinske dekoherencije (takozvani 'wipeout' efekt). Spektar bakra se ukupno sastoji od četiri linije, po dva para za dva izotopa ^{63}Cu i ^{65}Cu. Parovi linija dolaze od različitih okruženja atoma bakra – u blizini dopanda barija, ili daleko od njega. U nabojno uređenoj fazi, opažen je znatan porast širine linija bakra, što je očekivano za statične inkomenzurabilne nabojne pruge. Širina linija je izravno povezana s nabojnim parametrom reda, koji je nezavisno mjeren raspršenjem X-zraka u prethodnim istraživanjima. Ovi rezultati pokazuju da je nabojno uređenje kvazi-statično u LBCO, dok vrlo kratka vremena spinske dekoherencije i spin-rešetka relaksacije ukazuju na snažne fluktuacije elektronskih spinova. Sistematskim mjerenjem temperaturnih ovisnosti relaksacijskih vremena, te usporedbom njihovih vrijednosti za dva izotopa bakra, potvrđen je magnetski karakter relaksacija i pokazano je da spinske fluktuacije prate temperaturnu ovisnost karakterističnu za staklaste tekućine. To se slaže s prethodnim, neizravnim istraživanjima LBCO preko nuklearne magnetske rezonancije jezgri lantana. Također, na spinsku dekoherenciju snažno utječe vanjsko magnetsko polje unutar CuO_2 ravnina, koje stvara preferirani smjer za fluktuacije elektronskih spinova i time ih potiskuje.

Uz mjerenje NQR bakra u LBCO, dinamika nabojnih pruga proučavana je i u spoju LESCO mjerenjem nelinearne vodljivosti na niskim temperaturama, gdje su pruge već formirane. Tamo je opažena karakteristična ovisnost nelinearnod odziva o vanjskom elek-

tričnom polju, koja je u skladu s jednostavnim teorijama zapinjanja nabojnih pruga. Određeno je da su kritična polja zapinjanja reda veličine 10 V/cm ili veća, što je znatno više od klasičnih kvazi-jednodimenzionalnih sustava s valovima gustoće naboja.

Napokon, iz prethodnih istraživanja vodljivosti spoja LBCO na dopiranju $x = 0.125 = 1/8$ postoje indikacije za dvodimenzionalnu supravodljivost, opisanu Berezinski-Kosterlitz-Thouless (BKT) teorijom. Općenito je zbog slojevite strukture kuprata dimenzionalnost njihove supravodljivosti važno pitanje. No ponašanje u skladu s BKT predviđanjima za čistu dvodimenzionalnu supravodljivost nije opaženo ni u jednom spoju osim LBCO-1/8, gdje zato mora postojati neki mehanizam razvezivanja CuO_2 ravnina. Da bismo dokazali primjenjivost BKT teorije u LBCO-1/8, mjerena je električna vodljivost u širokom rasponu frekvencija, gdje je pronađen karakteristični niskofrekventni relaksacijski proces. Tipične vremenske skale su reda 0.1 ms, što je očekivano za dinamiku razvezanih supravodljivih vrtloga i antivrtloga u BKT sustavima. To je nezavisan i jak dokaz postojanja dvodimenzionalnih supravodljivih fluktuacija u LBCO-1/8. No nepostojanje takve relaksacije u drugim kupratima ukazuje da u njima općenito BKT fizika nije relevantna za supravodljivi prijelaz. Baš suprotno – nedavna mjerenja mikrovalne vodljivosti u reprezentativnim spojevima pokazuju da supravodljivost u principu nastaje na jednak način unutar ravnina i okomito na njih.

Da bismo istražili povezanost nabojnih pruga i dvodimenzionalne supravodljivosti, proučavan je i kuprat LESCO na isti način kao LBCO-1/8. U njemu je također oko dopiranja 1/8 opaženo odvajanje CuO_2 ravnina i pojava dvodimenzionalnosti, što pokazuje da međuigra nabojnih pruga i supravodljivosti općenito može dovesti do takvih efekata. To daje potporu teorijskoj ideji o valu gustoće faze (phase density wave – PDW), u kojoj međudjelovanjem nabojnih pruga i supravodljivog sparivanja nastaje prostorno modulirana supravodljivost. Slaganjem takvih valova gustoće faze u ravninama moguće je značajno smanjiti vezanje među ravnina. Međutim, uz efekt nabojnih pruga, proučavanje supravodljivosti LBCO i LESCO daje nam mogućnost ocjene drugog važnog utjecaja: niskotemepraturne tetragonalne (LTT) strukture. Naime, većina lantanovih kuprata na niskim temperaturama prelazi u LTT fazu, koja uključuje rotaciju oktaedarskih jedinica CuO_6 i slama simetriju duljina veza između kisika i bakra u CuO_2 ravninama. LTT struktura u pravilu potiskuje supravodljivost, no ovdje imamo priliku kvantitativno ocijeniti njen utjecaj. Usporedbom LBCO, LESCO i neodimijem ko-dopiranog kuprata LNSCO pokazuje se da je temperatura supravodljivog prijelaza obrnuto proporcionalna tempera-

turi LTT prijelaza, bez obzira na dopiranje. Ovakav sistematski utjecaj LTT faze pokazuje da je simetrija orbitala kisika važna za supravodljivost, i u skladu je s prethodnim mjerenjima lokalne strukture u kupratima gdje je mali postotak bakra zamijenjen cinkom. Efekt cinka je identičan efektu LTT strukture: lom lokalne simetrije dvaju kisika vezanih na bakar i snažno potiskivanje supravodljivosti. Simetrične kombinacije orbitala kisika prema tome igraju bitnu ulogu u supravodljivom mehanizmu.

5.4 Zaključci.

Četiri su glavna zaključka ovog rada: nabojne pruge u lantanovim kupratima nastaju kroz dobro definiranu fazu nabojnog nematika; vezanje nabojnih pruga za rešetku je jako, dok spinski stupnjevi slobode fluktuiraju; međudjelovanje nabojnih pruga i supravodljivosti može dovesti do pojave nekonvencionalne dvodimenzionalne supravodljivosti u trodimenzionalnim kristalima, ali kupratna supravodljivost u pravilu nije intrinzično dvodimenzionalna; i na kraju, LTT faza i lom simetrije kisika vezanih na bakar univerzalno potiskuje supravodljivost, što ukazuje na važnost simetričnih kombinacija orbitala kisika u supravodljivom mehanizmu. Ti zaključci predstavljaju bitan doprinos razumijevanju fizike kuprata, naročito nabojnih pruga i srodnih uređenja, te daju poveznice s drugim materijalima poput pniktidnih supravodiča, manganata, kobaltata itd. u kojima je nabojni i nematski red prisutan. Naposlijetku, zaključci vezani uz supravodljivi mehanizam predstavljaju test za bilo koju teoriju visokotemperaturne supravodljivosti u kupratima.

Appendix A

Cu NMR frequencies

The determination of Cu NMR resonant frequencies in the case of comparable quadrupolar and Zeeman contributions is described here. As discussed in Sections 2.1 and 3.2, the full NMR Hamiltonian must be considered to calculate the resonant frequencies of copper in lanthanum-based cuprates, if the external magnetic fields are neither too large nor too small. We are interested in the case of in-plane magnetic fields, since they affect the spin fluctuations associated with charge stripes much more than out-of-plane fields [111]. In cuprates the electric field gradient (EFG) tensor at the Cu site is nearly axially symmetric, with the symmetry axis perpendicular to the CuO_2 planes. The NMR Hamiltonian reads [117]

$$\mathcal{H} = -\gamma \mathbf{BI} + \frac{e^2 Q V_{zz}}{4I(2I-1)} \left[3I_z^2 - I^2 + \eta \left(I_x^2 - I_y^2 \right) \right] \tag{A.1}$$

where η is the asymmetry parameter which is ≈ 0 in LBCO and similar compounds, I is the nuclear spin, B the local magnetic field and Q the nuclear quadrupole moment. The z-axis is taken to be the EFG symmetry axis, implying that in in-plane field only has x or y components. The spin Hilbert space of a spin-3/2 nucleus such as Cu is four-dimensional, and in principle four eigenvalues are found by diagonalization of the Hamiltonian. The case of pure NRQ, i.e. when $B = 0$, is easily diagonalized, yielding only two degenerate energy levels. The single resonant frequency is ν_Q, which is between 30 and 40 MHz in most cuprates. The limiting case of small B can be solved by perturbation techniques around the pure NQR eigenstates [117]. Yet if the in-plane field is of the order of 1 T, it can no longer be treated as small, and numerical diagonalization of the full Hamiltonian becomes necessary. The following Mathematica code only finds the eigenvalues and transition frequencies:

The computed frequencies are shown in Figs. 2-1 and 3-15. To evaluate the transition

```
νQ = 34.55;
νL = 0.1*11.285;
i = 1;
freq1 = Array[0, 10000];
freq2 = Array[0, 10000];
freq3 = Array[0, 10000];
freq4 = Array[0, 10000];
freq5 = Array[0, 10000];
freq6 = Array[0, 10000];
polja = Array[0, 10000];
While[νL < 40,
 m = Eigenvalues[{{-3/2*νL - 1/4*νQ, 0, Sqrt[3]/4*νQ, 0},
    {0, -1/2*νL + 1/4*νQ, 0, Sqrt[3]/4*νQ}, {Sqrt[3]/4*νQ, 0, 1/2*νL + 1/4*νQ, 0},
    {0, Sqrt[3]/4*νQ, 0, 3/2*νL - 1/4*νQ}}];
 freq1[[i]] = Abs[m[[1]] - m[[2]]];
 freq2[[i]] = Abs[m[[1]] - m[[3]]];
 freq3[[i]] = Abs[m[[1]] - m[[4]]];
 freq4[[i]] = Abs[m[[2]] - m[[3]]];
 freq5[[i]] = Abs[m[[2]] - m[[4]]];
 freq6[[i]] = Abs[m[[3]] - m[[4]]];
 polja[[i]] = νL/11.285;
 νL = νL + 0.1*11.285;
 i++;
]
data1 = Thread[{polja, freq1}]
data2 = Thread[{polja, freq2}];
data3 = Thread[{polja, freq3}];
data4 = Thread[{polja, freq4}];
data5 = Thread[{polja, freq5}];
data6 = Thread[{polja, freq6}];
```

intensities, one must compute the matrix elements between the eigenstates with corresponding eigenvalues. The eigenstates are superpositions of the elementary spin levels, and in principle the matrix elements are rather complex.

Appendix B

The nematic susceptibility

In this Appendix we detail some of the steps in calculating the nonlinear response of an isotropic Fermi liquid discussed in Section 2.2. In particular, we address the k-space gradient of quantities such as $v_k P_l(\cos\theta)$, where $v_k = \partial\mathcal{E}_k\partial k$ is the quasiparticle group velocity and P_l the l-th order Legendre polynomial. These expressions appear on the right-hand side of the recursive equations of motion for the second-order and third-order equilibrium deviations $\delta\bar{n}_k^{(2)}$ and $\delta\bar{n}_k^{(3)}$. In calculating second-order response, we need to find $\mathbf{E}\cdot\nabla_{\mathbf{k}} v_k P_1(\cos\theta)$, which for a spherically symmetric system is equal to

$$\mathbf{E}\cdot\left(\hat{\mathbf{k}}\frac{\partial}{\partial k}+\frac{\hat{\theta}}{k}\frac{\partial}{\partial\theta}\right)v_k\cos\theta = E\left(\cos^2\theta\frac{\partial v_k}{\partial k}+\sin^2\theta\frac{v_k}{k}\right) \tag{B.1}$$

where $\hat{\mathbf{k}}$ and $\hat{\theta}$ are unit vectors, and the angle between the electric field and $\hat{k}$ is taken to be θ. The terms in parentheses can be collected to give

$$\cos^2\theta k\frac{\partial}{\partial k}\frac{v_k}{k}+\frac{v_k}{k} \tag{B.2}$$

where we have used that

$$\frac{\partial v_k}{\partial k}-\frac{v_k}{k} = k\frac{\partial}{\partial k}\frac{v_k}{k} \tag{B.3}$$

The angle-dependent term can now be expressed through Legendre polynomials to enable solving the equation different components of $\delta\bar{n}_k^{(2)}$. Using that $P_2(\cos\theta) = \frac{1}{2}(3\cos^2\theta - 1)$, we easily obtain the right-hand side of eq. (2.24). A further simplification is possible by observing that

$$\frac{\partial v_k}{\partial k}+2\frac{v_k}{k} = \frac{1}{k^2}\frac{\partial}{\partial k}v_k k^2 \tag{B.4}$$

Similar calculations are used in solving the transport equation for the third-order term,

eq. (2.23c). The relevant gradients are

$$\mathbf{E}\cdot\left(\hat{\mathbf{k}}\frac{\partial}{\partial k}+\frac{\hat{\theta}}{k}\frac{\partial}{\partial\theta}\right)k\frac{\partial}{\partial k}\frac{v_k}{k}P_2(\cos\theta) \tag{B.5a}$$

$$\mathbf{E}\cdot\left(\hat{\mathbf{k}}\frac{\partial}{\partial k}+\frac{\hat{\theta}}{k}\frac{\partial}{\partial\theta}\right)\frac{1}{k^2}\frac{\partial}{\partial k}v_k k^2 P_0(\cos\theta) \tag{B.5b}$$

As above, the angle between $\mathbf{E}$ and $\hat{\mathbf{k}}$ is θ, and $P_0(\cos\theta)=1$. In terms of θ, the gradients then become

$$\frac{1}{2}\frac{\partial}{\partial k}k\frac{\partial}{\partial k}\frac{v_k}{k}\cos\theta\left(3\cos^2\theta-1\right)+3\frac{\partial}{\partial k}\frac{v_k}{k}\cos\theta\left(\cos^2\theta-1\right) \tag{B.6a}$$

$$\frac{\partial}{\partial k}\frac{1}{k^2}\frac{\partial}{\partial k}v_k k^2\cos\theta \tag{B.6b}$$

To determine the Legendre components of the third order response, we must transform the angular terms into Legendre polynomials, using that $\cos^3\theta=\frac{3}{5}P_1(\cos\theta)+\frac{2}{5}P_3(\cos\theta)$. Inserting this relation into eq. (B.6), collecting the terms and noting that

$$3\frac{\partial}{\partial k}\frac{v_k}{k}+k\frac{\partial^2}{\partial k^2}\frac{v_k}{k}=\frac{1}{k^2}\frac{\partial}{\partial k}k^3\frac{\partial}{\partial k}\frac{v_k}{k} \tag{B.7a}$$

$$-2\frac{\partial}{\partial k}\frac{v_k}{k}+k\frac{\partial^2}{\partial k^2}\frac{v_k}{k}=k^3\frac{\partial}{\partial k}\frac{1}{k^2}\frac{\partial}{\partial k}\frac{v_k}{k} \tag{B.7b}$$

the equation of motion (2.26) is obtained.

Appendix C

The specific heat probe

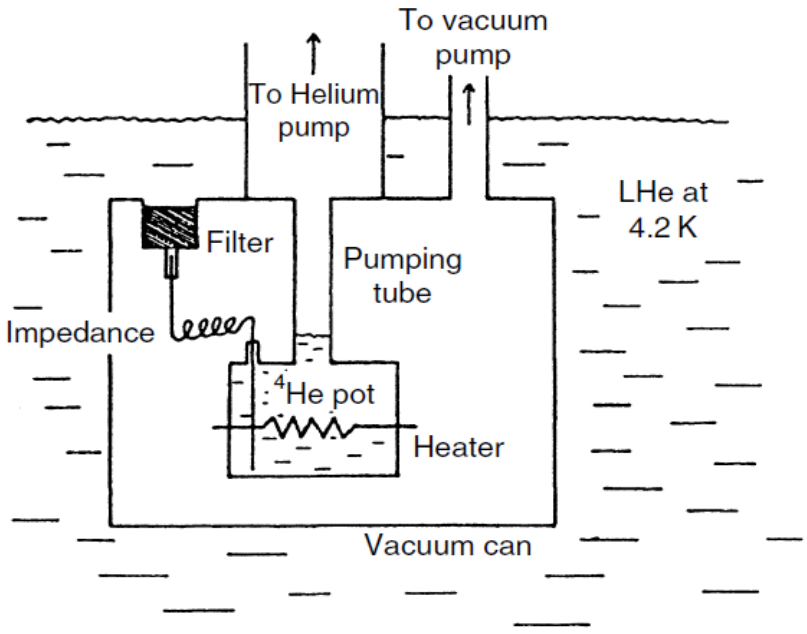

Figure C.1: The 1K pot probe.

A schematic representation of a continuously operating 1K pot probe is shown. The sample platform is suspended from the 1K pot with an intermediate heat conduction neck (not shown). Adapted from [180].

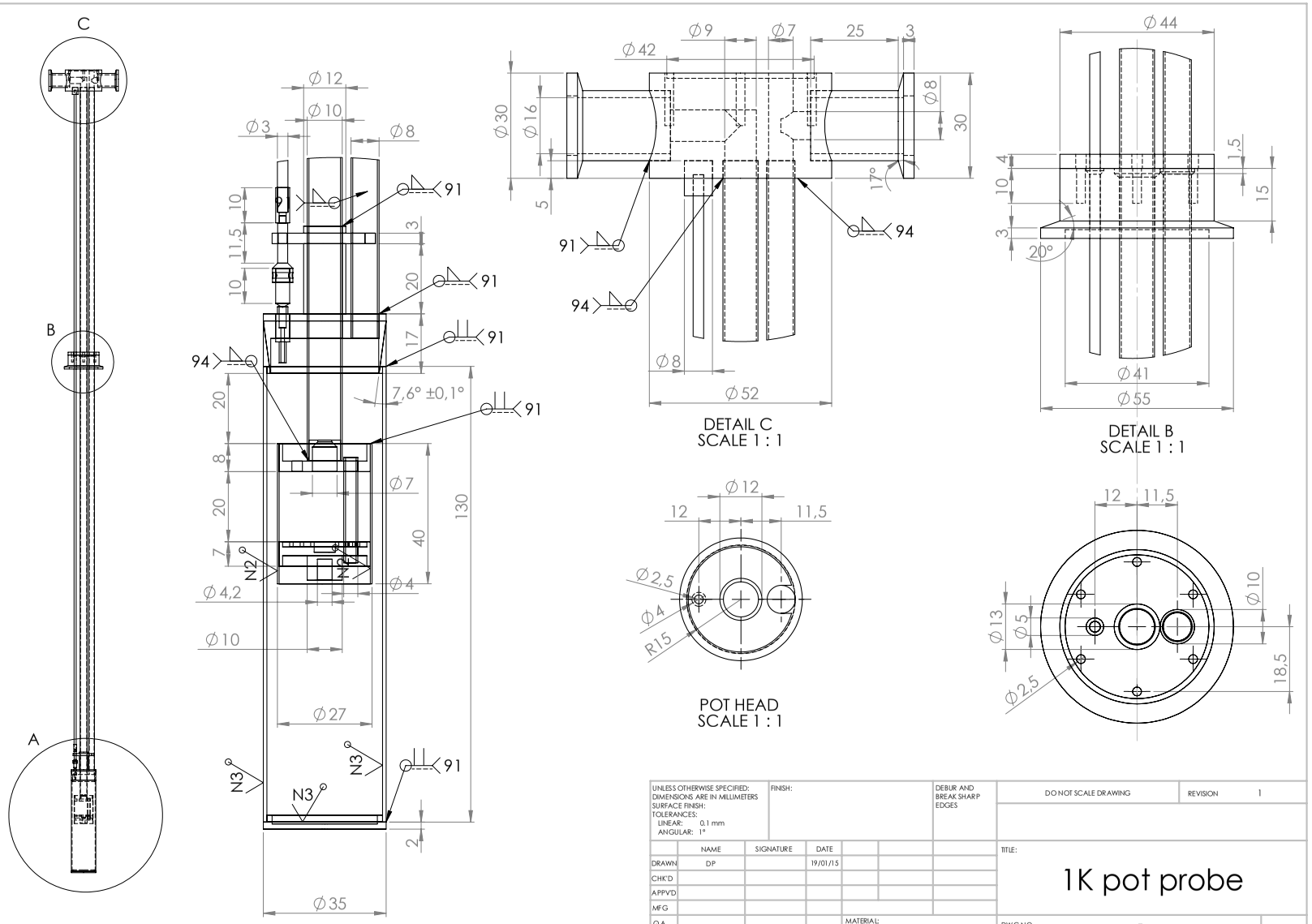
C
B
A
∅12
∅10
∅3
∅8
91
94
7,6° ±0,1°
∅7
∅4
∅4,2
∅10
∅27
∅35
N2
N3
130
40
DETAIL A
SCALE 1 : 1
∅9
∅7
25
3
∅42
∅30
∅16
∅8
30
17°
5
∅52
DETAIL C
SCALE 1 : 1
∅44
∅41
∅55
1,5
15
4
10
3
20°
DETAIL B
SCALE 1 : 1
12
11,5
∅2,5
R15
POT HEAD
SCALE 1 : 1
∅13
∅5
18,5
UNLESS OTHERWISE SPECIFIED:
DIMENSIONS ARE IN MILLIMETERS
SURFACE FINISH:
TOLERANCES:
LINEAR: 0.1 mm
ANGULAR: 1°
FINISH:
DEBUR AND BREAK SHARP EDGES
DO NOT SCALE DRAWING
REVISION 1
NAME
SIGNATURE
DATE
DRAWN DP 19/01/15
CHK'D
APPV'D
MFG
Q.A
MATERIAL:
WEIGHT:
TITLE:
1K pot probe
DWG NO. 1
A3
SCALE: 1:5
SHEET 1 OF 1

Appendix D

Stripe pinning

Here we describe the procedure of solving the stripe equation of motion in a one-dimensional periodic pinning potential, as discussed in Section 3.2. The starting equation is the reduced equation of motion, with neglected inertial term and sinusoidal pinning potential,

$$\Gamma \frac{d\xi}{dt} + \omega_0 \sin \xi(t) = E_{ext} \cos \omega t \tag{D.1}$$

where Γ is the damping coefficient, ω_0 a measure of the pinning potential depth, E_{ext} the external electric field, and ω the external field oscillation frequency. The equation of motion cannot be solved in closed form for large external fields, and we thus use a numerical procedure. It is divided in two parts: (i) solving the differential equation for $\xi(t)$; (ii) calculating the Fourier transform of $\xi(t)$ to obtain the response at 3ω, which is measured in experiments. The entire procedure is repeated for different values of the external field, to calculate the dependence of third harmonic response on external field for comparison with experiment. We do not use a fast Fourier transform routine, but the exact formula for the Fourier coefficient at 3ω. The Mathematica code for the calculation is as follows:

```
Needs["FourierSeries`"]
Γ = 10;
Etl = 0.6;
Ω = 1 / 1000;
MM = Array[0, 150];
xx = Array[0, 150];
ii = 1;
Ξ = 5;
While[Etl < 1.1,
 If[Etl < 0.98,
    s = NDSolve[{Γ * ϕ'[t] + Ω * Sin[ϕ[t]] == Etl * Cos[t], ϕ[-10 * π] == 0}, ϕ, {t, -0.01, 4 * π},
      MaxSteps → 100 000];
   MM[[ii]] =
    Sqrt[
     (2 * NIntegrate[(Evaluate[ϕ'[t] /. s]) * Cos[3 * t], {t, 0, 2 * π}, MaxRecursion → 13,
          WorkingPrecision → 50]) ^ 2 +
      (2 * NIntegrate[(Evaluate[ϕ'[t] /. s]) * Sin[3 * t], {t, 0, 2 * π}, MaxRecursion → 13,
          WorkingPrecision → 50]) ^ 2],
   MM[[ii]] =
     {Sqrt[
       (2 * NIntegrate[(Piecewise[{{-Sign[Sin[t]], Abs[Etl * Cos[t]] ≤ 1},
                {-Sign[Sin[t]] + Ξ * (Etl ^ 2 * (Cos[t]) ^ 2 - 1) ^ (1 / 2) * Sign[Cos[t]],
                 Abs[Etl * Cos[t]] > 1}}]) * Cos[3 * t], {t, 0, 2 * π}, MaxRecursion → 13,
            WorkingPrecision → 50]) ^ 2 +
        (2 * NIntegrate[(Piecewise[{{-Sign[Sin[t]], Abs[Etl * Cos[t]] ≤ 1},
                {-Sign[Sin[t]] + Ξ * (Etl ^ 2 * (Cos[t]) ^ 2 - 1) ^ (1 / 2) * Sign[Cos[t]],
                 Abs[Etl * Cos[t]] > 1}}]) * Sin[3 * t], {t, 0, 2 * π}, MaxRecursion → 13,
            WorkingPrecision → 50]) ^ 2]};
  ]
  xx[[ii]] = Etl;
 Etl = Etl + 0.05;
 ii++
]
```

Appendix E

The Davidson-Cole distribution

The general form of the Havriliak-Negami relaxation function discussed in Section 3.3,

$$\sigma_\infty + \frac{\sigma_0}{\left[1 + (i\omega\tau_0)^\alpha\right]^\beta} \tag{E.1}$$

becomes the Davidson-Cole relaxation if $\alpha = 1$. The complex relaxation function can be separated into real and imaginary parts

$$\Re\sigma(\omega) = \sigma_\infty + \sigma_0 \cos\beta\phi \left(1 + \omega^2\tau_0^2\right)^{-\beta/2} \tag{E.2a}$$

$$\Im\sigma(\omega) = \sigma_0 \sin\beta\phi \left(1 + \omega^2\tau_0^2\right)^{-\beta/2} \tag{E.2b}$$

where σ_∞ is the high-frequency conductivity, σ_0 the low-frequency conductivity step height, τ_0 is the relaxation time, β the stretching exponent, and $\tan\phi = \omega\tau_0$. The Davidson-Cole relaxation may be analysed as a superposition of elementary Debye-Drude relaxations with different characteristic times τ_D. To find the relaxation time distribution, a full Havriliak-Negami relaxation distribution must be used, taking the limit $\alpha \to 1$ as the last step. The HN relaxation time distribution function is [219]

$$g\left(\ln\tau_D\right) = \frac{1}{\pi} \frac{\left(\tau_D/\tau_0\right)^{\alpha\beta} \sin\beta\theta}{\left[\left(\tau_D/\tau_0\right)^{2\alpha} + 2\left(\tau_D/\tau_0\right)^\alpha \cos\pi\alpha + 1\right]^{\beta/2}} \tag{E.3}$$

with

$$\tan\theta = \frac{\sin\pi\alpha}{\left(\tau_D/\tau_0\right)^\alpha + \cos\pi\alpha} \tag{E.4}$$

if the right-hand side is positive; else π must be added to θ. Clearly one cannot simply take $\alpha = 1$, since that would lead to singularities in eq. (E.3) and a zero in eq. (E.4). Therefore the Davidson-Cole distribution function is meaningful only in the limit $\alpha \to 1$. In the time domain, the Havriliak-Negami function is expressed through a series of generalized

exponential functions known as Mittag-Leffler functions [238], similar in appearance to the stretched exponential relaxation. The peculiar form of the relaxation time distribution function (E.3) is not realistic in most cases, but gives the tractable analytical form of the relaxation in the frequency domain.

Bibliography

[1] J. G. Bednorz, K. A. Müller, *Z. Phys. B* **64**, 189-193 (1986)

[2] B. Keimer, S. A. Kivelson, M. R. Norman, S. Uchida, J. Zaanen, *Nature* **518**, 179-186 (2015)

[3] J. C. Phillips, A. Saxena, A. R. Bishop, *Rep. Prog. Phys.* **66**, 2111-2182 (2003)

[4] N. Barišić et al., *Proc. Nat. Acad. Sci. USA* **110**, 12235-12240 (2013)

[5] P. Lazić, D. K. Sunko, *Europhys. Lett.* **112**, 37011 (2015)

[6] D. Pelc, M. Požek, V. Despoja, D. K. Sunko, *New J. Phys.* **17**, 083033 (2015)

[7] R. J. Cava et al., *Physica C* **165**, 419-433 (1990)

[8] M. A. Kastner, R. J. Birgeneau, G. Shirane, Y Endoh, *Rev. Mod. Phys.* **70**, 897-928 (1998)

[9] N. Barišić et al., *arxiv:1507.07885* (2015)

[10] S. Ono, S. Komiya, Y. Ando, *Phys. Rev. B* **75**, 024515 (2007)

[11] J. Hubbard, *Proc. R. Soc.* **276**, 238 (1963)

[12] A. H. MacDonald, S. M. Girvin and D. Yoshioka, *Phys. Rev. B* **37**, 9735 (1988)

[13] S. Chakravarty, B. I. Halperin, D. R. Nelson, *Phys. Rev. B* **39**, 2344 (1989)

[14] T. Thio, A. Aharony, *Phys. Rev. Lett.* **73**, 894 (1994)

[15] R. Coldea et al., *Phys. Rev. Lett.* **86**, 5377 (2001)

[16] F. C. Chou et al., *Phys. Rev. Lett.* **71**, 2323 (1993)

[17] C. Niedermayer et al., *Phys. Rev. Lett.* **80**, 3843 (1998)

[18] H.-H. Klauss et al., *Phys. Rev. Lett.* **85**, 4590 (2000)

[19] X. Shi et al., *Nature Mater.* **12**, 47 (2013)

[20] M. Hashimoto, I. N. Vishik, R.-H. He, T. P. Devereaux, Z.-X. Shen, *Nature Phys.* **10**, 483 (2014)

[21] M. Plate et al.,*Phys. Rev. Lett.* **95**, 077001 (2005)

[22] N. E. Hussey et al., *Nature* **425**, 814 (2003)

[23] B. Kyung, S. S. Kancharla, D. Senechal, A.-M. S. Tremblay, *Phys. Rev. B* **73**, 165114 (2006)

[24] G. Sordi, P. Semon, K. Haule, A.-M. S. Tremblay, *Sci. Rep.* **2**, 547 (2012)

[25] M. K. Chan et al., *Nature Comm.* **7**, 10819 (2016)

[26] T. Wu et al., *Nature* **477**, 191 (2011)

[27] T. Wu et al., *Nature Comm.* **4**, 2113 (2013)

[28] J. Fink et al., *Phys. Rev. B* (2009)

[29] J. Fink et al., *Phys. Rev. B* **83**, 092503 (2011)

[30] G. Ghiringhelli et al., *Science* **337**, 821 (2012)

[31] J. Chang et al., *Nature Phys.* **8**, 871 (2012)

[32] M. Hücker et al., *Phys. Rev. B* **90**, 054514 (2014)

[33] W. Tabis et al., *Nature Comm.* **5**, 5875 (2014)

[34] W. Tabis et al., *arxiv*:1702.03348 (2017)

[35] W. D. Wise et al., *Nature Phys.* **4**, 696 (2008)

[36] F. Laliberte et al., *Nature Commun.* **2**, 432 (2011)

[37] M. Hücker et al., *Phys. Rev. B* **83**, 104506 (2011)

[38] P. A. Lee, *Phys. Rev. X* **4**, 031017 (2014)

[39] E. Fradkin, S. A. Kivelson, J. M. Tranquada, *Rev. Mod. Phys.* **87**, 457 (2015)

[40] L. Nie, G. Tarjus, S. A. Kivelson, *Proc. Nat. Acad. Sci. USA* **111**, 7980-7985 (2014)

[41] V. J. Emery, S. A. Kivelson, O. Zachar, *Phys. Rev. B* **56**, 6120 (1997)

[42] M. Imada, *Phys. Rev. B* **72**, 075113 (2005)

[43] R. E. Peierls, *Ann. Phys.* **4**, 121 (1930)

[44] H. Fröhlich, *Proc. R. Soc.* **223**, 296 (1954)

[45] V. J. Emery, S. A. Kivelson, *Physica C* **209**, 597 (1993)

[46] J. M. Tranquada et al., *Nature* **375**, 561-563 (1995)

[47] H.-J. Grafe, N. J. Curro, M. Hücker, B. Büchner, *Phys. Rev. Lett.* **96**, 017002 (2006)

[48] V. Thampy et al., *Phys. Rev. B* **88**, 024505 (2013)

[49] N. J. Curro et al., *Phys. Rev. Lett* **85**, 642-645 (2000)

[50] V. Mitrović et al., *Phys. Rev. B* **78**, 014504 (2008)

[51] H.-H. Klauss, *J. Phys.: Cond. Mat.* **16**, S4457 (2003)

[52] N. Doiron-Leyraud et al., *Nature* **447**, 565 (2007)

[53] W. D. Wise et al., *Nature Phys.* **4**, 696 (2008)

[54] H. Yamase, *Phys. Rev. Lett.* **102**, 116404 (2009)

[55] J. Zaanen, O. Gunnarsson, *Phys. Rev. B* **40**, 7391 (1989)

[56] S. Sachdev, R. La Placa, *Phys. Rev. Lett.* **111**, 027202 (2013)

[57] T. Wu et al., *Nature Comm.* **6**, 6438 (2015)

[58] N. Barišić et al., *Nature Phys.* **9**, 761 (2013)

[59] A. M. Kadigrobov, A. Bjeliš, D. Radić, *Phys. Rev. Lett.* **100**, 206402 (2008)

[60] M. Fujita et al., *Phys. Rev. B* **70**, 104517 (2004)

[61] H.-H. Wu et al., *Nature Comm.* **3**, 1023 (2012)

[62] N. B. Christensen et al., *arXiv:1404.3192* (2014)

[63] A. W. Hunt, P. M. Singer, K. R. Thurber, T. Imai, *Phys. Rev. Lett.* **82**, 4300 (1999)

[64] P. M. Singer, A. W. Hunt, A. F. Cederström, T. Imai, *Phys. Rev. B* **60,** 15345 (1999)

[65] A. W. Hunt, P. M. Singer, A. F. Cederström, T. Imai, *Phys. Rev. B* **64,** 134525 (2001)

[66] H.-J. Grafe et al., *Eur. Phys. J. ST* **188,** 89-101 (2010)

[67] M.-H. Julien et al., *Phys. Rev. B* **63,** 144508 (2001)

[68] Y. Kohsaka et al., *Nature* **454**, 1072 (2008)

[69] M. J. Lawler et al. *Nature* **466**, 347-351 (2010)

[70] R. Daou et al. *Nature* **463**, 519-522 (2010)

[71] Y. Ando, K. Segawa, S. Komiya, A. N. Lavrov, *Phys. Rev. Lett.* **88**, 137005 (2002)

[72] L. Li et al., *Phys. Rev. Lett.* **Phys. Rev. B 81**, 054510 (2010)

[73] L. S. Bilbro, R. V. Aguilar, G. Logvenov, I. Božović, N. P. Armitage, *Phys. Rev. B* **84**, 139903(R) (2011)

[74] G. Yu et al., *arxiv:1210.6942* (2012)

[75] J. Xia et al., *Phys. Rev. Lett.* **100**, 127002 (2008)

[76] R.-H. He et al., *Science* **331**, 1579 (2011)

[77] B. Fauque et al., *Phys. Rev. Lett.* **96**, 197001 (2006)

[78] H. A. Mook, Y. Sidis, B. Fauque, V. Baledent, P. Bourges, *Phys. Rev. B* **78**, 020506(R) (2008)

[79] Y. Li et al., *Nature* **455**, 372 (2008)

[80] A. Dubroka et al., *Phys. Rev. Lett.* **106**, 047006 (2011)

[81] Z. A. Xu et al., *Nature* **406**, 486 (2000)

[82] Y. Wang, L. Li, N. P. Ong, *Phys. Rev. B* **73**, 024510 (2005)

[83] O. Cyr-Choiniere et al., *Nature* **458**, 743 (2009)

[84] B. Büchner, M. Breuer, A. Freimuth, A. P. Kampf, *Phys. Rev. Lett.* **73**, 1841 (1994)

[85] Q. Li, M. Hücker, G. D. Gu, A. M. Tsvelik, J. M. Tranquada, *Phys. Rev. Lett.* **99**, 067001 (2007)

[86] J. M. Tranquada et al., *Phys. Rev. B* **78**, 174529 (2008)

[87] E. Berg et al., *Phys. Rev. Lett.* **99**, 127003 (2007)

[88] E. Berg, E. Fradkin, S. A. Kivelson, *Phys. Rev. B* **79**, 064515 (2009)

[89] E. Berg, E. Fradkin, S. A. Kivelson, J. M. Tranquada, *New J. Phys.* **11**, 115004 (2009)

[90] D. Mihailović, V. V. Kabanov, *Phys. Rev. B* **63**, 054505 (2001)

[91] N. Plakida, *High-temperature cuprate superconductors – experiment, theory and applications.* (Springer, Berlin, 2010)

[92] R. E. Walstedt, *The NMR probe of high-T_c materials.* (Springer, Berlin, 2008)

[93] S. Sadewasser, J. S. Schilling, A. P. Paulikas, B. W. Veal, *Phys. Rev. B* **61**, 741 (2000)

[94] V. I. Kudinov et al., *Phys. Rev. B* **47**, 9017 (1993)

[95] P. M. Singer, A. W. Hunt, T. Imai, *Phys. Rev. Lett.* **88**, 047602 (2002)

[96] J. Bobroff et al., *Phys. Rev. Lett.* **89**, 157002 (2002)

[97] Y.-F. Lv et al., *Phys. Rev. Lett.* **115**, 237002 (2015)

[98] M. C. Boyer et al., *Nature Phys.* **3**, 802 (2007)

[99] J. W. Alldredge, K. Fujita, H. Eisaki, S. Uchida, K. McElroy, *Phys. Rev. B* **87**, 104520 (2013)

[100] O. Fischer, M. Kugler, I. Maggio-Aprile, C. Berthof, C. Renner, *Rev. Mod. Phys.* **79**, 353 (2007)

[101] D. Pelc et al., in preparation

[102] J. C. Phillips, *Proc. Natl. Acad. Sci. USA* **107**, 1307 (2010)

[103] A. R. Bishop, D. Mihailović, J. Mustre de Leon, *J. Phys.: Cond. Mat.* **15**, L169 (2003)

[104] V. V. Kabanov, D. Mihailović, *Phys. Rev. B* **65**, 212508 (2002)

[105] S. A. Kivelson, E. Fradkin, V. J. Emery, *Nature* **393**, 550-553 (1998)

[106] S. A. Kivelson et al., *Rev. Mod. Phys.* **75**, 1201-1241 (2003)

[107] M. Vojta, *Adv. Phys.* **58**, 699-820 (2009)

[108] M. Capati et al., *Nature Comm.* **6**, 7691 (2015)

[109] J. Cardy, *Scaling and renormalization in statistical physics.* (Cambridge University Press, Cambridge, 1996)

[110] N. J. Curro et al., *Phys. Rev. Lett* **85**, 642-645 (2000)

[111] S.-H. Baek et al., *Phys. Rev. B* **92**, 155144 (2015)

[112] Y. Gallais et al., *Phys. Rev. Lett.* **111**, 267001 (2014)

[113] H. Yamase, R. Zeyher, *Phys. Rev. B* **88**, 125120 (2013)

[114] A. P. Dioguardi et al., *Phys. Rev. Lett.* **116**, 107202 (2016)

[115] A. P. Ramirez et al., *Phys. Rev. Lett.* **68**, 2680 (1992)

[116] M. Došlić, D. Pelc, M. Požek, *Rev. Sci. Instrum.* **85**, 073905 (2014)

[117] A. Abragam, *The principles of nuclear magnetism.* (Oxford University Press, Oxford, 1982)

[118] J. R. Schrieffer, *Theory of Superonductivity.* (Westview Press, Boulder, 1999)

[119] C. H. Pennington et al., *Phys. Rev. B* **39**, 274 (1989)

[120] C. H. Pennington, C. P. Slichter, *Phys. Rev. Lett.* **66**, 381 (1991)

[121] M. Takigawa, J. L. Smith, W. L. Hults, *Phys. Rev. B* **44**, 7764(R) (1991)

[122] E. Fukushima, S. Roeder, *Experimental Pulse NMR.* (Westview Press, Boulder, 1981)

[123] S. Ohsugi et al., *J. Phys. Soc. Jpn.* **63**, 700 (1994)

[124] E. Hahn, *Phys. Rev.* **80**, 580 (1950)

[125] M. P. Augustine, D. M. TonThat, J. Clarke, *Sol. State Nucl. Mag. Reson.* **11**, 139 (1998)

[126] P. T. Greenland et al., *Nature* **465**, 1057 (2010)

[127] D. I. Hoult, *Rev. Sci. Instrum.* **50**, 193 (1979)

[128] A. S. Peshkovsky, J. Forguez, L. Cerioni, D. J. Pusiola, *J. Magn. Reson.* **177**, 67 (2005)

[129] B. Nebendahl, D.-N. Peligrad, M. Požek, A. Dulčić, M. Mehring, *Rev. Sci. Instrum.* **72**, 1876 (2001)

[130] D.-N. Peligrad, M. Mehring, A. Dulčić, *Phys. Rev. B* **67**, 174515 (2003)

[131] M. S. Grbić et al., *Phys. Rev. B* **80**, 094511 (2009)

[132] A. Narduzzo et al., *Phys. Rev. B* **78**, 012507 (2008)

[133] M. S. Grbić et al., *Phys. Rev. B* **83**, 144508 (2011)

[134] C. T. Van Degrift, *Rev. Sci. Instrum.* **46**, 599 (1975)

[135] M. D. Vannette et al., *Phys. Rev. B* **50**, 024421 (2009)

[136] F. N. H. Robinson, *J. Sci. Instrum.* **36**, 481 (1959)

[137] P. A. Probst, B. Collet and W. M. MacInnes, *Rev. Sci. Instrum.* **47**, 1522 (1976)

[138] I. Božović, X. He, J. Wu, A. T. Bollinger, *Nature* **536**, 309 (2016)

[139] X. He, A. Gozar, R. Sundling, I. Božović, *Rev. Sci. Instrum.* **87**, 113903 (2016)

[140] C. E. Gough, N. J. Exon, *Phys. Rev. B* **50**, 488 (1994)

[141] M. S. Grbić, *PhD dissertation* (University of Zagreb, 2011)

[142] E. Pardo, D.-X. Chen, A. Sanchez, *IEEE Trans. Magn.* **40**, 1491 (2004)

[143] P. A. Lee, N. Nagaosa, X.-G. Wen, *Rev. Mod. Phys.* **78**, 17 (2006)

[144] M. Tinkham, *Introduction to superconductivity.* (McGraw-Hill, New York, 1996)

[145] R. Corson, L. Malozzi, J. Orenstein, J. N. Eckstein, i Božović, *Nature* **398**, 221 (1999)

[146] V. J. Emery, S. A. Kivelson, *Nature* **374**, 434 (1995)

[147] M. S. Grbić et al., in preparation

[148] J. M. Kosterlitz, D. J. Thouless, *J. Phys. C* **6**, 1181 (1973)

[149] V. L. Berezinski, *Zh. Eksp. Teor. Fiz.* **61**, 1144 (1971)

[150] C. N. Yang, *Rev. Mod. Phys.* **34**, 694 (1962)

[151] N. D. Mermin, H. Wagner, *Phys. Rev. Lett. 17*, 1133 (1966)

[152] S. Coleman, *Commun. Math. Phys.* **31**, 259 (1973)

[153] D. R. Nelson, J. M Kosterlitz, *Phys. Rev. Lett.* **39**, 1201 (1977)

[154] P. Minnhagen, *Rev. Mod. Phys.* **59**, 1001 (1987)

[155] B. I. Halperin, D. R. Nelson, *J. Low Temp. Phys.* **36**, 599 (1979)

[156] A. M. Kadin, K. Epstein, A. M. Goldman, *Phys. Rev. B* **27**, 6691 (1983)

[157] C. T. Rogers, K. E. Myers, J. N. Eckstein, I. Bozovic, *Phys. Rev. Lett.* **69**, 160 (1992)

[158] J. Kötzler, D. Görlitz, S. Skwirblies, A. Wriedt, *Phys. Rev. Lett.* **87**, 127005 (2001)

[159] G. Grüner, *Rev. Mod. Phys.* **60**, 1129-1181 (1988)

[160] S. L. Hou, N. Bloembergen, *Phys. Rev.* **138** A1218 (1965)

[161] N. Cheenne, T. Mishonov, J. Indekeu, *Eur. Phys. J. B* **32**, 437 (2003)

[162] A. N. Lavrov, I. Tsukada, Y. Ando, *Phys. Rev. B* **68**, 094506 (2003)

[163] R. M. Fleming, C. C. Grimes, *Phys. Rev. Lett.* **42**, 1423 (1979)

[164] J. Dumas, C. Schlenker, J. Marcus, R. Buder, *Phys. Rev. Lett.* **50**, 757 (1983)

[165] M. Suzuki, *Prog. Theor. Phys.* **58**, 1151 (1977)

[166] J.-P. Bouchaud, G. Biroli, *Phys. Rev. B* **72**, 064204 (2005)

[167] C. Crauste-Thibierge et al., *Phys. Rev. Lett. 104*, 165703 (2010)

[168] D. Pelc, I. Marković, M. Požek, *Phys. Rev. Lett.* **109**, 095902 (2012)

[169] L. Berthier, G. Biroli, *Rev. Mod. Phys.* **83**, 587 (2011)

[170] P. Morin, D. Schmitt, *Phys. Lett. A* **73**, 67 (1979)

[171] X. Deng, A. Sternbach, K. Haule, D.N. Basov, G. Kotliar, *Phys. Rev. Lett.* **113**, 246404 (2014)

[172] L. D. Landau, *Zh. Eksp. Teor. Fiz.* **30**, 1058 (1956)

[173] P. Nozieres, D. Pines, *The theory of quantum liquids.* (Westview Press, Boulder, 1999)

[174] R. W. Boyd, *Nonlinear optics.* (Academic Press, Burlington, 2008)

[175] I. Pomeranchuk, *Zh. Eksp. Teor. Fiz.* **35**, 524 (1958)

[176] C. A. Lamas, D.C. Cabra, N. Grandi, *Phys. Rev. B* **78**, 115104 (2008)

[177] I. C. Khoo, *Phys. Rep.* **471**, 221 (2009)

[178] B. Wunderlich, *Thermal analysis.* (Academic Press, New York, 1990)

[179] A. Schilling, O. Jeandupeux, *Phys. Rev. B* **52**, 9714 (1995)

[180] F. Pobell, *Matter and methods at low temperatures.* (Springer, Berlin, 2007)

[181] D. Pelc, M. Vučković, H.-J. Grafe, S.-H. Baek, M. Požek, *Nature Comm.* **7**, 12775 (2016)

[182] G. Dhanaraj et al. (eds.), *Handbook of crystal growth* (Springer, Berlin, 2010)

[183] C. Hess, E. M. Ahmed, U. Ammerahl, A. Revcolevschi, B. Büchner, *Eur. Phys. J. ST* **188**, 103 (2010)

[184] B. J. Suh et al., *Phys. Rev. B* **61**, 9265(R) (2000)

[185] M. H. Hamidian et al., *Nature* **532**, 343 (2015)

[186] D. F. Ross, T. Senthil, *Phys. Rev. Lett.* **108**, 267001 (2012)

[187] D. F. Ross, T. Senthil, *Phys. Rev. B* **86**, 115138 (2012)

[188] K. Sun, M. J. Lawler, E.-A. Kim, *Phys. Rev. Lett.* **104**, 106405 (2010)

[189] D. Pelc, H.-J. Grafe, G. D. Gu, M. Požek, *Phys. Rev. B* **95**, 054508 (2017)

[190] J. D. Axe et al., *Phys. Rev. Lett.* **62**, 2751 (1989)

[191] R. Werner, M. Hücker, B. Büchner, *Phys. Rev. B* **62**, 3704 (2000)

[192] M. Hücker et al., *Physica C* **460**, 170 (2007)

[193] A. J. Achar et al., *Science* **351**, 576 (2016)

[194] N. Barišić et al., *Phys. Rev. B* **78**, 054518 (2008)

[195] J.-H. Chu, H.-H. Kuo, J. G. Analytis, I. R. Fisher,*Science* **337**, 710 (2012)

[196] R. M. Fernandes, A. V. Chubukov, J. Schmalian, *Nature Phys.* **10**, 97 (2014)

[197] M. P. Lilly, K. B. Cooper, J. P. Eisenstein, L. N. Pfeiffer, K. W. West, *Phys. Rev. Lett.* **82**, 394 (1999)

[198] M. Hücker, M. v. Zimmermann, G. D. Gu, *Phys. Rev. B* **75**, 041103(R) (2007)

[199] A. Pautrat, F. Giovannelli, N. Poirot, *Phys. Rev. B* **75**, 125106 (2007)

[200] A. Asamitsu, Y. Tomioka, H. Kuwahara, Y. Tokura, *Nature* **388**, 50 (1997)

[201] S. Yamanouchi, Y. Taguchi, Y. Tokura, *Phys. Rev. Lett.* **83**, 5555

[202] J. Bardeen, *Phys. Rev. Lett.* **42**, 1498 (1980)

[203] X. M. Chen et al., *Phys. Rev. Lett.* **117**, 167001 (2016)

[204] H. Tou, M. Matsumura, H. Yamagata, *J. Phys. Soc. Jpn.* **61**, 1477-1480 (1992)

[205] S. Pliberšek, P. F. Meier, *Europhys. Lett.* **50**, 789 (2001)

[206] A. Dulčić, B. Rakvin, M. Požek, *Europhys. Lett.* **10**, 593 (1989)

[207] B. Sapoval, C. Hermann, *The physics of semiconductors.* (Springer, Berlin-New York, 1993)

[208] S. M. Hayden et al., *Phys. Rev. Lett.* **76**, 1344 (1996)

[209] Q. Si, Y. Zha, K. Levin, J. P. Lu, *Phys. Rev. B* **47**, 9055 (1993)

[210] N. Bloembergen, E. M. Purcell, R. V. Pound, *Phys. Rev.* **73**, 679 (1948)

[211] G. Adam, H. J. Gibbs, *J. Chem. Phys.* **43**, 139 (1961)

[212] E. Donth, *The Glass Transition.* (Springer, Berlin, 2001)

[213] P. Fulde, R. A. Ferrell, *Phys. Rev.* **135**, A550 (1964)

[214] A. I. Larkin, Y. N. Ovchinnikov, *Zh. Teor. Eksp. Fiz.* **47**, 1136 (1964)

[215] S. Baruch, D. Orgad, *Phys. Rev. B* **77**, 174502 (2008)

[216] S. Havriliak, S. Negami, *Polymer* **8**, 16 (1967)

[217] F.Alvarez, A. Alegria, J. Colmenero, *Phys. Rev. B* **44**, 7306 (1991)

[218] D. W. Davidson, R. H. Cole, *J. Chem. Phys.* **19**, 1484 (1951)

[219] R. Zorn, *J. Polymer Sci.* **37**, 1043 (1999)

[220] G. M. Wysin, *Phys. Rev. B* **71**, 094423 (2005)

[221] S. A. Leonel et al., *Phys. Rev. B* **67**, 104426 (2003)

[222] H. Kitano, T. Ohashi, A. Maeda, I. Tsukada, *Phys. Rev. B* **73**, 092504 (2006)

[223] L. Benfatto, C. Castellani, T. Giamarchi, in *40 Years of Berezinskii-Kosterlitz-Thouless theory* (ed. J. V. Jose, World Scientific, Singapore, 2013)

[224] D. Podolsky, S. Raghu, A. Vishwanath, *Phys. Rev. Lett.* **99**, 117004 (2007)

[225] A. Gozar et al., *Nature* **455**, 782 (2008)

[226] G. Logvenov, A. Gozar, I. Božović, *Science* **326**, 699 (2009)

[227] L. S. Bilbro et al., *Nature Phys.* **7**, 298-302 (2011)

[228] G. Drachuck et al., *Phys. Rev. B* **85**, 184518 (2012)

[229] J. E. Sonier et al., *Phys. Rev. B* **76**, 134518 (2007)

[230] G. Grissonnanche et al., *Nature Comm.* **5**, 3280 (2014)

[231] Y. Ando et al., *Phys. Rev. B* **60**, 12475 (1999)

[232] C. S. O'Hern, T. C. Lubensky, J. Toner, *Phys. Rev. Lett.* **83**, 2745 (1999)

[233] J. Chang et al., *Nature Phys.* **8**, 751 (2012)

[234] J. D. Axel et al., *Phys. Rev. Lett.* **62**, 2751 (1989)

[235] S. Barišić, J. Zelenko, *Solid State Commun.* **74**, 367 (1990)

[236] C. C. Homes et al., *Phys. Rev. Lett.* **96**, 257002 (2006)

[237] M. Hücker et al., *J. Supercond. Nov. Mag.* **24**, 1229 (2011)

[238] J. Hilfer, *Phys. Rev. E* **65**, 061510 (2002)

Curriculum vitae

Damjan Pelc was born in Zagreb, Croatia, on May 28th 1987. He received primary and secondary education in Zagreb, and enrolled in the University of Zagreb to study at the Faculty of Science in 2006. In 2011 he graduated from the Physics Department of the Faculty of Science, and started his graduate studies at the same institution in the group of prof. Miroslav Požek. His research interests are in condensed matter physics and include high-temperature superconductors, disordered systems, and soft and glassy matter. As of May 2017, he has taught several undergraduate courses, published eleven scientific papers, and held four invited talks at international conferences and research institutions. He lives in Zagreb with his wife, cat and a number of plants.

Published articles:

D. Pelc, H.-J. Grafe, G. Gu and M. Požek, Cu nuclear magnetic resonance study of charge and spin stripe order in $La_{1.875}Ba_{0.125}CuO_4$. *Phys. Rev. B* **95**, 054508 (2017)

D. Pelc et al., Unconventional charge order in a co-doped high-T_c superconductor. *Nature Comm.* **7**, 12775 (2016)

I. Kupčić, G. Nikšić, Z Rukelj and D. Pelc, Effective number of charge carriers in doped graphene: Generalized Fermi liquid approach. *Phys. Rev. B* **94**, 075434 (2016)

J. C. C. Freitas et al., Determination of the hyperfine magnetic field in magnetic carbon-based materials: DFT calculations and NMR experiments. *Scientific Reports* **5**, 14764 (2015)

D. Pelc, M. Požek, V. Despoja and D. K. Sunko, Mechanism of metallization and superconductivity suppression in $YBa_2Cu_{2.97}Zn_{0.03}O_{6.92}$ revealed by ^{67}Zn NQR. *New J. Phys.* **17**, 083033 (2015)

P. Lazić et al., Effects of Sr and Zn doping on the metallicity and superconductivity of LSCO and YBCO. *J. Supercond. Nov. Magn.* **28**, 1299 (2015)

M. Došlić, D. Pelc and M. Požek, Contactless measurement of nonlinear conductivity in the radio-frequency range. *Rev. Sci. Instrum.* **85**, 073905 (2014)

T. Cvitanić, D. Pelc, M. Požek, E. Amit and A. Keren, ^{17}O Knight shift study of the interplay of superconductivity and pseudogap in $(Ca_xLa_{1-x})(Ba_{1.75-x}La_{0.25+x})Cu_3O_y$.

Phys. Rev. B **90**, 054508 (2014)

D. Pelc, S. Marion, M. Požek and M. Basletić, Role of microscopic phase separation in gelation of aquesous gelatin solutions. *Soft Matter* **10**, 348 (2014)

D. Pelc, I. Marković and M. Požek, Cooperative mercury motion in the ionic conductor Cu_2HgI_4. *Phys. Rev. Lett.* **109**, 095902 (2012)

D. Pelc, S. Marion and M. Basletić, Four-contact impedance spectroscopy of conductive liquid samples. *Rev. Sci. Instrum.* **82**, 073907 (2011)